Instrumentation Development for Site-Specific Prediction of Spectral Effects on Concentrated Photovoltaic System Performance

by

Viktar Tatsiankou

Thesis submitted to the Faculty of Graduate and Postdoctoral Studies in partial fulfilment
of the requirement for the Master of Applied Science
in Electrical and Computer Engineering

School of Electrical Engineering and Computer Science
University of Ottawa

"Patience and work will fray through anything"

– Russian proverb

Abstract

The description of a novel device to measure the spectral direct normal irradiance is presented. The solar spectral irradiance meter (SSIM) was designed at the University of Ottawa as a cost-effective alternative to a prohibitively expensive field spectroradiometer (FSR). The latter measures highly-varying and location-dependent solar spectrum, which is essential for accurate characterization of a concentrating photovoltaic system's performance. The SSIM measures solar spectral irradiance in several narrow wavelength bands with a combination of photodiodes with integrated interference filters. This device performs spectral measurements at a fraction of the cost of a FSR, but additional post-processing is required to deduce the solar spectrum. The model was developed to take the SSIM's inputs and reconstruct the solar spectrum in 280–4000 nm range. It resolves major atmospheric processes, such as air mass changes, Rayleigh scattering, aerosol extinction, ozone and water vapour absorptions.

The SSIM was installed at the University of Ottawa's CPV testing facility in September, 2013. The device gathered six months of data from October, 2013 to March, 2014. The mean difference between the SSIM and the Eppley pyrheliometer was within $\pm 1.5\%$ for cloudless periods in October, 2013. However, interference filter degradation and condensation negatively affected the performance of the SSIM. Future design changes will improve the longterm reliability of the next generation SSIMs.

Statement of Originality

The research work presented in this dissertation, including the model development for the solar spectrum reconstruction, the mechanical and the electrical designs of the solar spectral irradiance meter, and its performance analysis, was carried out solely by the author under the supervision of Dr. Karin Hinzer from September, 2012 to May, 2014. To the best of his knowledge, the results contained in this thesis are original, unless otherwise noted.

Acknowledgement

First of all, I would like to thank my supervisor Dr. Karin Hinzer for giving me the opportunity back in 2008 to be a work-study student at SUNLAB, which I believe is responsible for nurturing me to the graduate studies. Dr. Hinzer's utmost respect and entrust of responsibility for her students is a privilege that I cherish. I believe students at SUNLAB are given all of the tools to succeed and excel in their studies, and Dr. Hinzer works hard on the sidelines to make this happen.

I am grateful to senior members of SUNLAB, Matt Wilkins, Dr. Joan Haysom and Dr. Henry Schriemer for their valuable input at the meetings and thoughtful editing of my publications. Furthermore, I would like to thank all members of SUNLAB for making my graduate studies memorable and exciting.

I am thankful to Morgan Solar Inc. for the initiation of this research project.

I am appreciative to the National Science and Engineering Research Council of Canada for their financial support of this work.

Special thank you goes to my angel guardians Marjorie and Alex Dow, who I consider my second parents. Dear Marjorie and Alex, your never-ending support and constant motivation over the years allowed me to excel in everything I do and it is a big reason why I will be pursuing the doctorate studies. From the bottom of my heart I think that "you got it all" and with that thank you for everything!

An honourable mention (sarcasm) goes to my girlfriend, Roxanne Bouvier. Without your kindness, patience, and love I would not be able to complete this thesis. Your support is a bedrock of my success!

Дорогие мама и папа, я надеюсь что пара следующих предложений опишет, как я чувствую о вашей поддержке на протяжении этих многих лет. Однако в действительности, мне нужно пара страниц. Тем не менее, ваша любовь, мотивация, и ментальное присутство помогли мне добиться успеха в Канаде. Я люблю вас, скучаю по вам и обещаю что с этого момента я буду вас посещать на много чаще. Огромное спасибо товарищи!

List of Publications

This thesis work has led to the following publications:

[1] **V. Tatsiankou**, K. Hinzer, A. Muron, et al. "Solar resource assessment with the solar spectral irradiance meter". In: *10th International Conference on Concentrating Photovoltaic Systems: CPV-10*. Submitted April, 2014.

[2] A. Trojnar, J. Thibaudeau, **V. Tatsiankou**, et al. "The effects of the varying sunlight intensity over the course of a day on the efficiency of Si and GaAs solar cells using Crosslight simulations". In: TEXPO and CMC Annual Symposium. 2013.

[3] **V. Tatsiankou**, K. Hinzer, and S. Myrskog. "Invention disclosure: Solar spectral irradiance meter". In: University of Ottawa's Technology Transfer and Business Enterprise. 2014.

[4] **V. Tatsiankou**, K. Hinzer, A. Muron, et al. "Reconstruction of the solar spectral resource using limited spectral sampling for concentrating photovoltaic systems". In: *Photonics North 2013*. Vol. 891506. International Society for Optics and Photonics. 2013, pp. 1–11.

Contents

List of Figures

List of Tables

List of Symbols and Acronyms

Roman Symbols

A	Area
A_i	Absorption coefficient of gas i
c	Speed of light in vacuum, 2.99792458×10^8 m/s
c_m	Mass concentration of a gas
c_n	Molar concentration of a gas
C_i	Temperature correction of gas i
D_n	Diffusion coefficient of electrons
D_p	Diffusion coefficient of holes
E_g	Bandgap of a semiconductor
E_ph	Energy of the photon
f	Frequency
F_x	Filter transmission of the channel x
FF	Fill factor
H	Pathlength of the entire atmosphere
h	Planck constant, $6.62606957 \times 10^{-34}$ J $\cdot$ s
I	Current
I_0	Reverse saturation current
I_dif	Diffusion current
I_d	Dark current
I_mp	Current at the maximum power point
I_n1	Johnson noise current
I_n2	Shot noise current
I_rad	Radiative recombination current
I_scr	Current due to recombination in the space charge region
I_sc	Photogeneration or short circuit current

k	Boltzmann constant, $1.3806488 \times 10^{-23}$ J/K
L	Irradiance
L_{n}	Diffusion length of electrons
L_{n}	Diffusion length of holes
M	Molar mass of a gas
m_i	Air mass of gas i
n	Ideality factor of a diode
N_{A}	Avogadro constant, 6.0221420×10^{23} molecules/mol
N_{a}	Doping concentration in a p-type semiconductor
N_{d}	Doping concentration in a n-type semiconductor
n_{i}	intrinsic carrier concentration
N_{L}	Loschmidt constant, 2.6867774×10^{25} molecules/m^3
P	Pressure
P_{max}	Maximum power of a solar cell
P_{r}	Ratio of actual to reference pressure
p_i	Pathlength of gas i through the atmosphere
q	Electron charge, $1.6021766 \times 10^{-19}$ C
Q_{m}	Total mass column density
Q_{n}	Total column density
R	Ideal gas constant, 8.3144621 m$^3 \cdot$ Pa $\cdot$ mol$^{-1} \cdot$ K^{-1}
R	Responsivity
r	Ratio of the average to actual sun to earth distance
R_{p}	Shunt resistance
R_{s}	Series resistance
S	Spectral irradiance
S_0	Extraterrestrial spectral irradiance
T	Temperature
T_{nom}	Reference temperature
T_{r}	Ratio of actual to reference temperature
T_i	Transmission of gas i through the atmosphere
V	Voltage
V_{mp}	Voltage at the maximum power point
V_{oc}	Open circuit voltage
Z	Zenith angle of the sun

Greek Symbols

α	Ångström's exponent for aerosol optical depth
β	Ångström's coefficient for aerosol optical depth
χ_V	Mixing ratio of a gas
Δf	Noise bandwidth
ϵ_1	Pressure scaling factor for water vapour
ϵ_2	Humidity correction factor for water vapour
η	Efficiency
γ	Pressure correction coefficient
κ_{ij}	Coefficients for calculating the air mass of gas i
λ	Wavelength
ω_i	Rayleigh scattering fit coefficients
ϕ	Azimuth angle of the sun
τ_i	Optical depth of gas i
θ	Elevation angle of the sun

Acronyms

ADC	Analog to digital converter
AM	Air mass
AM0	Extraterrestrial solar spectrum
ASTM	American Society for Testing and Materials
CPV	Concentrating photovoltaic(s)
DHI	Diffuse horizontal irradiance
DNI	Direct normal irradiance
DU	Dobson unit
FF	Fill factor
FSR	Field spectroradiometer
FWHM	Full width at half maximum
GHI	Global horizontal irradiance
IR	Infrared
MCFR	Multi-channel filter radiometer
MCU	Microcontroller unit
MJSC	Multi-junction solar cell
NREL	National Renewable Energy Laboratory
OTF	Optical transfer function

PCB	Printed circuit board
ppmv	parts per million by volume
PV	Photovoltaic(s)
RCR	Remote cosine receptor
RMS	Root mean square
SATP	Standard ambient temperature and pressure
SMARTS	Simple Model of the Atmospheric Radiative Transfer of Sunshine
SPA	Solar position algorithm
SSIM	Solar spectral irradiance meter
STP	Standard temperature and pressure
TJSC	Triple-junction solar cell
UV	Utraviolet

Chapter 1

Introduction

Over the past centuries, the standard of living for our society significantly improved due to advances in medicine, agriculture, and engineering. This breathtaking progress has been largely fuelled by the availability of electrical energy - without it, modern ways of life cannot be sustained. At present, the energy production is largely dependent on fossil fuels, such as coal, oil and natural gas. These fuel sources are being rapidly depleted as the appetite for energy in developing countries rises, aided primarily by a burgeoning population growth in Asia. The share of the total electricity generation by fossil fuels is projected to fall from 67% to 38% from 2010 to 2040 [1]. Meanwhile, American oil giant Exxon Mobile predicts an 85% increase in global energy demand over the same time period [2]. Today, no one argues with the fact that the world's fossil fuel resources will be exhausted in the near future; the debate is rather: how do we to replace them? Photovoltaic (PV) systems are making a convincing case for being the energy technology of tomorrow. In a nutshell, photovoltaics is a safe, scalable, and modular technology that has low operating costs and no emissions during operation, all while "running" on an essentially limitless energy source - sunlight. These advantages make PV systems more attractive than other renewable sources of energy, such as wind, biomass, and geothermal.

There are two main types of the solar technologies: flat panel PV and concentrating photovoltaics (CPV). The first predominantly uses silicon (Si) semiconductor to convert the sunlight into electricity. On the other hand, CPV systems typically concentrate light with optical components on a multi-junction solar cell (MJSC), which consists of several layers of semiconductor materials. Figure 1.1 demonstrates the record efficiencies for both the PV and CPV research solar cells over the past four decades. This chart reveals that the MJSCs are presently the most efficient solar devices in the world, with efficiencies reaching up to 44% under concentration. Furthermore, the pace of the MJSCs development has been franticly

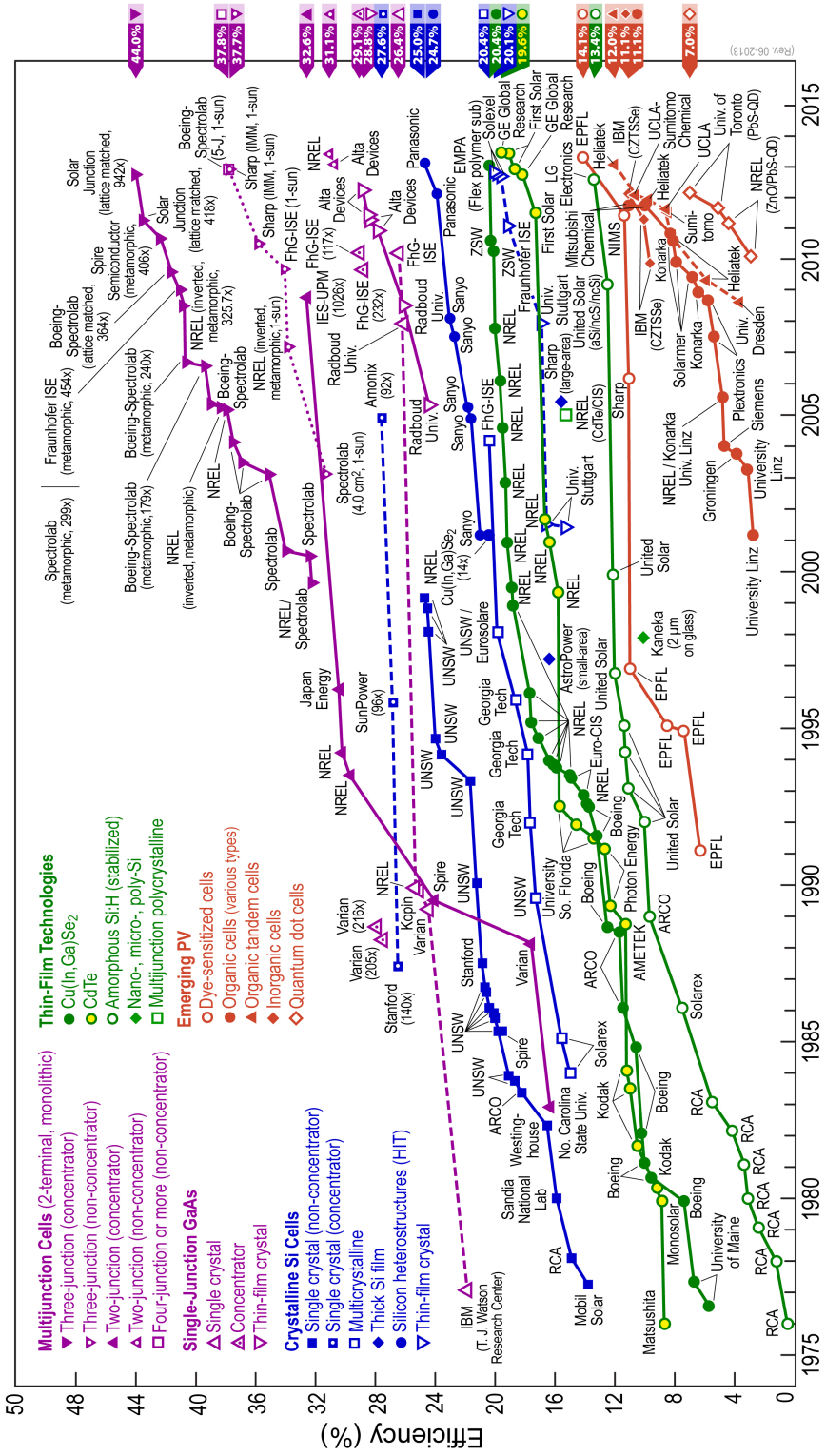

Figure 1.1: Record efficiencies of the solar cell technologies from 1975 to 2014 [3].

exciting, with efficiency improving on average 0.85% per year since 2000, and on top of that, there is a lot of room for potential future growth. On the contrary, the efficiency improvements for the Si solar cells have been stagnant for over a decade as its fundamental efficiency limits are being approached. Overall, Figure 1.1 gives a good perspective on different types of solar technologies available today, all of which have advantages either from cost, efficiency, or manufactureability points of view. Of all of them, CPV technology utilizing MJSCs is one of the most promising to significantly alter the energy industry.

1.1 Overview of CPV systems

CPV systems use inexpensive refractive or reflective optics to concentrate light on a small, high-efficiency MJSC. The main benefit of this approach is the significant reduction in the quantity of the required semiconductor material, which is inherently expensive. Furthermore, the sunlight concentration fundamentally improves a solar cell's performance, as demonstrated in Figure 1.1, where the highest 1-sun (1000 W/m^2) efficiency for the MJSC is 37.8% versus 44% under 942-sun concentration. There are many optical methods to concentrate the sunlight on a MJSC, some of which are presented in Figure 1.2. The Fresnel lens is a

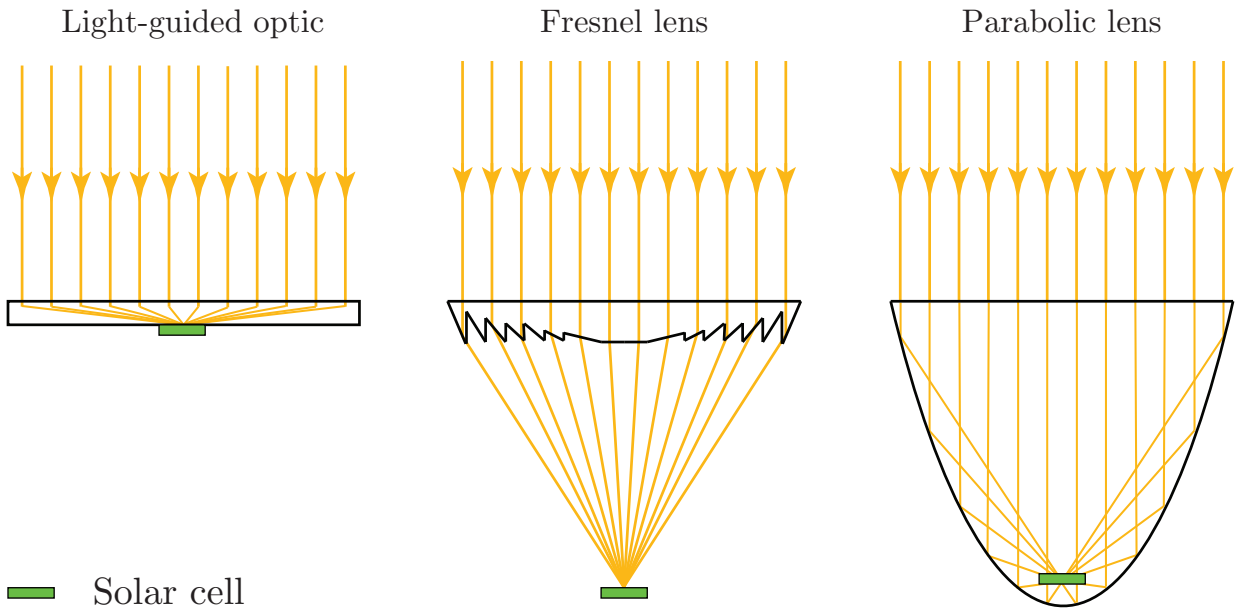

Figure 1.2: Conceptual representation of the optical topologies for light concentration in CPV systems. The Fresnel lens is the most popular way of focusing the sunlight on a MJSC (adapted from [4]).

conventional way for the sunlight concentration in CPV systems. Major CPV heavyweights, such as Ammonix, Semprius, and Suncore, all use this approach. However, Canadian start-up Morgan Solar pioneered the light-guided optic with zero focal length as a new way of focusing the sunlight on a MJSC, as demonstrated in Figure 1.2. This approach promises to reduce the manufacturing costs associated with building a CPV module.

CPV modules have a narrow light acceptance angle and as a result they must continuously track the sun with a high accuracy. Figure 1.3 shows Morgan Solar's implementation of the Sun Simba CPV modules on their dual-axis, human scale Savanna tracking systems. Tracking systems are typically equipped with a sun sensor, which allows to orientate solar modules within a fraction of a degree to the sun rays. As a result, CPV modules are exposed to the spectral direct normal irradiance (DNI). To accurately characterize the system's performance, knowledge of the spectral DNI is often desired, which can be obtained with a field spectroradiometer (FSR). However, this instrument is prohibitively expensive and very few entities actually have it. Therefore, this thesis addresses the issue of CPV systems characterization through the development of an inexpensive solar spectral irradiance meter (SSIM) at the University of Ottawa's CPV testing facility.

Figure 1.3: Morgan Solar's Sun Simba CPV modules mounted on the Savanna trackers [5]. Four panels are mounted on each corner of the boxframe, which constitutes a single unit (cell) within a solar farm.

1.2 Thesis overview

This thesis consists of six chapters. The first chapter introduces the need for renewable energy in the face of depleting fossil fuel reserves. A brief case is made for PV as the technology for powering the energy needs of today and tomorrow. Specifically, it is predicted that CPV systems with their high efficiency, heat tolerability, and great potential for future cost-reductions, will dramatically change the landscape of the energy industry.

Chapter 2 contains a detailed description of the solar resource. The astronomical, geographical, and atmospheric factors influencing the solar spectral resource distribution at the earth's surface are identified and quantified. A great emphasis is placed on temporally varying atmospheric constituents, such as the aerosols and the water vapour. The effects of these and other constituents on the solar spectrum are presented. Finally, an overview of the instrumentation required for the solar resource assessment is given.

Chapter 3 demonstrates a method of limited spectral sampling with a simulated multi-channel filter radiometer (MCFR) to reconstruct incident solar spectra. The measured FSR's spectrum from the University of Ottawa's CPV testing facility is used to simulate the MCFR with varying number of channels. This study is used to determine the optimal number of channels required by the MCFR to adequately reconstruct the solar spectrum. The model resolves major atmospheric processes, such as air mass (AM), Rayleigh scattering, aerosol extinction, water vapour and ozone absorptions. This chapter provides the foundation for the solar spectrum reconstruction of the SSIM.

Chapter 4 dives into single-junction solar cell theory, which is extended to the development of a MJSC model. The latter is used to demonstrate the effect of aerosol extinction and water vapour and ozone absorptions on the MJSC performance throughout the day. It is proved that the aforementioned atmospheric constituents can significantly affect the functionality of the MJSC and consequently the CPV system. Therefore, to accurately assess the performance of a CPV system, knowledge of the spectral DNI is required at the installation site.

Chapter 5 introduces the University of Ottawa's CPV testing facility in terms of the available instrumentation for solar resource assessment. This chapter describes the opto-mechanical and electrical designs of the SSIM. The SSIM's performance is evaluated over six months against the baseline instrumentation, such as the spectroradiometer, the pyrheliometer and the weather station.

Chapter 6 gives an overview and provides a summary of each chapter in this thesis. Furthermore, it recaps main highlights from the performance of the SSIM and lists the necessary design changes to improve the longterm reliability of this device.

References

[1] *International Energy Outlook 2013*. Tech. rep. U.S. Energy Information Administration, 2013.

[2] *2012 Energy Outlook: A view to 2040*. Tech. rep. Exxon Mobile, 2012.

[3] NREL. *Best research photovoltaic cell efficiencies*. US Department of Energy. [Accessed: April 26, 2014]. URL: http://commons.wikimedia.org/wiki/File:Best_Research-Cell_Efficiencies.png.

[4] *How it works*. Morgan Solar. [Accessed: April 26, 2014]. URL: http://dev.morgansolar.com/wp-content/uploads/2011/11/figure1-638px.jpg.

[5] *Savanna trackers*. Morgan Solar. [Accessed: April 26, 2014]. URL: http://morgansolar.com/wp-content/uploads/2013/09/2013.09.10_Savanna1.4_SunSimbafront_PVbground_Slider_Web.jpg.

Chapter 2

The solar resource

The sun is an indispensable source of energy for all living organisms on the earth. It is a driving force behind our planet's life-sustaining processes such as suitable climate, photosynthesis, and surface illumination. The sun can be approximated as an isotropic blackbody radiator with a surface temperature close to 6000 K. Only a small amount of its total electromagnetic radiation reaches the top of the earth's atmosphere at the mean sun-earth distance of about 1.5×10^8 km. At this point in space the radiation intensity, or "solar constant", is equal to approximately 1366 W/m^2 and the spectral distribution is referred to as air mass zero (AM0) extraterrestrial spectrum. The AM0 spectrum undergoes considerable transformation as it traverses through the earth's atmosphere before it can be harvested by solar panels. Atmospheric processes, such as Rayleigh scattering, aerosol extinction, ozone and water vapour absorptions, modify the solar spectrum both temporally and geographically. This chapter takes a detailed look at the geographical, environmental and astronomical factors influencing the solar spectral irradiance at the earth's surface.

2.1 The blackbody

The sun radiates electromagnetic energy at different intensities in a broad wavelength range spanning from gamma rays to radio waves. Its emission spectrum can be approximated to the spectral distribution of an ideal radiator, a blackbody, of specific surface temperature. Blackbody radiation theory was proposed at the onset of the 20$^{\text{th}}$ century by a German scientist M. Planck. Eventually it lead to the development of the Planck's law, which is defined in thermal equilibrium as [1]

$$S(\lambda, T) = \frac{2\pi \cdot c^2 \cdot h}{\lambda^5 \cdot (e^{hc/\lambda kT} - 1)}, \tag{2.1}$$

where S is the spectral irradiance (W/m^2/nm), λ is the wavelength (m), T is the mean surface temperature of the blackbody (K), c is the speed of light in vacuum (m/s), h is Planck constant, and k is Boltzmann constant (J/K). Figure 2.1 demonstrates the use of the Planck's law to roughly match the AM0 with the blackbody's emission spectrum. As the mean surface temperature of the blackbody is increased from 4000 to 6000 K, its emission spectrum "blue" shifts, as implied by shifting peaks of the curves in Figure 2.1. At 6000 K the blackbody's spectrum and the AM0 match reasonably well, albeit not perfectly, as expected, since the sun is not an ideal radiator.

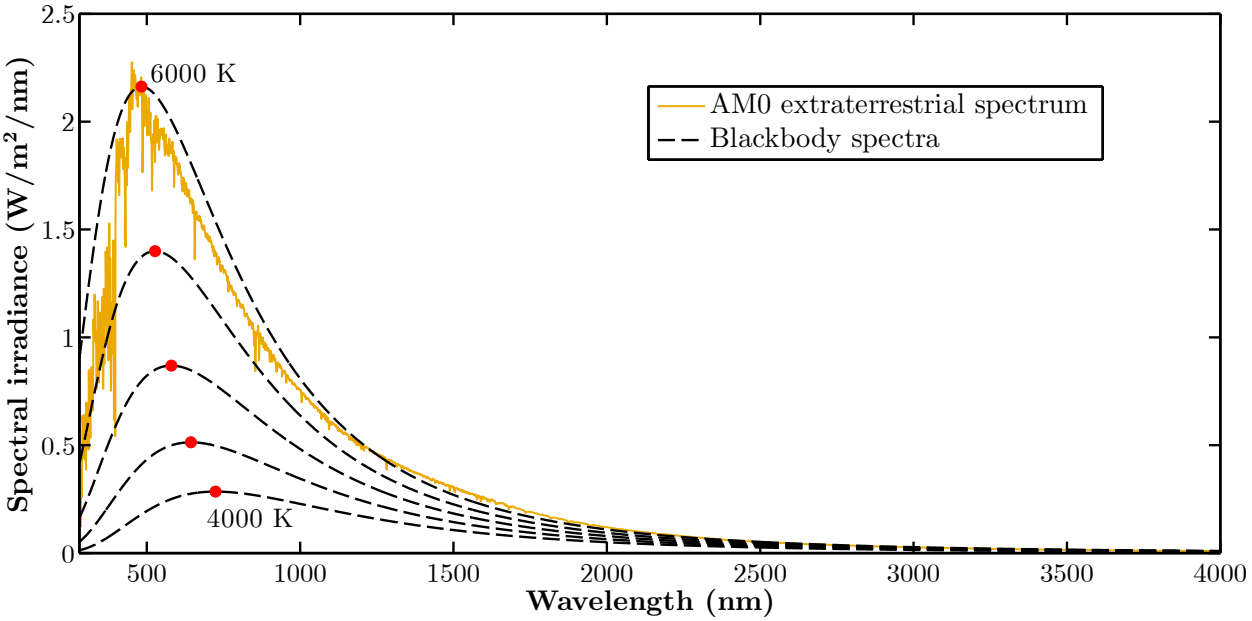

Figure 2.1: The blackbody spectra with the mean surface temperature varying uniformly from 4000 to 6000 K. The AM0 extraterrestrial spectrum can be approximated by a blackbody radiator with the mean surface temperature of 6000 K.

2.2 The extraterrestrial irradiance

The sun's gravitational forces keep the earth in its elliptical orbit, which implies the distance between these two planetary bodies is changing as a function of time with the minimum and maximum being at perihelion and aphelion, respectively. The sun emits energy isotropically over its surface area, known as the photosphere. The irradiance at distance x away from the centre of the sun, $L(x)$, can be expressed as:

$$L(x) = \frac{P_{\text{total}}}{4\pi \cdot x^2 - 4\pi \cdot r_{\text{sun}}^2}, \tag{2.2}$$

where P_{total} is the total power emitted by the sun and r_{sun} is the sun's mean radius. If x is significantly larger then r_{sun}, the irradiance at distance x can be rewritten as:

$$L(x) \approx \frac{P_{\text{total}}}{4\pi \cdot x^2} \text{ for } x >> r_{sun}. \tag{2.3}$$

If the irradiance at distance x_1 is known, the irradiance at distance x_2 can be determined through this expression:

$$L(x_2) \approx L(x_1) \cdot \frac{x_2^2}{x_1^2} \text{ for } x_1, x_2 >> r_{sun}. \tag{2.4}$$

Since the mean sun-earth distance is over 215 times larger than the mean sun's radius, Equation 2.4 is appropriate for the earth's applications. One known data point $[x_1, L(x_1)]$ is needed, as per Equation 2.4, to determine the irradiance at any distance x from the centre of the sun. It is accepted that at the mean sun earth distance the extraterrestrial irradiance is equal to 1366.1 W/m^2 in 0.1195–1000 µm range [2]. However, from November, 1978 to January, 2003 its absolute minimum and maximum were 1363 W/m^2 and 1368 W/m^2, respectively, with variation mainly due to the sun spots [3]. Figure 2.2 shows the calculated fluctuation of about ±3.3% of the extraterrestrial irradiance throughout 2014. Therefore, 1322 W/m^2 and 1413 W/m^2 are the minimum and the maximum irradiance, respectively, reaching the top of the earth's atmosphere.

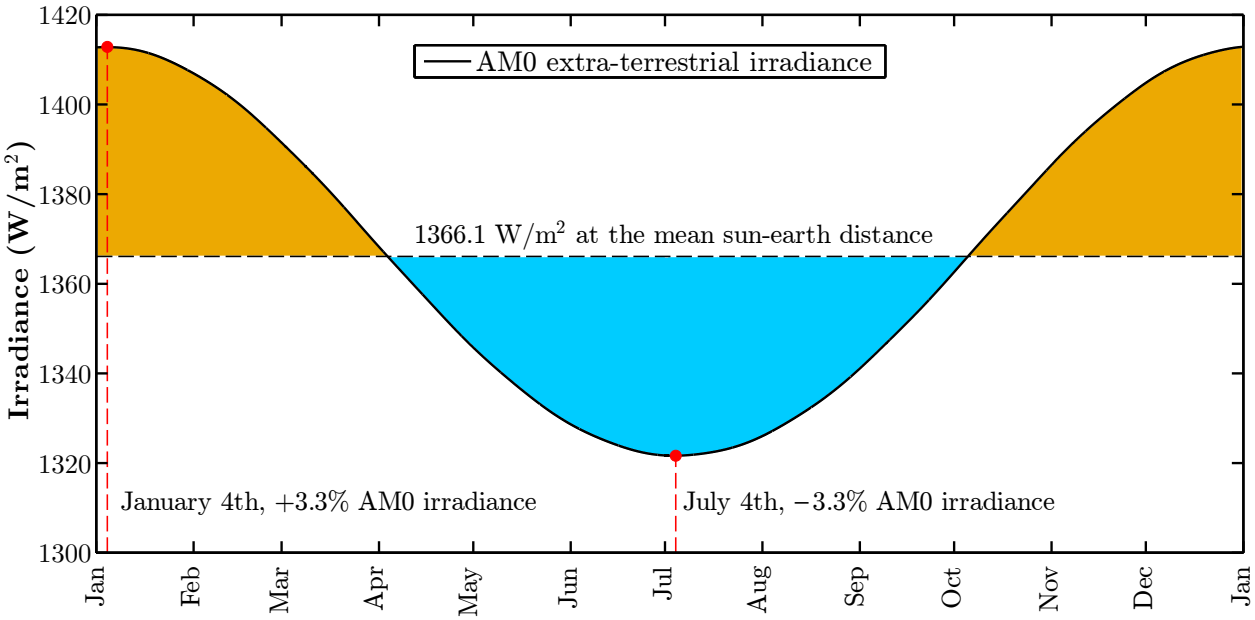

Figure 2.2: The predicted fluctuation of the extraterrestrial irradiance for 2014 with the minimum and maximum of 1322 W/m^2 and 1413 W/m^2 occurring on July 4th and January 4th, respectively.

2.3 Global solar coordinates

The geometric orbit of the earth around the sun is called the ecliptic plane. The earth's rotational axis, which is aligned north-south, is tilted by 23.44° with respect to the ecliptic plane, as shown in Figure 2.3. This geometry is primarily responsible for existence of seasons on the earth. The northern hemisphere is tilted toward the sun in June and away from the sun in December. As a result, there are more sunshine hours in the northern hemisphere in June as opposed to December, hence, the difference between summer and winter. The first days of summer and winter are considered to be summer and winter solstices. On these dates, the sun has the highest and lowest altitudes at the local solar noon, respectively. During spring and fall equinoxes the earth is neither tilted toward nor away from the sun, and the sunrise and sunset are due east and west, respectively.

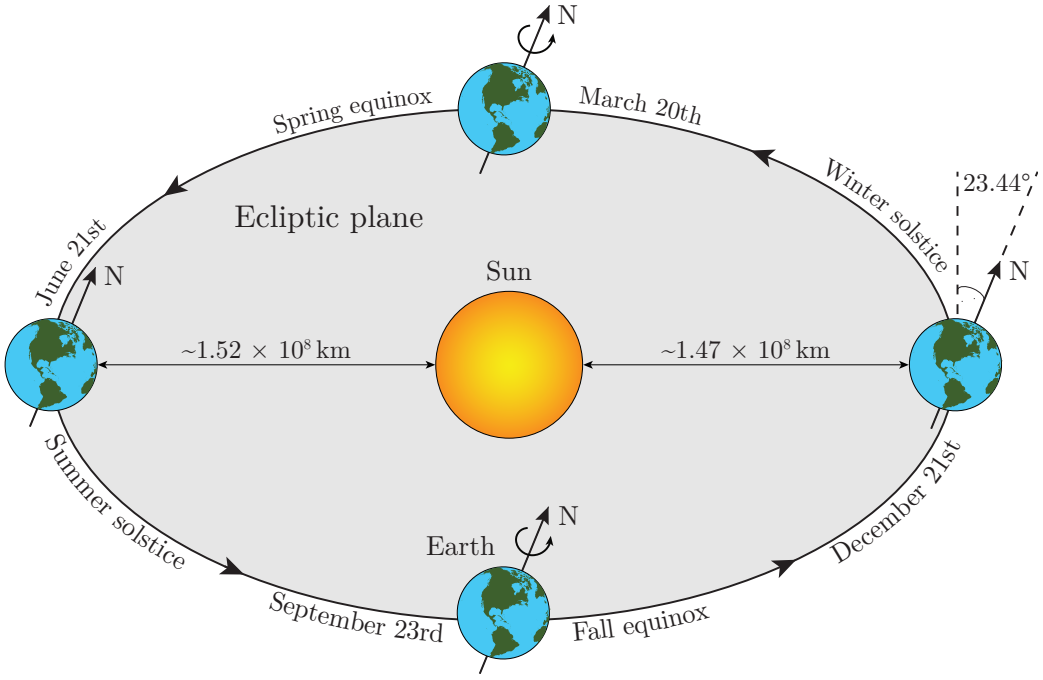

Figure 2.3: The earth's rotational axis is tilted by 23.44° with respect to its orbital plane (ecliptic plane). In the northern hemisphere the earth is tilted toward the sun during summer and away from the sun during winter. It takes the earth 24 hours to make one revolution about its north-south axis.

From an observer on the earth, the sun and other stars appear to be moving on the celestial sphere, as shown in Figure 2.4. The celestial sphere makes a complete revolution in a clockwise direction in 24 hours, or equivalently it rotates at a rate of 15° per hour. The position of any celestial body within the celestial sphere can be defined by a spherical coordinate system. In Figure 2.4 the sun's position is determined by the sun-earth distance, the right ascension, and the declination. The right ascension is the angle between the projection of sun's current position onto the equatorial plane and the sun's position at spring equinox, when the ecliptic and the equatorial planes intersect. The sun moves in a counterclockwise direction with respect to the celestial sphere and makes a full revolution once a year, hence the right ascension varies from 0 to 360°.

The equator of the celestial sphere coincides with the earth's equator in the equatorial plane. The angle between the equatorial plane and the ecliptic plane defines the declination angle of the sun. The declination angle varies from -23.44 to 23.44° throughout the year, with the minimum and the maximum being at winter and summer solstices, respectively. In Figure 2.4 the sun is at summer solstice as evident by a 90° right ascension angle.

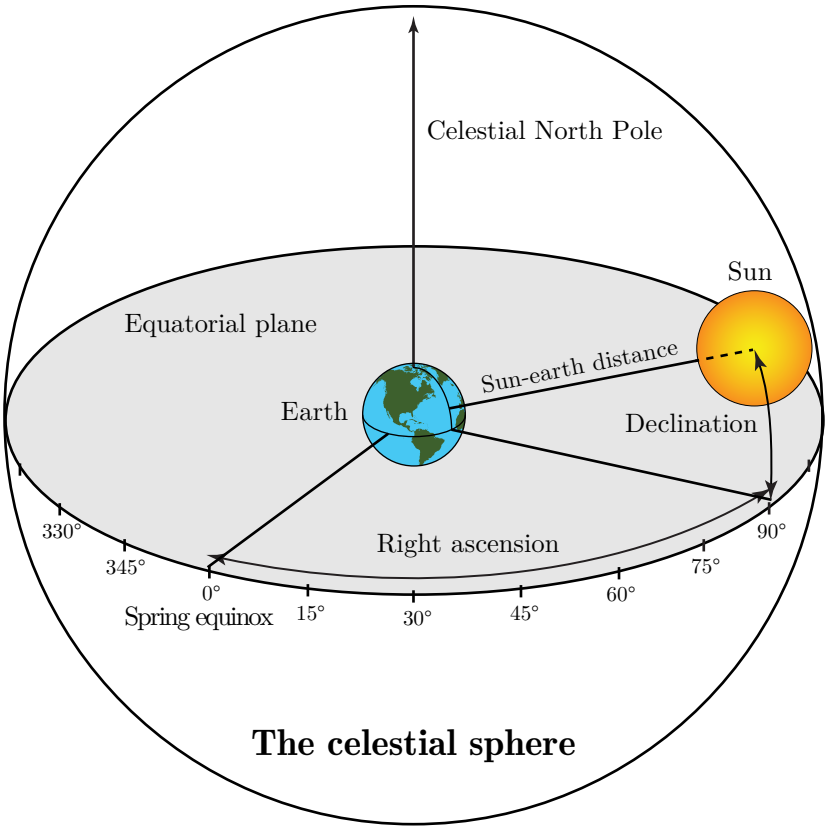

Figure 2.4: Representation of the celestial sphere where the position of the sun is defined by the sun-earth distance, the right ascension, and the declination angle. (Adapted from [4].)

The illustration of the celestial sphere can be extended to an observer at any latitude. Figure 2.5 demonstrates the orientation of the celestial sphere from the perspective of an observer in Ottawa, Canada, where it is tilted by latitude 45.4° with respect to the north. As one moves closer toward the equator, the angle between the celestial North Pole and the observer's north decreases until eventually at the equator it becomes 0°, and the scenario in Figure 2.4 is achieved. The sun's apparent motion across the sky reaches its highest altitude at local solar noon, which is always due south in the northern hemisphere. This point in time is defined as the intersection of the celestial sphere's equatorial plane and the local meridional plane. The latter lies in the plane of the page and is defined by three points: due north, due south, and the zenith. The local meridional plane is perpendicular to the east-west axis and it coincides with the longitude of the observer. At solar noon the local hour angle is equal to zero. The hour angle is the time remaining until the sun reaches the local solar noon, or time elapsed after the solar noon, where each hour represents the rotation of the celestial sphere by 15°. By convention, the hour angle is negative before solar noon and is positive after solar noon. Figure 2.5 shows the sun's apparent motion in a clockwise direction throughout the day.

Ultimately, the goal is to relate the celestial coordinates, right ascension and declination, to a more convenient local coordinate system, which is defined by the specific longitude and latitude. To accomplish this task, a time correction, known as the equation of time, must be applied. The earth rotates counterclockwise about its axis and at the same time it orbits the sun on the elliptical path in the same direction (prograde motion). As a result, the duration of the solar day, which is a length of time between two consecutive solar noons, varies throughout the year. Specifically, in one day the earth moves counterclockwise $1/365.25^{\text{th}}$ of the way around the sun. If the earth's orbit was circular, the solar day would be 24 hours / 365.25 = 3.94 minutes shorter than the sidereal day (24 hours long). However, due to the elliptical nature of the earth's orbit, the correction is more complex. The approximation to the equation of time, which is measured in minutes, is taken from [5]:

$$E = 9.87 \cdot \sin(2B) - 7.53 \cdot \cos(B) - 1.5 \cdot \sin(B), \tag{2.5}$$

where

$$B = \frac{360}{364} \cdot (n - 81) \qquad \text{(degrees)}, \tag{2.6}$$

where n is the day number and $n = 0$ corresponds to January 1^{st}. The variation of the equation of time throughout the year is shown in Figure 2.6. For example, on September 14^{th} the solar noon occurs 5 minutes after the noon of the local solar time. Furthermore, Figure 2.7 shows the solar analemma, which represents the change in sun's position over the year at the same time of the day for a specific location.

If the earth had a circular orbit and it didn't have axial tilt, the sun would always appear due south at midday or 12:00 local solar time. In addition, the local solar time rarely matches the local standard time (or civil time) due to human adjustments: timezones and daylight saving. For example, Toronto, Canada (79.4° W, 43.7° N), is 5 hours west of Greenwich, England if daylight saving is not in effect. Since the earth rotates longitudinally 15° per hour, this implies that the local solar noon is offset from the local noon or meridian by $79.4° - 15°/\text{ hour} \cdot 5 \text{ hours} = 4.4°$ or 17.6 minutes, due to the timezone effect. On the other hand, Ottawa, Canada (75.7° W, 45.4° N), is only affected by 2.8 minutes.

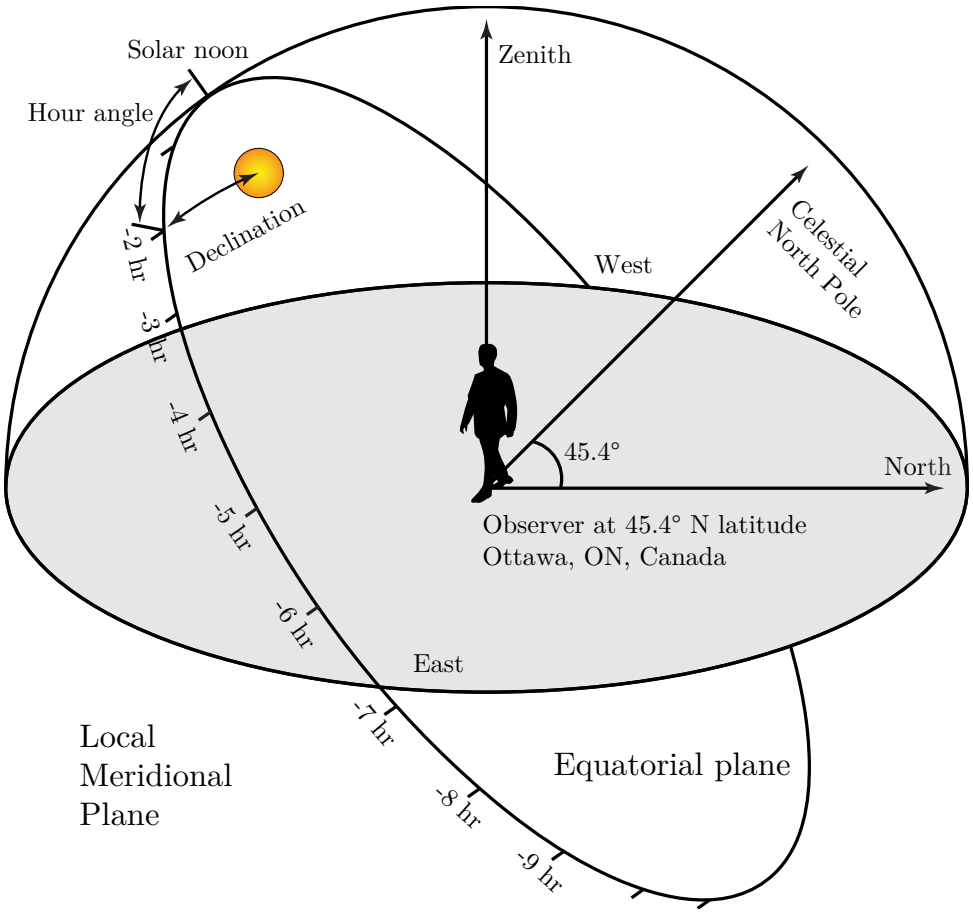

Figure 2.5: Illustration of the celestial sphere from the observer's perspective in Ottawa, Canada, at 45.4° N latitude. The hour angle indicates the sun is 2 hours behind the solar noon, which is characterized by the intersection of equatorial plane of the celestial sphere and the local meridional plane. The latter is defined by the zenith line, which is normal to the earth's surface, and the north-south axis. (Adapted from [4].)

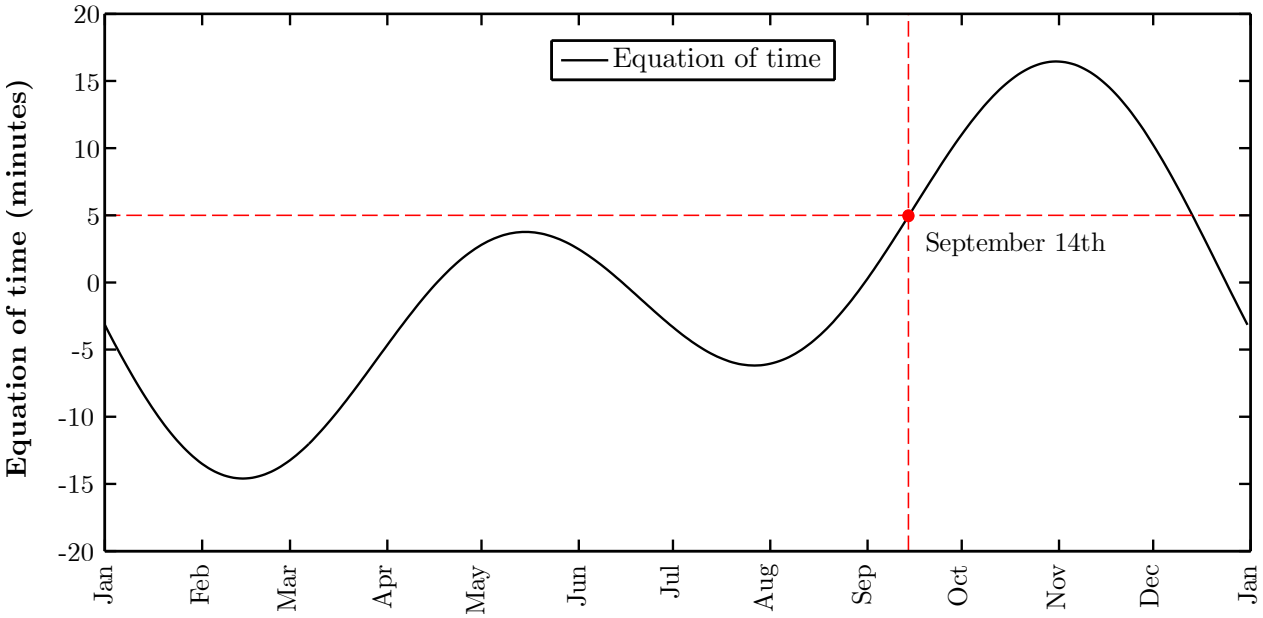

Figure 2.6: The equation of time compensates for the difference between the solar day and the siderial day due to the earth's elliptical orbit and obliquity. For example, on September 14th the sun will appear due south 5 minutes after the local solar noon.

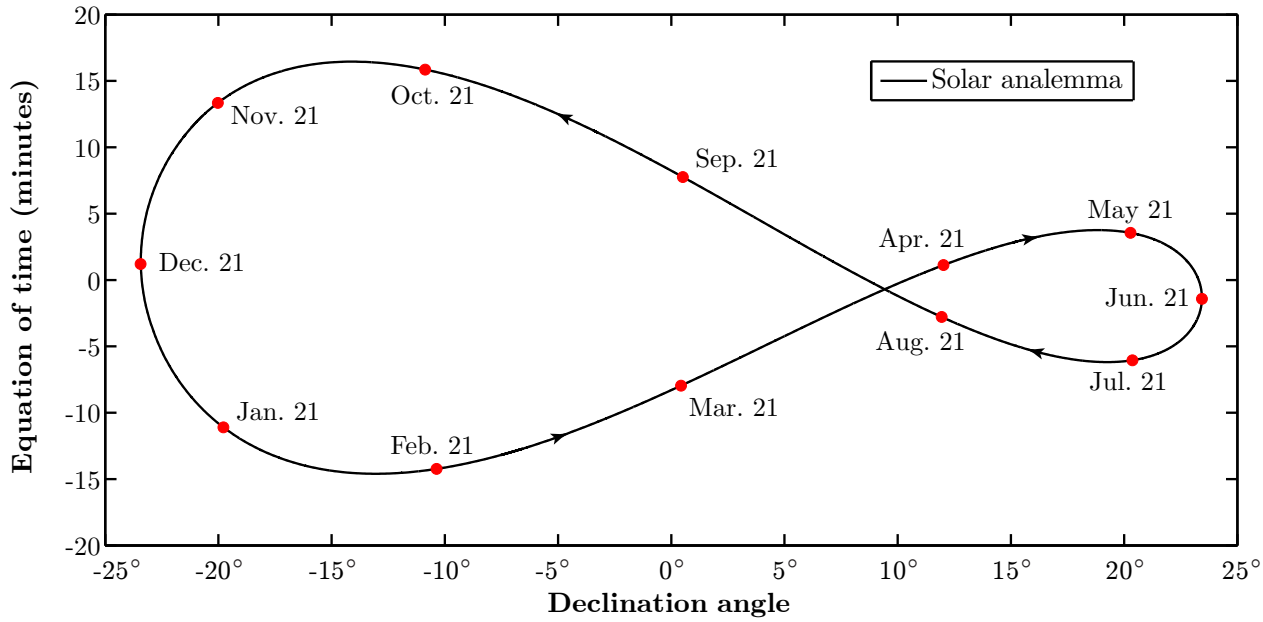

Figure 2.7: The plot of equation of time versus the solar declination angle is known as the solar analemma. It denotes the change in the sun's mean position at the same time of the day throughout the year from an observer's perspective.

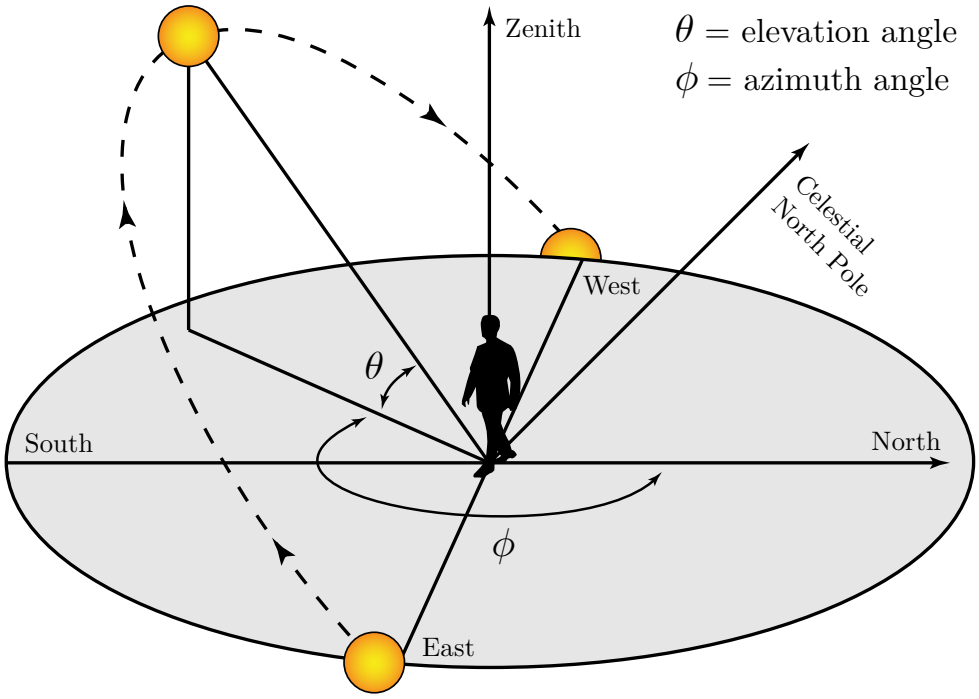

Figure 2.8: The azimuth and elevation angles define the sun's position with respect to the local horizontal plane of the observer. The azimuth angle, ϕ, is measured clockwise from north to the projection of the sun's position onto the local horizontal plane. The elevation angle, θ, is measured from the horizontal plane up. (Adapted from [4].)

2.4 Local solar coordinates

The local coordinate system, presented in Figure 2.8, determines the sun's position at any time during the day. From an observer's point of view, two variables: the azimuth and the elevation angles, are needed to define the sun's position at any latitude and longitude. The azimuth angle, ϕ, is measured clockwise from north to the projection of the sun onto the local horizontal plane, as shown in Figure 2.8. Similar to the right ascension, the azimuth angle spans 0° to 360°, where 0° corresponds to due north. Some conventions have the azimuth angle spanning from -180° to 180°, where 0° is due south. Before solar noon, the azimuth angle is positive, while after solar noon, it is negative. Throughout this thesis the first convention is used.

The elevation angle, θ, denotes the altitude of the sun above the local horizontal plane. Commonly, the zenith angle, which is measured from the zenith line down, is used in place of the elevation angle. However, only knowledge of one is required to deduce the other, as the sum of both adds up to 90°. Throughout this text, both the elevation and zenith

angles terminology is used for convenience wherever appropriate. Lastly, the maximum daily elevation angle occurs at solar noon, while the yearly maximum is at summer solstice. Only the latitudes between the Tropic of Cancer (23.44° N) and the Tropic of Capricorn (23.44° S) experience the sun being directly overhead ($\theta = 90°$) at least once a year. In Ottawa, Canada, the maximum and the minimum elevation angles are $\theta_{\max} = 90° - 45.4° + 23.4° = 68.0°$ and $\theta_{\min} = 90° - 45.4° - 23.4° = 21.2°$, appearing on the solar noon on summer and winter solstices, respectively.

2.5 Solar position calculation

Accurate algorithms capable of determining the azimuth and elevation angles of the sun at the observer's latitude, longitude, and local standard time, are vital for predicting the amount of solar irradiance reaching the earth's surface. This prediction becomes especially important for PV panels operating on tracking systems as the latter must actively follow the sun throughout the day to maximize power production from the PV panels. There are numerous solar position algorithms (SPAs) with varying degrees of accuracy at ones disposal. For this thesis work, the most accurate algorithm available is used from the National Renewable Energy Laboratorty (NREL), titled "Solar position algorithm for solar radiation applications" [6]. This SPA has an accuracy of $\pm 0.0003°$ for the calculation of the azimuth and elevation angles from the year 2000 BC to AD 6000.

One of the helpful ways to summarize the position of the sun throughout the year is to plot the azimuth versus the elevation angle for selected days between summer and winter solstices at a specific location. Figure 2.9 demonstrates the sun path chart for Ottawa, Canada, from the NREL SPA's calculated solar parameters.

2.6 The influence of the atmosphere

The solar irradiance at the ground level is a dynamic energy resource that fluctuates in intensity and spectrum due to varying geographical and meteorological conditions. AM, aerosols, atmospheric gases (oxygen, ozone, water vapour, etc.), and numerous pollutants act in conjunction as a continuously varying filter of the extraterrestrial solar irradiance. In order to understand the extinction of sunlight through the atmosphere, it is important to parameterize the effects of each atmospheric constituent. This subsection takes a deeper look at how individual components of the atmosphere affect the solar spectrum.

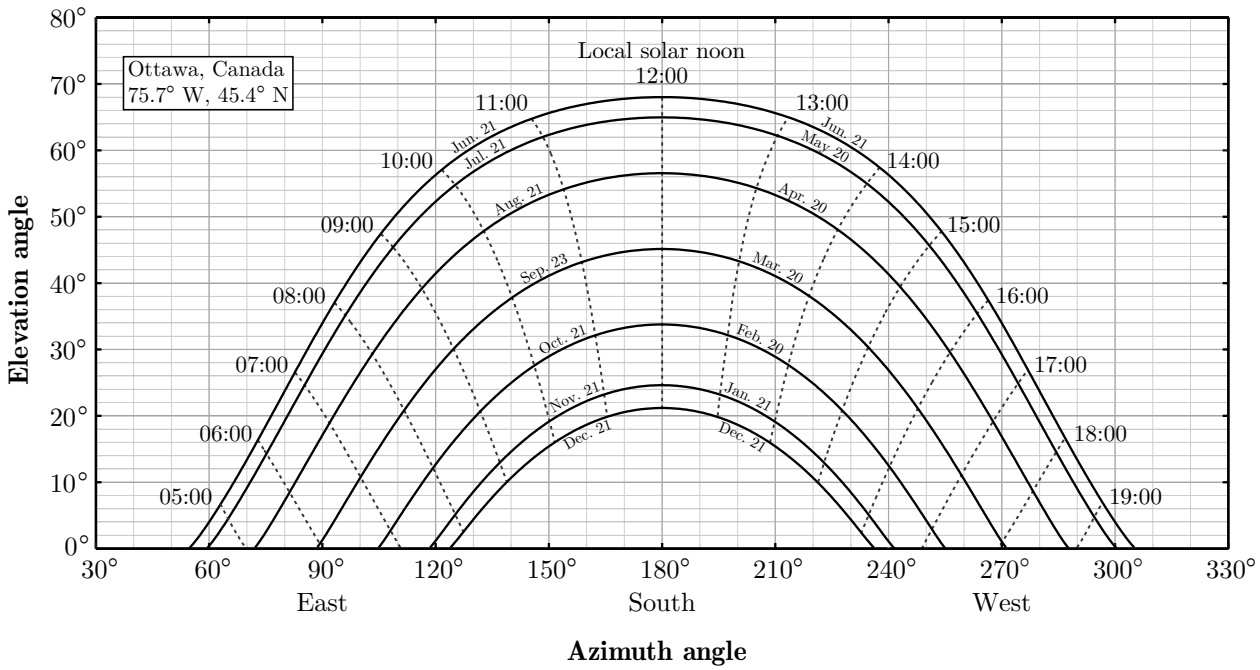

Figure 2.9: The sun path plot for Ottawa, Canada, in 2014. On the summer solstice (June 21st) the azimuth angle varies from about 55° to 305°, while during the winter solstice (December 21st) it changes from approximately 125° to 235° at sunrises and sunsets, respectively. The elevation angle at the solar noon changes from 21.18° to 68.02° between the solstices. At the spring and fall equinoxes (March 20th and September 23rd, respectively) the sunrise and sunset are due east and west with azimuth angles of 90 and 270°, respectively. The time is reported as the local solar time. (Style is adapted from [4].)

2.6.1 Direct normal, diffuse and global irradiance

On a clear-sky day the vast majority of the solar irradiance passes through the atmosphere unabsorbed and strikes the earth's surface directly at the local elevation angle of the sun. This type of irradiance is termed direct normal irradiance (DNI). For example, if on a cloudless day a PV panel is oriented to the azimuth and elevation angles of the sun, the nearly perpendicular rays that shine on the panel are part of the DNI beam. The DNI beam is not perfectly collimated because the sun is a spherical source with a diameter of 1.392×10^6 km located on average 1.496×10^8 km away from the earth. This geometry results in the sunlight collimation (full angle) being approximately 0.533° (or half angle of 0.267°) at the mean sun-earth distance, as demonstrated in Figure 2.10. Furthermore, the collimation of the DNI beam fluctuates between 0.525° and 0.542° at the aphelion and perihelion of the sun-earth orbit, respectively. However, due to radiation scattering by the atmosphere, the instruments

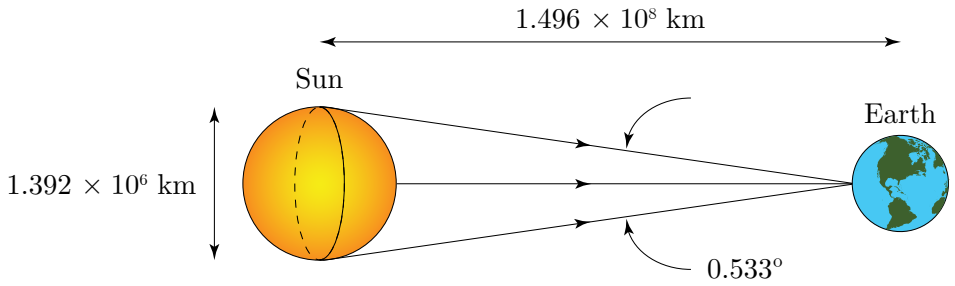

Figure 2.10: The collimation of the DNI cone reaching the earth is determined by the sun's diameter and the sun-earth distance. On average the full angle of the direct beam from the sun is 0.533°.

that measure DNI have the aperture opening to accept sunlight with half angle of 1° to 10° depending on the application [7]. The radiation that is mixed with the direct beam of sunlight is called the circumsolar radiation and it strongly depends on the atmospheric conditions. On a hazy day, when the circumsolar radiation is high, the sun's aureole appears larger to an observer than on a clear day due to sunlight scattering.

The remainder of the solar irradiance, which is not a part of the DNI beam, is scattered and/or reflected by the atmosphere and clouds in random directions, as shown in Figure 2.11. Some portion of the scattered sunlight is reflected back into the space, and the remainder makes its way to the earth. The scattered radiation that reaches the surface of the earth is commonly referred to as diffuse horizontal irradiance (DHI), which by definition includes the circumsolar radiation. The reflection from the ground (albedo) or any other object within the hemispherical view of an observer also contribute to DHI. For example, in winter the snow-covered areas have a high albedo and as a result a significant portion of DHI comes from this source.

The horizontally mounted surface is exposed to the combination of DNI and DHI. This type of solar irradiance, which comes from any direction within the observer's hemisphere, is defined as global horizontal irradiance. More specifically, it is equal to the product of DNI and the sine of the elevation angle, θ, plus DHI:

$$\text{GHI} = \text{DNI} \cdot \sin(\theta) + \text{DHI}. \tag{2.7}$$

In some instances GHI can momentarily exceed the solar constant value of 1366.1 W/m^2 due to lensing effects. On a partially cloudy day, if the direct beam of the sunlight is unaffected by clouds and a large portion is reflected by clouds to an observer, the instantaneous GHI reading can be abnormally high.

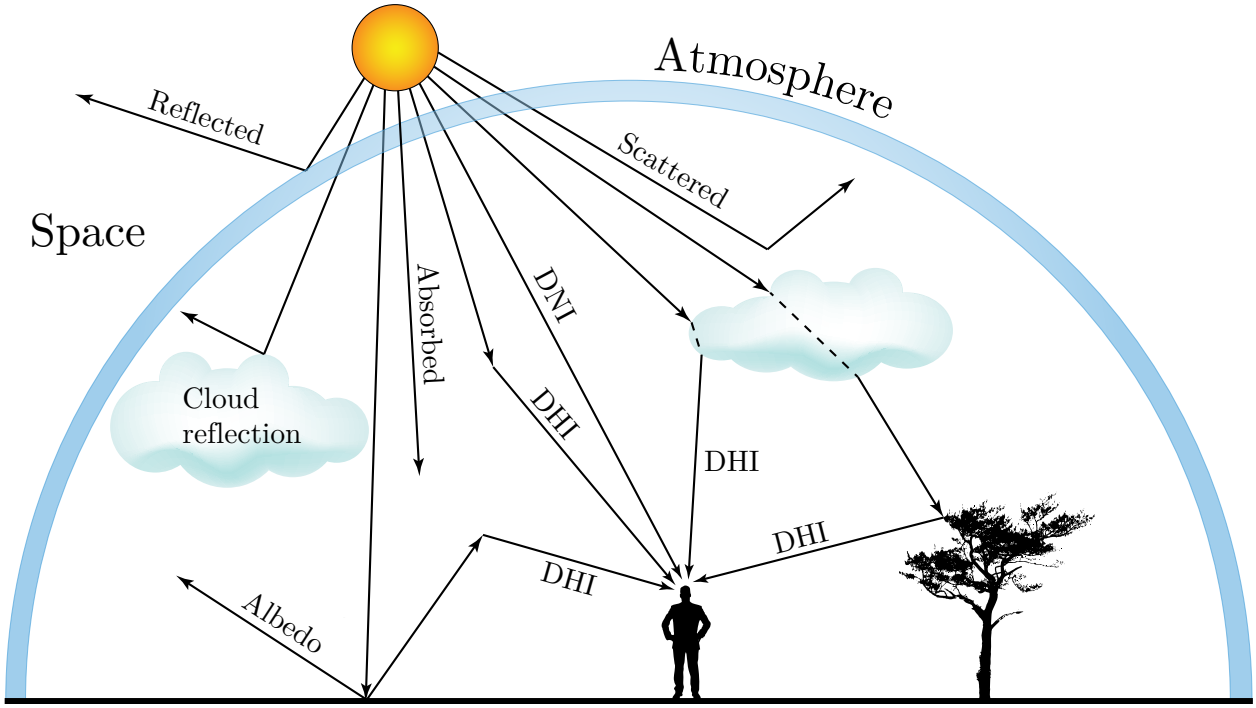

Figure 2.11: The effect of the atmosphere and clouds on the solar irradiance components. The unscattered and unabsorbed radiation reaching an observer on the earth is called DNI. On the other hand, DHI arises from the scattering of sunlight due to the atmosphere and clouds, and/or the reflection from the ground (albedo) or any other object within the hemispherical view of the observer. The combination of the projected DNI onto the horizontal surface plus cumulative DHI yields GHI.

2.6.2 Air mass

AM is a significant factor affecting the solar spectral resource at the earth's surface. It refers to the amount of "equivalent atmospheres" or multiples of AM1.0 the sunlight has to travel before it reaches the earth, as demonstrated in Figure 2.12. AM1.0 refers to the path-length through the atmosphere at the sun elevation angle of 90°, in other words, when the sun is directly overhead. The simplistic geometric expression for the AM is

$$AM = 1/\sin(\theta), \tag{2.8}$$

where θ is the elevation angle of the sun. Figure 2.13 shows the simulated effect of AM on the spectral DNI from early morning and up to solar noon in local standard time. During this interval the AM decreases until it reaches the lowest value of the day at the solar noon. The simulations are performed using a Simple Model of the Atmospheric Radiative Transfer

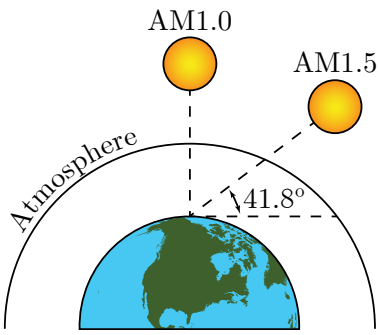

Figure 2.12: The amount of the atmosphere the solar radiation travels through before it reaches the earth depends on the position of the sun with respect to an observer. As the elevation angle decreases, the AM increases, resulting in additional sunlight absorption and scattering.

of Sunshine (SMARTS), version 2.9.2, developed by C. Gueymard at the Florida Solar Energy Center [7, 8]. SMARTS borrows absorption profiles and recent spectroscopic data for some gases from the Air Force Geophysical Laboratory Moderate Resolution Transmission model (MODTRAN), version 4.0, which serves as the community standard for atmospheric modelling [9, 10]. The spectral accuracy of SMARTS is within ±2% of MODTRAN [11]. Throughout this thesis work, all simulations of the spectral irradiance are performed with aid of SMARTS unless otherwise specified.

The solar spectrum reaching the earth's surface varies with location as influenced by the atmospheric conditions, such as cloud cover, aerosols, water vapour, and ozone content. As a result, standard spectra exist to assist many applications that require theoretical or practical evaluation of the solar spectral irradiance effects, such as solar cell design or PV module testing. The most popular standards are AM1.5D and AM1.5G ($\theta = 41.8°$) as defined by the American Society for Testing and Materials (ASTM) with designation G173-03. AM1.5D is the standard for the direct normal plus circumsolar (2.9° half angle) spectral irradiance with normalized power of 900.1 W/m^2, while AM1.5G is the reference for the global spectral irradiance for a 37° tilted, south-facing horizontal surface with normalized power of 1000.4 W/m^2 [12]. Both spectra are shown in Figure 2.14 along with the AM0 spectral irradiance standard from the ASTM with designation E490-00a. The AM1.5D and AM1.5G spectra differ considerably from the AM0 spectrum and demonstrate the profound effect of the atmosphere on the solar radiation.

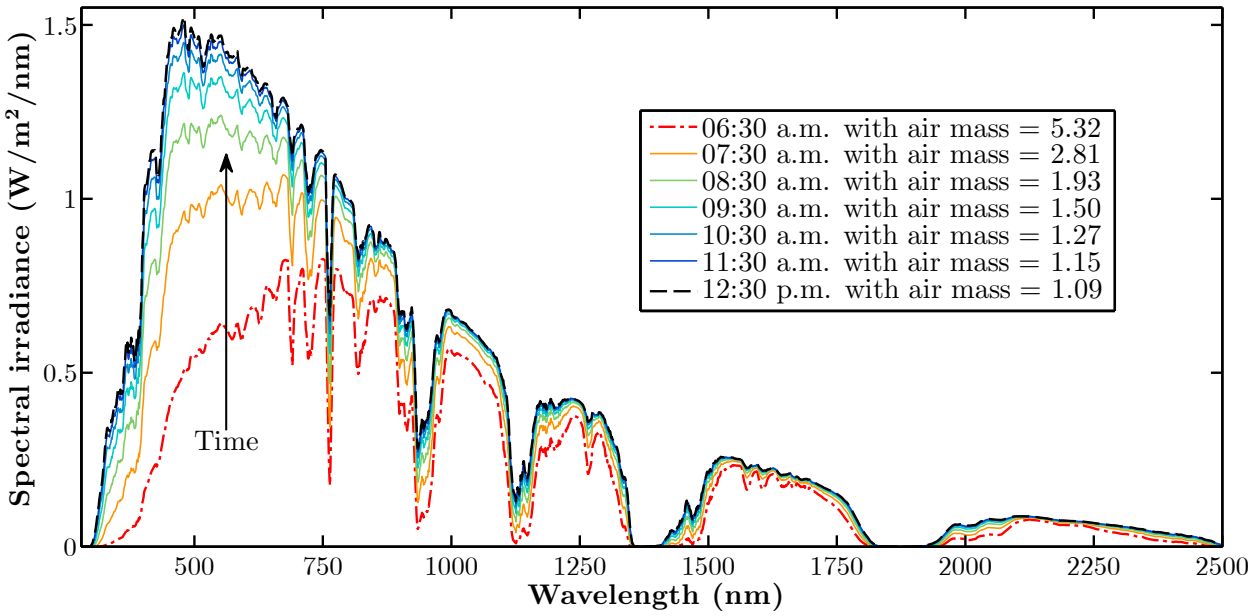

Figure 2.13: Simulated effect of AM on the spectral DNI for Ottawa, Canada, during the summer solstice on June 21st, 2013. As the AM increases, the short-wavelength irradiance is impacted more than the long-wavelength one.

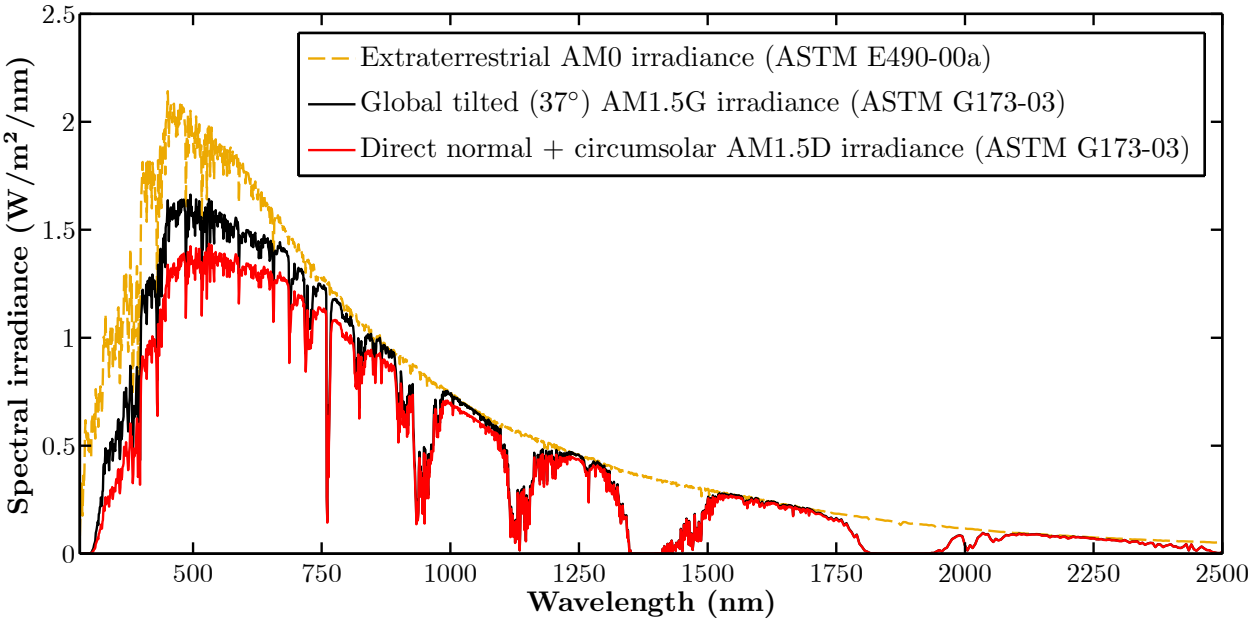

Figure 2.14: The ASTM developed standard spectra AM1.5D and AM1.5G to aid comparison of PV module performance at different times and locations. These standards also demonstrate the profound effect of the earth's atmosphere on the spectral irradiance as compared to the extraterrestrial AM0 spectrum.

Table 2.1: Parameterization of the AM1.5D spectrum losses through the atmosphere.

Atmospheric process	**Solar radiation losses (%)**
Trace gases absorption	0.2
Ozone absorption	1.7
Mixed gases absorption	1.8
Aerosols extinction	7.1
Rayleigh scattering	10.5
Water vapour absorption	12.1
Total loss	33.4

The incident power difference between AM0 and AM1.5D spectra is 33% in the 280–4000 nm range. To understand where the power loss occurs, it is useful to isolate the effect of each atmospheric constituent. Figure 2.15 depicts the parameterized solar radiation losses of the AM0 spectrum traversing through the atmosphere under AM1.5D conditions. In total, six atmospheric processes are used to quantify solar radiation losses, as summarized in Table 2.1. Rayleigh scattering and water vapour absorption are the main factors for the solar spectrum extinction, with 10.5% and 12.1% of the AM0 spectrum being lost due to these processes, respectively. Furthermore, Figure 2.16 demonstrates the normalized breakdown for the solar radiation losses associated with each atmospheric constituent. For example, at 500 nm, the majority of the solar spectrum losses occur due to Rayleigh scattering (58.2%) and aerosol extinction (35.6%). The ultraviolet (UV) (under 400 nm) and visible spectral ranges (400–700 nm) are dominated by Rayleigh scattering, ozone absorption and aerosol extinction, while water vapour and mixed gases have a major influence in the infrared (IR) range (over 700 nm).

The present state-of-the-art MJSCs can only harvest photons with wavelengths of up to 1800 nm due to limitations in material absorption. By comparison, conventional Si solar cells are optically transparent to wavelengths greater than 1100 nm. Therefore, for practical applications the relative weight of some atmospheric constituents deviates from Table 2.1. For Si applications in the 300–1100 nm range, which contains approximately 75% of the AM0 incident power, Rayleigh scattering, aerosol extinction, and ozone absorption dominate as loss mechanisms. On the other hand, the aforementioned processes plus water vapour absorption are responsible for the majority of solar radiation extinction in the 300–1800 nm range, which the MJSC applications currently utilize. The impact of the solar spectrum on a solar cell's performance is discussed in detail in Chapter 4.

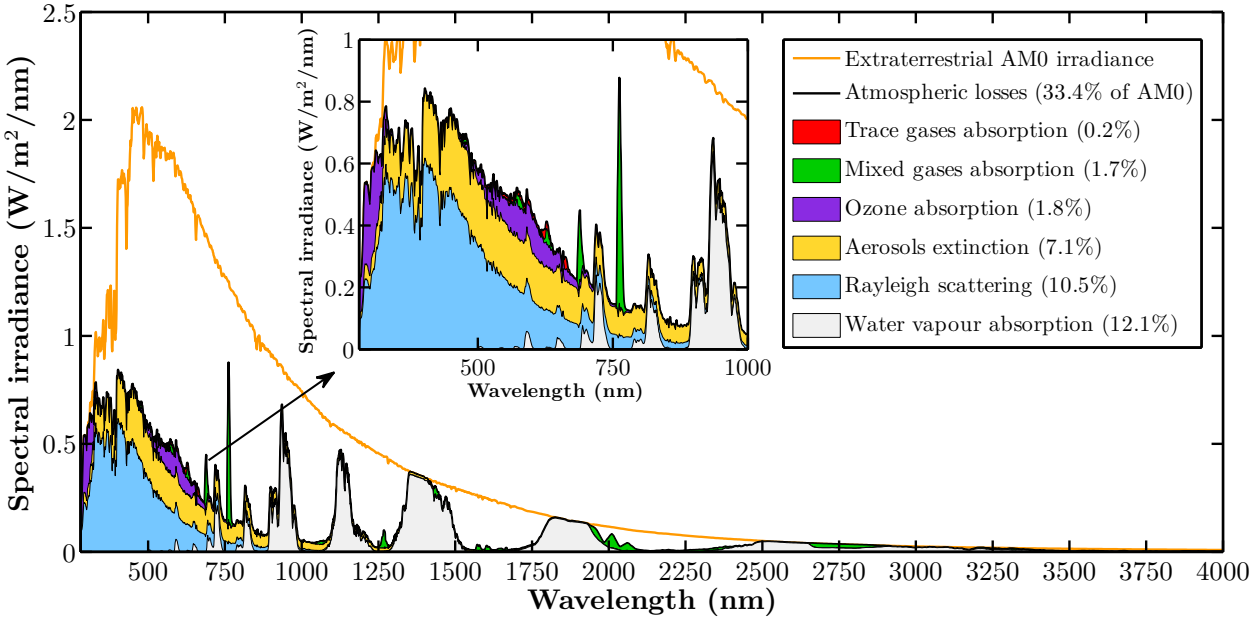

Figure 2.15: The parameterization of the solar radiation losses under AM1.5D conditions. In this case the AM0 spectrum sheds 33.4% of its incident power before reaching the earth's surface.

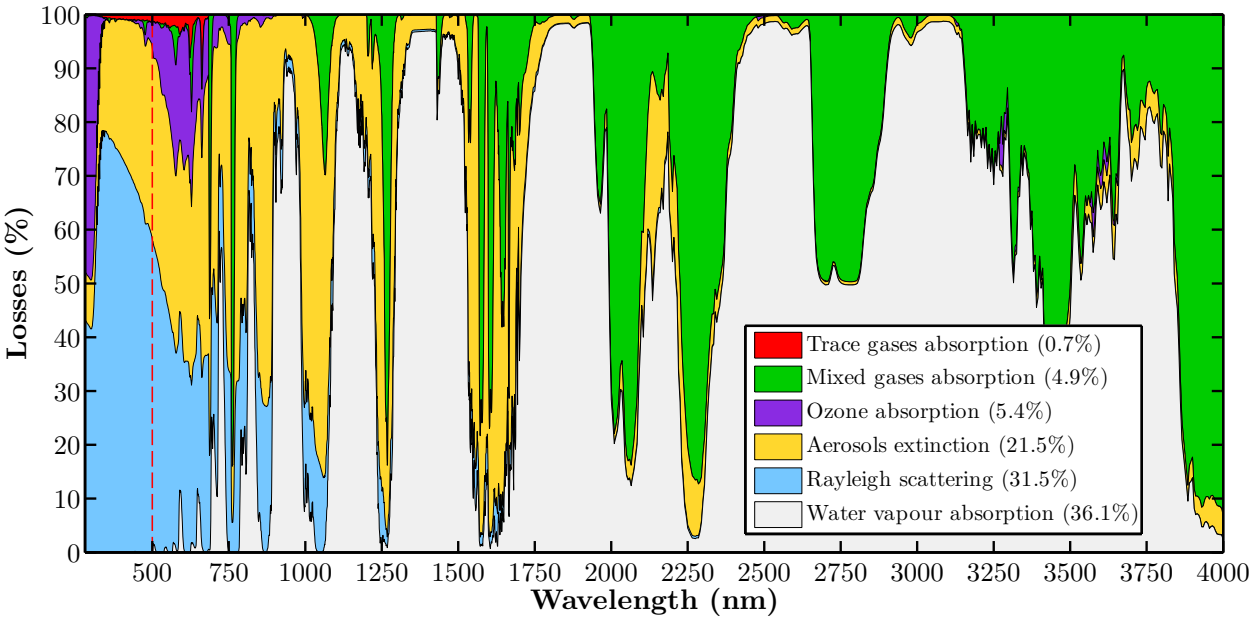

Figure 2.16: The normalized breakdown of the solar radiation losses arising from the atmospheric processes. In the ultraviolet and visible spectral ranges the dominant loss mechanisms are Rayleigh scattering, aerosol extinction and ozone absorption, while in the infrared – water vapour and mixed gases absorptions.

2.6.3 Quantification of gas abundances

The amount or abundance of any gas in the atmosphere can be defined by either the concentration or the mixing ratio. The concentration of a gas is defined as the amount of a gas per volume of air at specific temperature and pressure:

$$c_{\mathrm{m}} = \frac{\text{Mass of gas}}{\text{Volume of air}} \quad \text{or} \quad c_{\mathrm{n}} = \frac{\text{Number of molecules}}{\text{Volume of air}}, \tag{2.9}$$

where c_{m} is the mass concentration and c_{n} is the number density of a gas.

The mixing ratio of a gas is defined as the amount of a gas per amount of air plus the gas in question:

$$\chi_{\mathrm{V}} = \frac{\text{Unit of volume of gas}}{10^6 \text{ unit volumes of air + gas}} \text{ (ppmv)}. \tag{2.10}$$

For the atmospheric gases, χ_{V} is typically expressed in units of parts per million by volume (ppmv), although parts per billion and per trillion by volume, ppbv and pptv, respectively, are also used. The mixing ratio does not depend on the temperature and pressure.

Conversion between the concentration and the mixing ratio is often required. For specific temperature and pressure, the mixing ratio, χ_{V}, is expressed from [13] as

$$\chi_{\mathrm{V}} = c_{\mathrm{n}} \cdot \frac{1}{N_{\mathrm{A}}} \cdot \frac{RT}{P} \quad \text{or} \quad \chi_{\mathrm{V}} = c_{\mathrm{m}} \cdot \frac{1}{M} \cdot \frac{RT}{P}, \tag{2.11}$$

where N_{A} is Avogadro constant, T and P are temperature and pressure, respectively, at which c_{n} or c_{m} is measured, R is the ideal gas constant, and M is the molar mass of the gas in g/mol. Consequently, c_{n} and c_{m} are defined in terms of χ_{V} as

$$c_{\mathrm{n}} = \chi_{\mathrm{V}} \cdot N_{\mathrm{A}} \cdot \frac{P}{RT} \quad \text{and} \quad c_{\mathrm{m}} = \chi_{\mathrm{V}} \cdot M \cdot \frac{P}{RT}. \tag{2.12}$$

For example, if the mixing ratio of ozone (O_3) is equal to 20 ppbv at standard ambient temperature and pressure (SATP) of $T = 298.15$ K and $P = 100$ kPa, Equation 2.12 can be used to compute the mass concentration, c_{m}, of O_3 as 38.7 μg/m^3 and the number density, c_{n}, of O_3 as 4.86×10^{11} molecules/cm^3.

For some gases in the atmosphere the mixing ratio does not stay constant with increasing altitude, which is the case for O_3, as shown in Figure 2.17. Therefore, to quantify the total amount of O_3 in the atmosphere, the total column density, Q_{n}, and the total mass column density, Q_{m}, are used, where the number density and the mass concentration, respectively, are integrated vertically from the earth's surface to infinity

$$Q_{\mathrm{n}} = \int_0^\infty c_{\mathrm{n}}(z) \cdot dz \quad \text{and} \quad Q_{\mathrm{m}} = \int_0^\infty c_{\mathrm{m}}(z) \cdot dz. \tag{2.13}$$

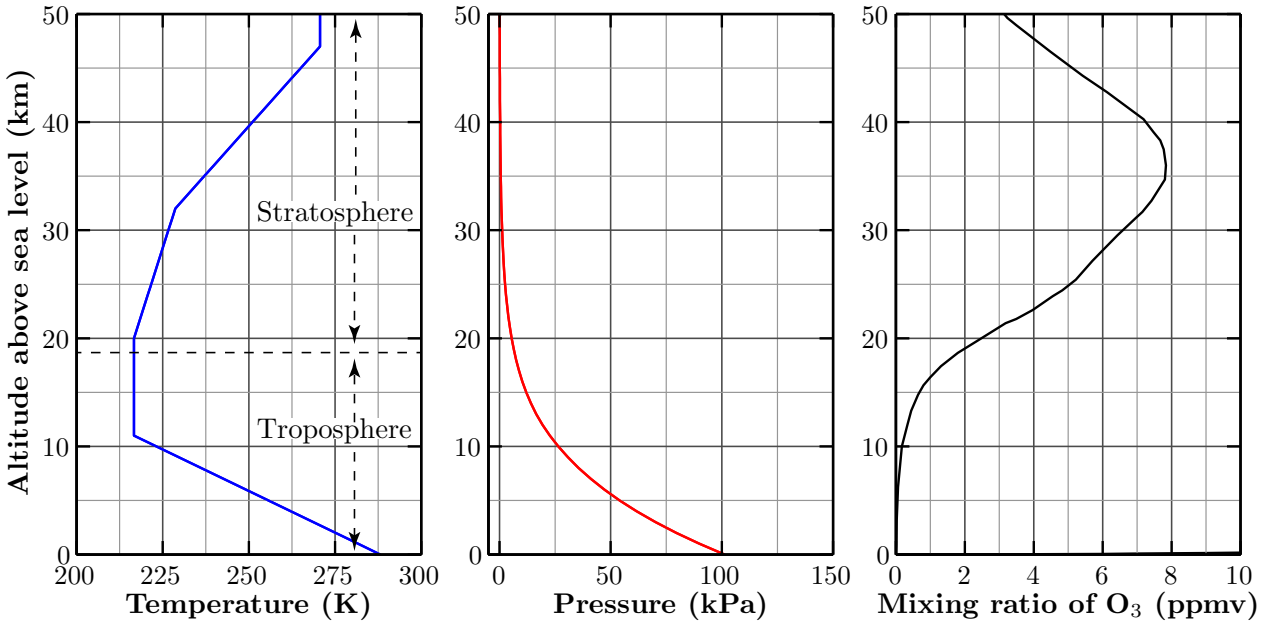

Figure 2.17: U.S. standard atmosphere of 1976 from [14]. The temperature, pressure, and mixing ratio of ozone profiles are shown for the altitude between 0 km and 50 km above sea level. As demonstrated, the vast majority of the atmosphere lies below an altitude of 50 km.

Q_{n} and Q_{m} are measured in units of molecules/m^2 and µg/m^2 or equivalent units, respectively. Since the mixing ratio profile of O_3 is known, Equations 2.12 and 2.13 can be used to calculate the total column density, Q_{n}, of O_3 with the temperature and pressure profiles specified in Figure 2.17, which represents the U.S. standard atmosphere of 1976. The total column density in this case is equal to the sum of all O_3 molecules above a square metre of surface between 0 km and 50 km altitude and it is computed as 9.289×10^{22} molecules/m^2. A more common way to express the column abundance of O_3 is through the use of Dobson units (DU). One DU is equivalent to 10 µm column of a gas above a square metre of surface at the standard temperature and pressure (STP) with $T = 273.15$ K and $P = 101.325$ kPA. The total column density, Q_{n}, and the path-length, p_i, of a gas i are related through

$$p_i = \frac{Q_{\mathrm{n}}}{N_{\mathrm{L}}}, \tag{2.14}$$

where N_{L} is the Loschmidt constant. The column density of one DU is 2.6867774×10^{20} mole- cules/m^2 for an ideal gas. Therefore, the total column abundance of O_3 in the U.S. standard atmosphere of 1976 is approximately 345.7 DU, which is consistent with [15]. That is equivalent to the same number of molecules as in a 3.457 mm high column of air at STP, which demonstrates the fragility of the ozone layer.

2.6.4 Trace and mixed gases absorption

The earth's atmosphere contains numerous gases whose mixing ratios are shown in Table 2.2. In the context of solar radiation extinction, these atmospheric gases can be divided into two categories: trace and mixed, both of which arise from either natural and/or anthropogenic sources. Trace gases have a much lower concentration in the atmosphere than the mixed gases and tend to be distributed very close to the earth's surface, typically within altitude of 1 km [8]. The most important trace gases to consider, in terms of the solar radiation extinction, are sulfur dioxide (SO_2) and nitrogen dioxide (NO_2). These gases are largely responsible for the extinction of the solar radiation in the UV and the visible spectral ranges, as demonstrated in Figure 2.18. For example, in Sarnia, Canada, the highest one hour concentrations of SO_2 and NO_2 were 0.10 ppmv and 0.06 ppmv in 2010, respectively [16]. This scenario would result in the transmission of the solar radiation due to SO_2 and NO_2 to be in between the moderate and the severe cases of pollution from Figure 2.18. Both of these gases are primarily generated from fossil fuel combustion at power generation plants, although in cities the road traffic is the main source of NO_2 [17].

Mixed gases are uniformly mixed in the atmosphere. In other words, the mixing ratio stays close to constant at all altitudes above the earth's surface, as is the case with oxygen (O_2), carbon dioxide (CO_2), and methane (CH_4) [18, 19]. O_2 is the second most abundant gas in air and is largely responsible for the solar spectrum absorption in narrow bands centred at 687, 761, and 1269 nm. CH_4 and CO_2 attenuate the solar irradiance mostly in the IR range and consequently are greenhouse gases. Other gases from Table 2.2, namely ozone (O_3) and highly variable water vapour, are addressed individually in subsequent sections due to their importance in the solar radiation extinction.

Table 2.2: Average composition of the earth's atmosphere [20].

	Volume mixing ratio	
Gas	**%**	**(ppmv)**
Nitrogen (N_2)	78.08	780,000
Oxygen (O_2)	20.95	209,500
Argon (Ar)	0.93	9,300
Water vapour (H_2O)	0.00001–4.0	0.1–40,000
Carbon dioxide (CO_2)	0.0375	375
Methane (CH_4)	0.00017	1.8
Ozone (O_3)	0.000003–0.001	0.03–10

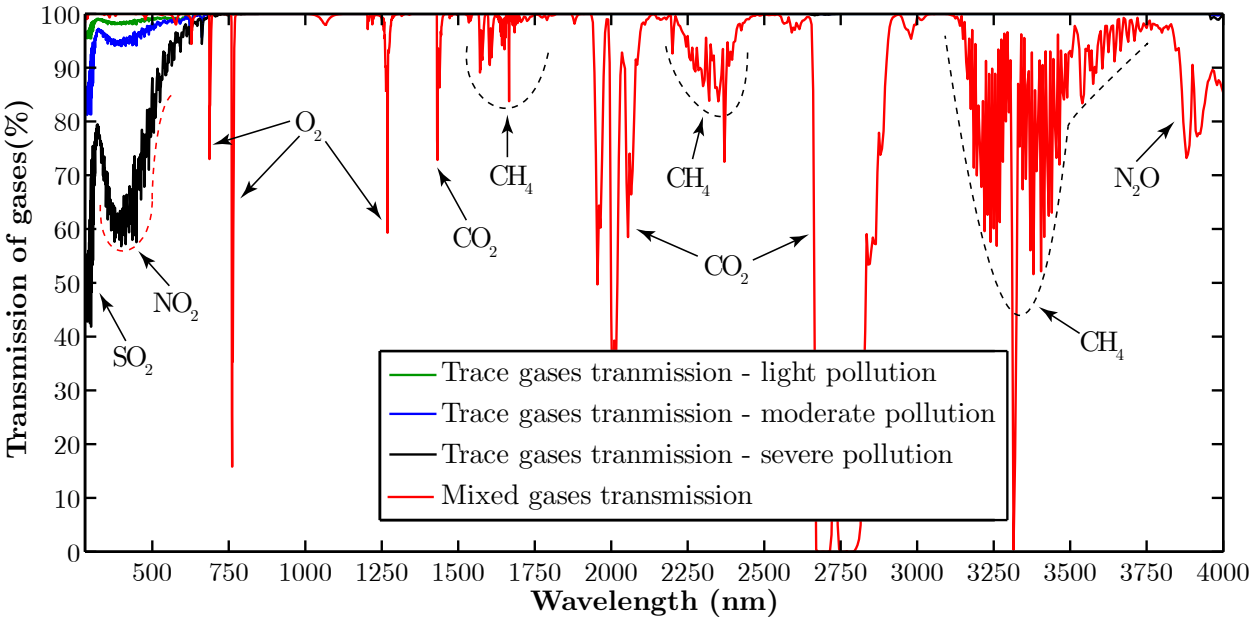

Figure 2.18: Transmission of the solar radiation through trace and mixed gases under the AM1.5D conditions. Also shown is the extinction of the solar spectrum due to different levels of pollution: light (0.01 ppmv, 0.005 ppmv), moderate (0.05 ppmv, 0.02 ppmv) and severe (0.2 ppmv, 0.2 ppmv), where (x, y) is the concentration of SO_2 and NO_2, respectively, as defined in [8]. (SMARTS simulation).

2.6.5 Ozone absorption

Ozone (O_3) is a crucial atmospheric gas for sustaining life on the earth by absorbing most of the sun's harmful UV radiation. It is most abundant in the stratosphere (18–50 km altitude) with a peak concentration of approximately 8 ppmv at about 35 km above the earth's surface, as shown in Figure 2.17. However, in the troposphere (0–18 km altitude) it is not only a component of smog, but also is poisonous to humans and plants. In 2010 the annual mean total column density of O_3 was about 287 DU between 60° S and 60° N latitudes [21]. O_3 concentration is greater at higher latitudes, with the notable exception of ozone hole over the south pole in the Antarctic. Furthermore, the total column density of O_3 has a seasonal cycle with minimum and maximum occurring around autumn and spring in the northern hemisphere, respectively. For example, in Toronto, Canada, the seasonal variability of the total column density of O_3 was on average 60 DU from 1960–1998 [22].

Figure 2.19 shows the transmission of O_3 through the atmosphere with varying total column density under AM1.5D conditions. O_3 almost completely attenuates the UV solar radiation shorter than 300 nm, while also absorbing a significant portion of the solar spectrum

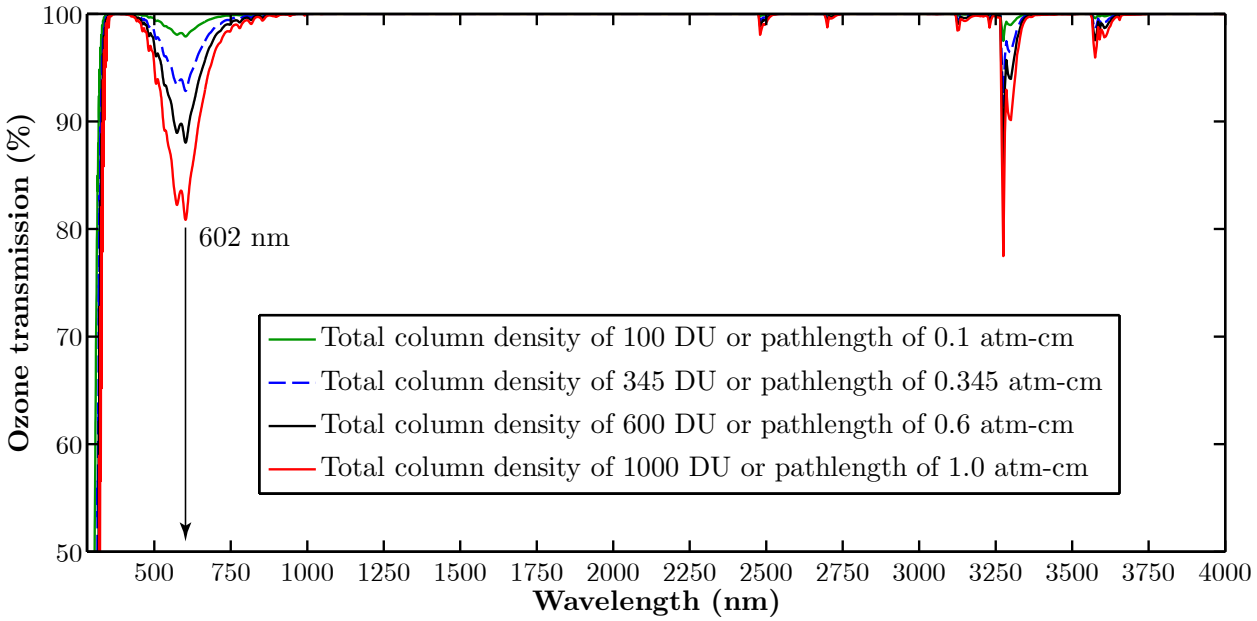

Figure 2.19: Ozone transmission through the atmosphere with varying total column density under the AM1.5D conditions. The dashed line corresponds to the column density of ozone for the U.S. standard atmosphere. The maximum absorption in visible range occurs at approximately 602 nm. Please note the y-scale has the range from 50% to 100% to emphasize the ozone absorption band in the visible range. (SMARTS simulation).

in the visible range. The peak O_3 absorption in the visible range occurs at 602 nm and for the total column density of 345 DU the solar radiation transmission for this wavelength is 92.8%.

2.6.6 Aerosol extinction

Aerosol extinction refers to the scattering and the absorption of solar radiation in the atmosphere by colloids of solid or liquid particles (aerosols) ranging in radii from around 0.001 μm to as large as 100 μm [23]. They manifest themselves in the form of haze and are generated both naturally and anthropogenically. Natural aerosols include volcanic and windblown dust, smoke from forest fires, salt from the spray of seawater, and small particles created by the chemical reactions of natural atmospheric gases. The man-made aerosols are airborne particles emitted mostly from fossil fuel combustion, such as soot (impure or amorphous carbon), ash, and sulfates. For example, Figure 2.20 shows the scanning electron microscope image of the fly ash particles, consisting mostly of silicon dioxide and calcium oxide, from a coal fired power plant.

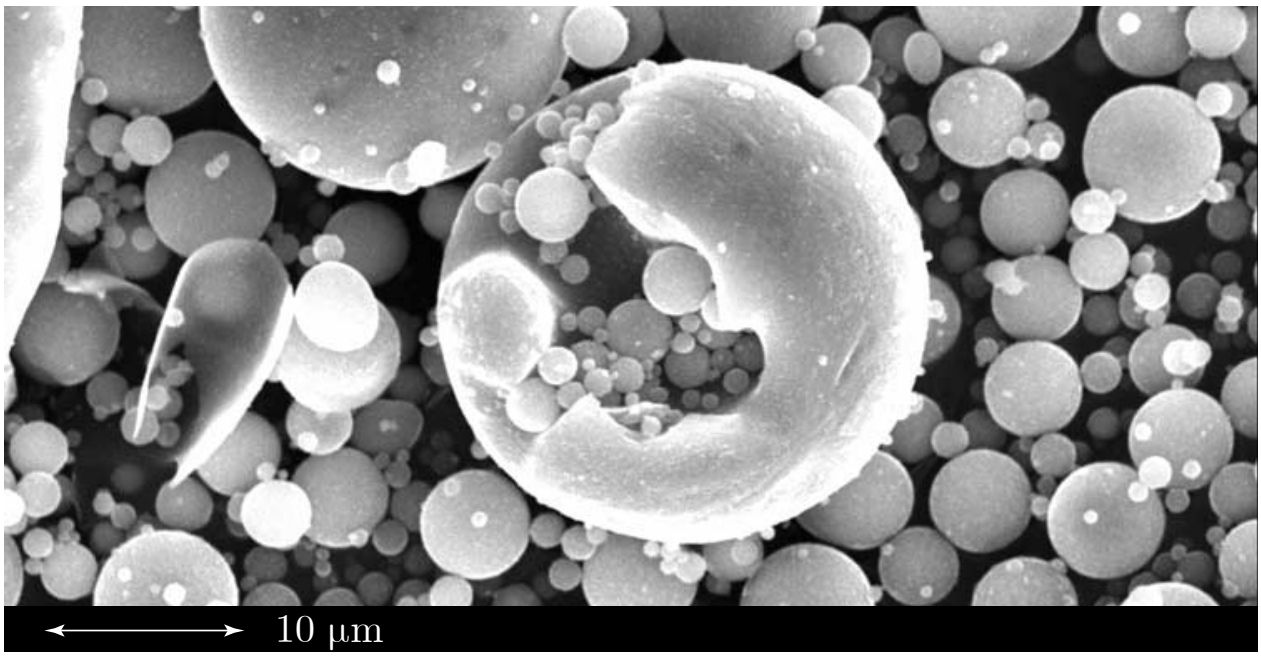

Figure 2.20: Scanning electron microscope image of fly ash from a coal power generation plant [24]. The particles are composed of silicon dioxide and calcium oxide with radii varying from about 0.5 to 15 μm.

To accurately predict the solar radiation extinction due to aerosols, it is required to know their particle size, their complex index of refraction, and the wavelength of incident light [25]. These parameters are needed to define the optical depth (or thickness) of aerosols, which is the wavelength dependent measure of atmospheric transparency for a particular constituent. Once the optical depth is known, the transmission of aerosols in the atmosphere, $T(\lambda)$, can be calculated with Beer-Lambert-Bouguer law, or Beer's law for short, as

$$T(\lambda) = \exp\Big[- m \cdot \tau(\lambda) \Big], \tag{2.15}$$

where m is the AM and $\tau(\lambda)$ is the optical depth. Since aerosols have very location-dependent characteristics, models for the optical depth are typically created for a specific set of the environmental conditions, such as rural, urban, and maritime. Figure 2.21 shows the transmission of aerosols as defined by different models used in SMARTS, with all having the optical depth of 0.084 at 500 nm, which is the AM1.5D standard. A simpler approach is to model aerosol optical depth empirically with an Ångström power law [26]

$$\tau(\lambda) = \beta \cdot \lambda^{-\alpha}, \tag{2.16}$$

where α is the Ångström absorption exponent and β is a coefficient; both are experimentally determined. Figure 2.21 demonstrates the use of Ångström's and Beer's laws to generate

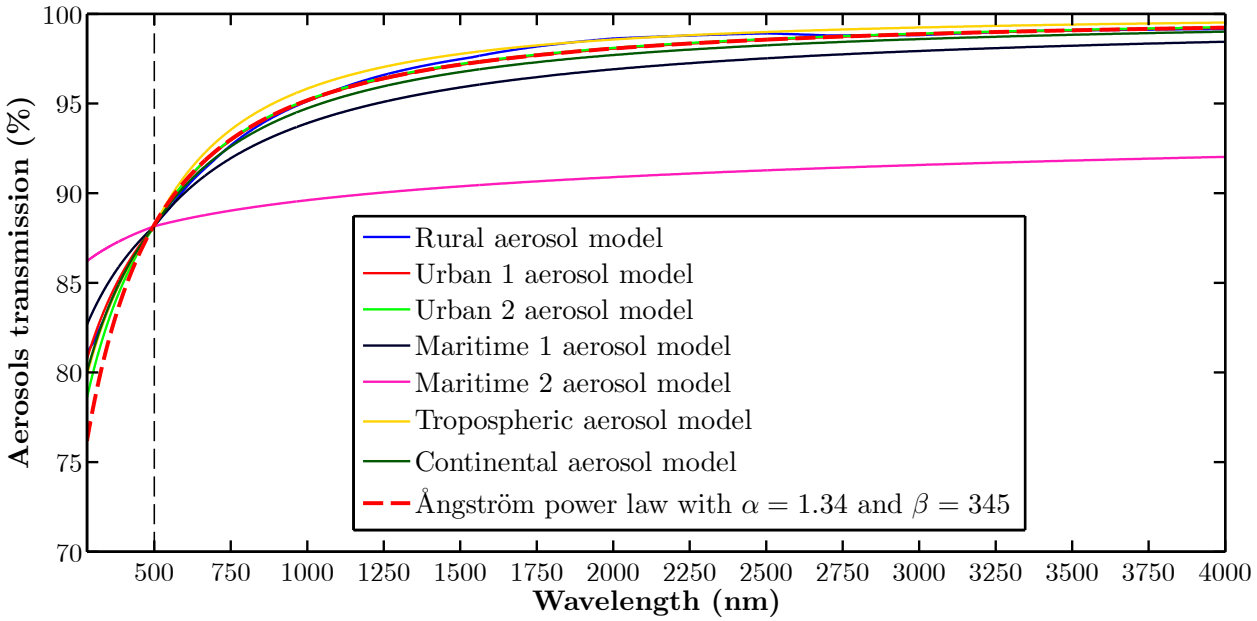

Figure 2.21: Aerosols transmission through the atmosphere represented by different models used in SMARTS, but with all having the optical depth, τ, equal to 0.084 at 500 nm and the AM equal to 1.5. Note, the rural aerosol model corresponds to the aerosol transmission profile of AM1.5D spectrum.

the transmission profile of aerosols. With adjustment of α and β parameters, every curve in Figure 2.21 can be reasonably matched without the knowledge of aerosols characteristics.

In most cases the aerosols scatter and absorb UV radiation more efficiently than IR radiation due to the average particle size of aerosols being closer to the wavelengths of the UV light. However, as the size of particles becomes significantly larger than the wavelength of the incident light, as is the case for clouds, the light scatters more uniformly in the visible range and appears white to a human eye. In other words, the transmission curves in Figure 2.21 generally shift toward the short-wave radiation with increasing aerosol particle size.

2.6.7 Rayleigh scattering

Rayleigh scattering refers to the molecular scattering of the solar radiation in the atmosphere, a phenomenon first explained by English scientist Lord Rayleigh in 1871. In this regime, the light-scattering particles are much smaller than the wavelength of the incident light. For example, with respect to the light in the visible spectral range, particles with radii less than 0.05 μm are responsible for Rayleigh scattering [25]. If the particle diameter is approximately

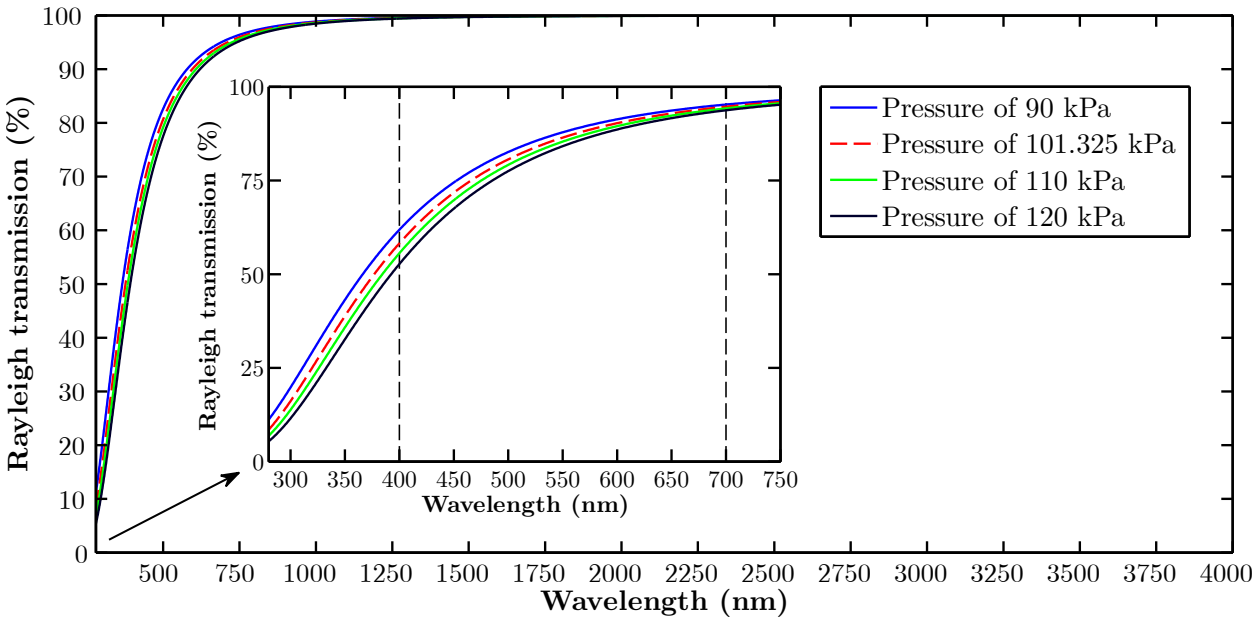

Figure 2.22: Rayleigh transmission through the atmosphere with varying ambient pressure under the AM1.5D conditions. In the visible spectral range the blue wavelengths are scattered significantly more than the red ones, which results in the sky appearing blue to a human observer. The dashed line represents the case for the AM1.5D spectrum with ambient pressure of 101.325 kPA. (SMARTS simulation).

equal to the wavelength of the incident light, the scattering regime is referred to as Mie scattering. On the other hand, if the particle size is significantly greater – geometric scattering. Both types fall under aerosols scattering, which is different from Rayleigh scattering mainly due to larger atmospheric particle size for the first phenomenon.

Similarly to aerosol scattering, Rayleigh scattering affects short-wave radiation more than long-wave radiation, although to a greater degree. Figure 2.22 shows the transmission of the solar radiation in the atmosphere due to Rayleigh scattering for different ambient pressures. For all cases in the visible spectral range the blue wavelengths are scattered significantly more than the red ones. This is the reason why the sky appears blue to a human eye. This effect is more pronounced as the ambient pressure rises, as demonstrated in Figure 2.22.

Unlike aerosol scattering, Rayleigh scattering is very predictable as the abundances of the major constituents of air (nitrogen, oxygen and argon) barely change from one location to the other if the ambient pressure is accounted for. The aforementioned molecules are the driving forces behind Rayleigh scattering.

2.6.8 Water vapour absorption

The major source of water vapour in the atmosphere is the evaporation of water from soil, rivers, lakes, and oceans. A small amount is also being produced anthropogenically from fuel combustion, however, oceans are responsible for about 85% of water vapour in the atmosphere [20]. The mixing ratio of water vapour varies significantly with a location. For example, in cold climates, such as North and South poles, water condenses as liquid or transforms into ice, and as a result its mixing ratio is almost zero. On the other hand, near the equator, where the temperature is high and the evaporation from oceans is vigorous, the water vapour content can reach up to 4% [20].

Water vapour absorption dominates solar spectrum losses in the IR range, as shown in Figure 2.23. It has several deep absorption bands around 1368, 1875, and 2760 nm, which attenuate the solar spectrum considerably even at very low water vapour path-lengths. The near IR absorption bands at 934 and 1135 nm are typically used for water vapour detection, as they transmit a moderate amount of incident irradiance through the atmosphere even under extreme conditions.

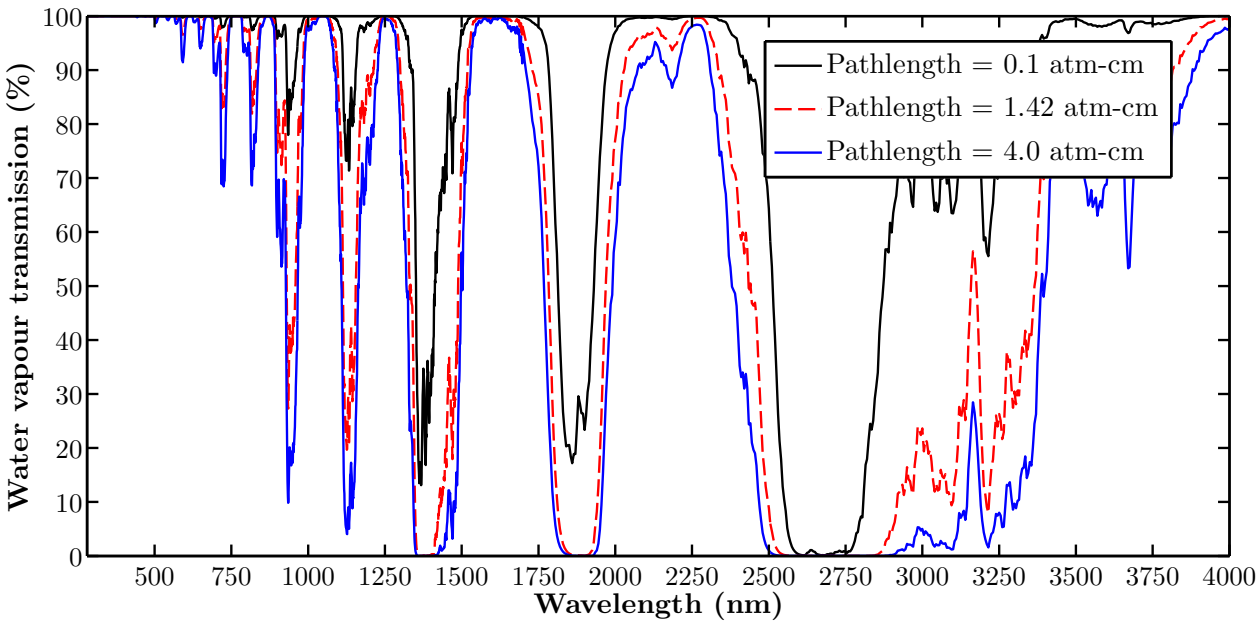

Figure 2.23: Water vapour transmission through the atmosphere with varying total column density under the AM1.5D conditions. Water vapour significantly affects the infrared portion of the solar spectrum with major absorption bands at approximately 1368, 1875, and 2670 nm. The dashed line represents the case for the AM1.5D spectrum with water vapour path-length of 1.42 cm. (SMARTS simulation).

2.7 Measuring solar resource

The analysis of PV devices requires knowledge of the incident solar irradiance, as it represents the actual input into the system. There are two main ways of performing such measurements: ground-based and satellite imaging. The satellite imaging of the atmosphere provides a good estimate of the averaged DNI and GHI for the entire planet, which would require a lot of ground-based instruments. However, the satellite imaging has a low temporal resolution and a coarse spatial accuracy. For example, NASA-modelled satellite data for a monthly average of DNI values has a root mean square (RMS) error of 22.7% [4]. On the other hand, the ground-based measurements typically have an accuracy of around ±3%.

The most common ground-based instruments for measuring DNI and GHI are pyrheliometers and pyranometers, respectively. A pyrheliometer is always mounted on a solar tracker to capture the direct plus the circumsolar irradiance as allowed by the instrument's field of view. The solar radiation is detected by a thermopile array via the Seebeck effect, which generates a voltage proportional to the temperature change between the exposed to the sun (hot) and the shaded (cold) sides of the thermopiles. The raw output voltage from a pyrheliometer is typically in the range of μV, and amplifier circuits are needed to interface the instrument with a datalogger.

A pyranometer detects solar radiation analogously to a pyrheliometer, but it is typically mounted horizontally to measure GHI. A pyranometer has a hemispherical view of the solar radiation, which is significantly greater than a pyrheliometer's field of view. In some cases a pyranometer is mounted on a south-facing tilt with respect to the horizontal in the northern hemisphere, thus measuring global tilted irradiance (GTI). GTI is useful for evaluating the performance of the fixed tilt PV panels.

Figure 2.24 shows the daily DNI and GHI profiles measured at the University of Ottawa's CPV testing facility on the summer solstice on June 21st, 2013. The DHI is calculated from these measurements by rearranging Equation 2.7. Another way to determine DHI is to install a shadowband over the horizontally mounted pyranometer. The shadowband blocks the direct sun rays and allows to measure the diffuse component of the solar radiation. Typically, on a clear-sky day the DHI value peaks at solar noon, but DHI as a percentage of GHI undertakes the opposite relationship. For example, about 13% of the GHI comes from the DHI at the solar noon in Figure 2.24. On the other hand, the GHI comprises of approximately 32% of DHI in the morning and the evening due to increased light scattering at high AMs.

A pyrheliometer's and a pyranometer's measured spectral range is usually limited by the transmission of a protective window, which is typically made out of a fused silica. This

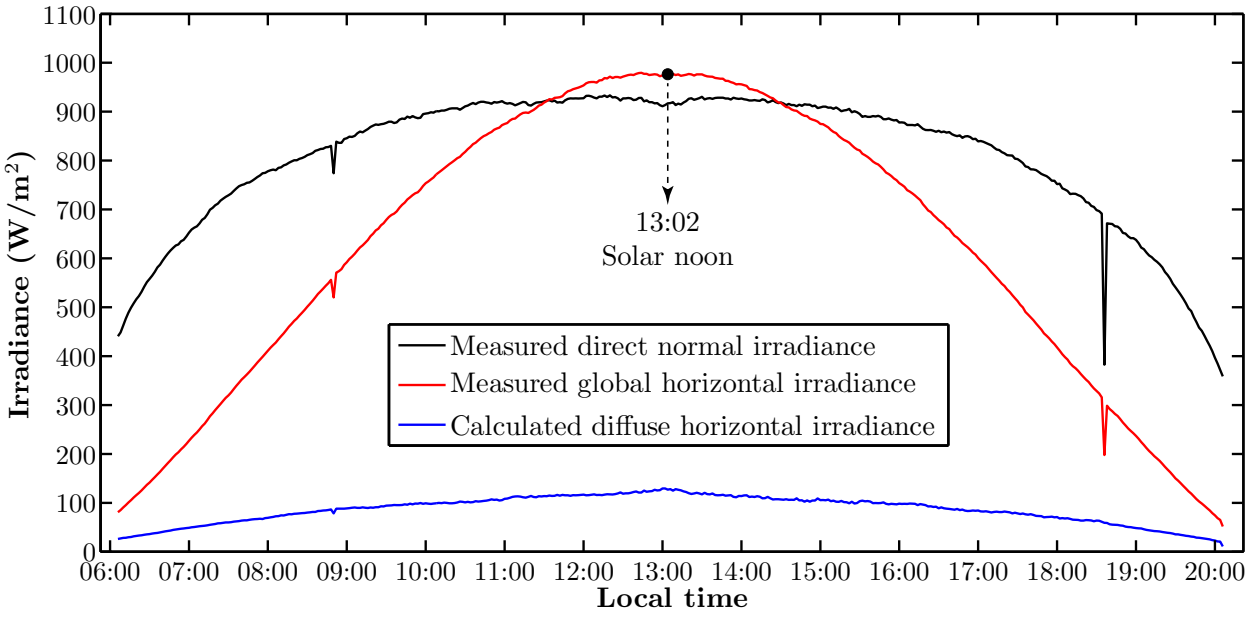

Figure 2.24: The DNI and the GHI measured at the University of Ottawa's CPV testing facility on June 21st, 2013. A few clouds are present during otherwise a perfect day. The GHI exceeds the DNI around the solar noon at 13:02 local time. Note, the daylight saving is in effect.

material has an excellent transmission in the 300–3000 nm range with only small dips in the transmission at around 2800 nm. However, a pyrheliometer and a pyranometer do not give any information about the spectral distribution of the solar irradiance. Therefore, two solar spectra may have the same absolute incident power, but their shape may differ. Figure 2.25 illustrates this case with two spectra captured at different AMs with highly distinct atmospheric conditions. Although the ozone content is about the same, the aerosol optical depth at 500 nm and total column density or path-length of water vapour are about three times greater from one spectrum to the other. Since the response of the solar cells varies for different wavelengths of light, their output power would be different for the input spectra in Figure 2.25. For example, if a Si solar panel with the responsivity shown in Figure 2.25 is used, the short circuit current density would be 23.8 mA/cm^2 versus 24.1 mA/cm^2, for difference of about 1.3%. Hence, it is often desirable to know the spectral distribution of the solar irradiance at locations of interest.

An expensive alternative to either a pyrheliometer or a pyranometer is a FSR, which can be configured to obtain either the spectral DNI or GHI. A FSR measures the solar irradiance with a resolution of a few nanometres with a photodiode or CCD array. Another instrument

capable of performing spectral measurements is a photometer or a MCFR. A MCFR measures the solar irradiance in a few narrow bands of light, primarily with a purpose of parameterizing the atmospheric effects. For example, a MCFR can be configured to determine the aerosol extinction, ozone and water vapour absorptions in the atmosphere. The next section takes a look at how this can be accomplished.

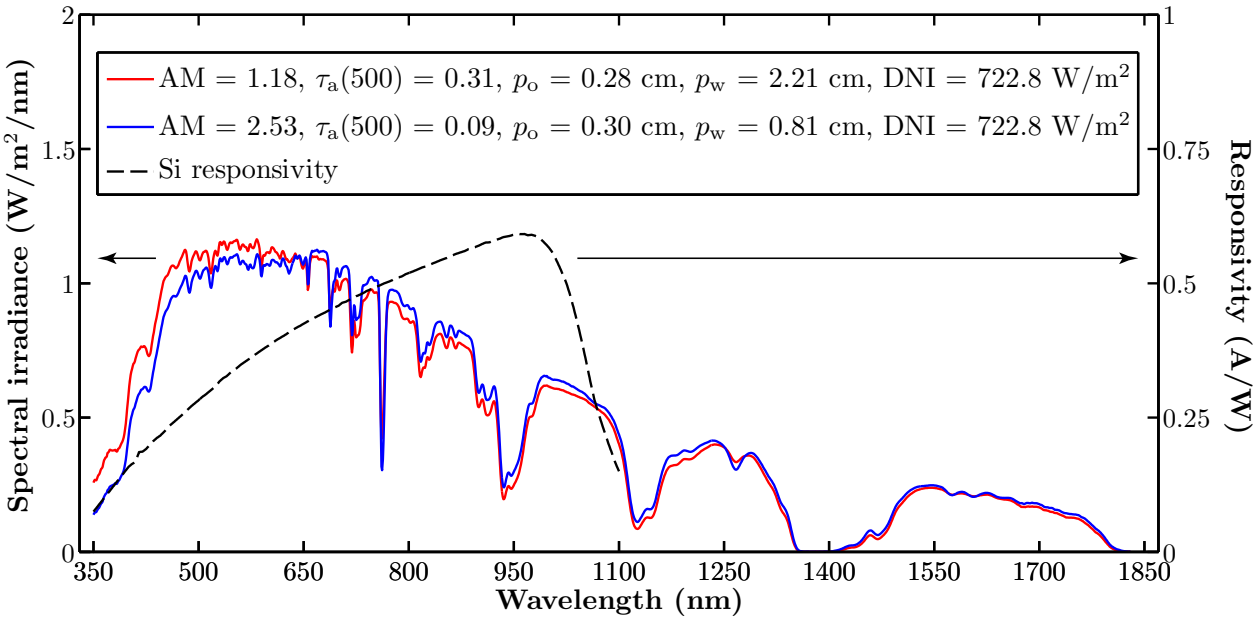

Figure 2.25: Spectra measured by the FSR at the University of Ottawa's CPV testing facility. Both curves have the same incident power but at significantly different atmospheric conditions. The aerosol optical depth and the water vapour content is about three times higher from one spectra to the other. The difference in the spectral shape results in dissimilar current density output from the solar cells. If a Si solar cell is utilized in this case, the short circuit current density would be 23.8 mA/cm^2 (red curve) versus 24.1 mA/cm^2 (blue curve) or difference of about 1.3%.

References

[1] M. Planck. "On the law of distribution of energy in the normal spectrum". In: *Annalen der Physik* 4.553 (1901), p. 1.

[2] ASTM. *E490-00a: Solar constant and zero air mass solar spectral irradiance tables.* 2006.

[3] C. A. Gueymard. "The sun's total and spectral irradiance for solar energy applications and solar radiation models". In: *Solar Energy* 76 (2004), pp. 423–453.

[4] V. Frank, M. Joseph, and S. Thomas. *Solar and infrared radiation measurements*. CRC Press, 2012.

[5] M. Gilbert. *Renewable and efficient electric power systems*. John Wiley & Sons, 2004.

[6] I. Reda and A. Andreas. *Solar position algorithm for solar radiation applications*. Tech. rep. NREL, 2008.

[7] C. A. Gueymard. "Parameterized transmittance model for direct beam and circumsolar spectral irradiance". In: *Solar Energy* 71 (2001), pp. 325–346.

[8] C. A. Gueymard. *SMARTS2: a simple model of the atmospheric radiative transfer of sunshine*. 1995.

[9] A. Berk, D. C. Robertson, and L. S. Bernstein. *MODTRAN: A Moderate Resolution Model for LOWTRAN 7*. 1989.

[10] A. Berk, G. Anderson, P. Acharya, et al. "MODTRAN4 user's manual". In: *Air Force Research Laboratory, Space Vehicles Directorate* (1999), pp. 1–5.

[11] C. A. Gueymard. *SMARTS code, version 2.9.5, user's manual*. Tech. rep. Solar Consulting Services, 2006.

[12] ASTM. *G*173-03*: Standard tables for reference solar spectral irradiances: direct normal and hemispherical on 37° tilted surface*. 2012.

[13] U. Platt and J. Stutz. *Differential optical absorption spectroscopy*. Springer, 2008.

[14] *U.S. standard atmosphere, 1976*. National oceanic and atmospheric administration, 1976.

[15] A. J. Krueger and R. A. Minzner. "A mid-latitude ozone model for the 1976 US Standard Atmosphere". In: *Journal of Geophysical Research* 81.24 (1976), pp. 4477–4481.

[16] *Air quality in Ontario, Canada*. Tech. rep. Government of Ontario, 2010.

[17] N. L. Gilbert, S. Woodhouse, D. M. Stieb, et al. "Ambient nitrogen dioxide and distance from a major highway". In: *Science of the Total Environment* 312.1 (2003), pp. 43–46.

[18] P. Foucher, A. Chédin, R. Armante, et al. "Carbon dioxide atmospheric vertical profiles retrieved from space observation using ACE-FTS solar occultation instrument". In: *Atmospheric Chemistry and Physics* 11.6 (2011), pp. 2455–2470.

[19] D. Ehhalt and L. Heidt. "Vertical profiles of CH_4 in the troposphere and stratosphere". In: *Journal of Geophysical Research* 78.24 (1973), pp. 5265–5271.

[20] M. Z. Jacobson. *Fundamentals of atmospheric modeling*. New York, USA: Cambridge University Press, 2005.

[21] J. Blunden, D. Arndt, and M. Baringer. "State of the Climate in 2010". In: *Bulletin of the American Meteorological Society* 92.6 (2011), S1–S236.

[22] R. Hosseinian and W. A. Gough. "Total Column Ozone Variability Over Toronto, Ontario, Canada". In: *The Great Lakes Geographer* Vol. 7 (2000).

[23] W. C. Hinds. *Aerosol technology: properties, behavior, and measurement of airborne particles*. John Wiley & Sons, 2012.

[24] The New Mexico Bureau of Geology & Mineral Resources. [Accessed: January 24, 2014]. URL: `http://geoinfo.nmt.edu/labs/microprobe/images/gh1.jpg`.

[25] J. H. Seinfeld and S. N. Pandis. *Atmospheric chemistry and physics: from air pollution to climate change*. John Wiley & Sons, 2012.

[26] A. Ångström. "On the atmospheric transmission of sun radiation and on dust in the air". In: *Geografiska Annaler* 11 (1929), pp. 156–166.

Chapter 3

Modelling the solar spectral resource

At present, the most accurate way to obtain solar spectra at a desired location is to perform direct outdoor measurements with a FSR. However, these measurements are rarely available due to the prohibitive cost of the instrument. An alternative approach is to use modelling tools in conjunction with available local meteorological inputs, such as atmospheric pressure, ambient temperature and humidity, to produce an approximated spectrum. The most common way to simulate spectral DNI is through the use of SMARTS, which has become the de-facto standard in the solar community [1, 2]. However, to do so accurately, SMARTS requires inputs such as the aerosol optical depth at 500 nm, water vapour and ozone total column densities, which are not typically available locally. Aerosol Robotic Network (AERONET) sites can be used to determine the aforementioned parameters if a nearby site is available (600 sites are currently in operation worldwide) [3, 4]. However, a leading option is to interpolate AERONET data for a desired location using measurements from nearby sites [5].

In chapter 3, a method of limited spectral sampling is analyzed by using a simulated MCFR to reconstruct incident local solar spectra. A MCFR is an instrument that measures solar irradiance in several narrow wavelength bands with a combination of interference filters and photodiodes. This device can perform spectral measurements at a fraction of the cost of a FSR, but additional post-processing is required to deduce the solar spectrum [6]. Therefore, it is of interest to quantify the accuracy of a MCFR for inferring spectral irradiance as the number and type of channels is varied. In this study the FSR's measurements at the University of Ottawa's CPV testing facility are fed into the model to mimic the outputs from the MCFR.

3.1 Calculation of spectral direct normal irradiance

On a clear, cloudless day the spectral DNI can be written as

$$S(\lambda) = S_0(\lambda) \cdot r^2 \cdot T_{\mathrm{a}}(\lambda) \cdot T_{\mathrm{g}}(\lambda) \cdot T_{\mathrm{n}}(\lambda) \cdot T_{\mathrm{o}}(\lambda) \cdot T_{\mathrm{R}}(\lambda) \cdot T_{\mathrm{w}}(\lambda), \tag{3.1}$$

where $S_0(\lambda)$ is the extraterrestrial irradiance (or AM0), r is the ratio of the average to actual sun to earth distance, and T_{i} is the transmittance of the atmospheric constituent, with the subscripts "a", "g", "n", "o", "R", and "w" referring to the aerosol absorption and scattering, mixed gas absorption (O_2, CO_2, and CH_4), NO_2 absorption, ozone absorption, Rayleigh scattering, and water vapour absorption, respectively. The AM0 spectrum, with an integrated irradiance value of 1366.1 W/m^2, is adapted from the most recent measurements and analysis [7].

Equation 3.1 can be expressed equivalently with Beer's law as

$$\begin{aligned} S(\lambda) = S_0(\lambda) \cdot r^2 \cdot \exp\Big[- \Big(&\tau_{\mathrm{a}}(\lambda) \cdot m_{\mathrm{a}} + \tau_{\mathrm{g}}(\lambda) \cdot m_{\mathrm{g}} + \tau_{\mathrm{n}}(\lambda) \cdot m_{\mathrm{n}} + \\ &\tau_{\mathrm{o}}(\lambda) \cdot m_{\mathrm{o}} + \tau_{\mathrm{R}}(\lambda) \cdot m_{\mathrm{R}} + \tau_{\mathrm{w}}(\lambda) \cdot m_{\mathrm{w}}^* \Big) \Big], \end{aligned} \tag{3.2}$$

where τ_i and m_i are the optical depth and the AM associated with each atmospheric component. The optical depth is a dimensionless measure of atmospheric transparency, as influenced by absorption and scattering. The AM values are functions of the zenith angle of the sun. The general expression for the AM of each component can be written from [2] as

$$m_i = \Big[\cos(Z) + \kappa_{i1} \cdot Z^{\kappa_{i2}} \cdot (\kappa_{i3} - Z)^{\kappa_{i4}} \Big]^{-1}, \tag{3.3}$$

where Z is the zenith angle (°) of the sun, calculated with NREL's SPA within uncertainty of ±0.0003° [8]. The κ_{ij} parameters are given in Table 3.1.

Table 3.1: Optical AM coefficients for Equation 3.3 from [9]

Optical AM	i	κ_{i1}	κ_{i2}	κ_{i3}	κ_{i4}
Aerosols (m_{a})	1	0.169	0.182	95.318	-1.954
Mixed gases (m_{g})	2	0.484	0.0959	96.741	-1.754
Nitrogen dioxide (m_{n})	3	1.121	1.613	111.55	-3.263
Ozone (m_{o})	4	1.065	0.638	101.8	-2.269
Rayleigh (m_{R})	5	0.484	0.0959	96.741	-1.754
Water vapour (m_{w}^*)	6	0.107	0.114	93.781	-1.920

Note: $m_{\mathrm{w}}^* = m_{\mathrm{w}}^{0.943}$

Aerosol extinction can be modelled empirically with Ångström's power law [10] as

$$\tau_{\mathrm{a}}(\lambda) = \beta_{\mathrm{y}} \cdot \lambda^{-\alpha_{\mathrm{y}}}, \tag{3.4}$$

where β_{y} and α_{y} are coefficients that are determined experimentally. Aerosol extinction is divided into y regions over the FSR's measured 350–1830 nm range, where $y+1$ is the number of aerosol dedicated channels. For example, for the MCFR with four aerosol channels, three sets of β_{y} and α_{y} coefficients are calculated and applied to the corresponding spectral region y for all wavelengths between two adjacent aerosol channels.

The optical depth due to mixed gases is caused by the cumulative effect of multiple gases that are uniformly distributed in the atmosphere. Only the constituents that significantly affect the results in the FSR's measured 350–1830 nm range are selected in the simulations. Consequently, the mixed gases optical depth can be expressed as

$$\tau_{\mathrm{g}}(\lambda) = p_{\mathrm{CH_4}} \cdot A_{\mathrm{CH_4}}(\lambda) + p_{\mathrm{CO_2}} \cdot A_{\mathrm{CO_2}}(\lambda) + p_{\mathrm{O_2}} \cdot A_{\mathrm{O_2}}(\lambda), \tag{3.5}$$

where p_i is the path-length of the constituent gas (in atm-cm) and $A_i(\lambda)$ is its wavelength-dependent absorption coefficient (in cm^{-1}). The path-length of a gas with a uniform mixing ratio profile is affected by changes in temperature and pressure in the atmosphere. The general expression for it can be written as

$$p_i = \chi_{\mathrm{V}} \cdot P_{\mathrm{r}}^{\gamma} \cdot T_{\mathrm{r}}^{\varphi} \cdot H, \tag{3.6}$$

where is χ_{V} the volume mixing ratio of a gas (in ppmv), P_{r} and T_{r} are the ratios of actual to reference pressure and temperature, respectively, γ, φ are pressure and temperature correction coefficients, respectively, and H is the path-length of the entire atmosphere. The latter is equal to 7.9895×10^5 cm for the U.S. 1976 standard atmosphere and is calculated from

$$H = \frac{N_{\mathrm{A}}}{R \cdot N_{\mathrm{L}}} \cdot \int_0^{\infty} \frac{P(z)}{T(z)} \cdot dz, \tag{3.7}$$

where $P(z)$ and $T(z)$ are the pressure and the temperature profiles of the atmosphere, respectively. Table 3.2 presents the assumed volume mixing ratios of mixed gases along with pressure and temperature correction coefficients.

Table 3.2: Mixed gases volume mixing ratios [11] with pressure and temperature correction coefficients [9].

Mixed gas	χ_{V} (ppmv)	γ	φ
Methane (CH_4)	1.8	1.125	0.0473
Carbon dioxide (CO_2)	375	1	0
Oxygen (O_2)	209500	1	0

The ozone optical depth can be expressed as

$$\tau_{\mathrm{o}}(\lambda) = p_{\mathrm{o}} \cdot A_{\mathrm{o}}(\lambda) \cdot C_{\mathrm{o}}(\lambda, T), \tag{3.8}$$

where p_{o} is the experimentally determined ozone path-length (in atm-cm), $A_{\mathrm{o}}(\lambda)$ is the absorption coefficient in (cm^{-1}), and $C_{\mathrm{o}}(\lambda, T)$ is the unitless ozone temperature correction function.

The nitrogen dioxide (NO_2) optical depth, $\tau_{\mathrm{n}}(\lambda)$, is a highly variable atmospheric quantity, deriving from both natural and anthropogenic sources. Its expression is identical to Equation 3.8 utilizing the absorption coefficient, $A_{\mathrm{n}}(\lambda)$, and the temperature correction function, $C_{\mathrm{n}}(\lambda, T)$. A path-length of $p_{\mathrm{n}} = 0.00118$ atm-cm is used, which is the average concentration of NO_2 in Montreal, Canada in 2005.

Rayleigh scattering is a well-understood phenomenon [12, 13]. The least-squares fit from [9] is used to determine the optical depth as

$$\tau_{\mathrm{R}}(\lambda) = \frac{P_{\mathrm{r}}}{\omega_1 \cdot \lambda^4 + \omega_2 \cdot \lambda^2 + \omega_3 + \omega_4 \cdot \lambda^{-2}}, \tag{3.9}$$

where P_{r} is the ratio of site to sea level ambient pressure, $\omega_1 = 117.341\ \mathrm{nm}^{-4}$, $\omega_2 = 1.511\ \mathrm{nm}^{-2}$, $\omega_3 = 0.0175$, and $\omega_4 = 8.774\ \mathrm{nm}^2$.

The expression for precipitable water vapour from [9] is formulated as

$$\tau_{\mathrm{w}}(\lambda) = p_{\mathrm{w}}^{0.943} \cdot \varepsilon_1(\lambda) \cdot \varepsilon_2(\lambda) \cdot A_{\mathrm{w}}(\lambda), \tag{3.10}$$

where $A_{\mathrm{w}}(\lambda)$ is its wavelength-dependent absorption coefficient (cm^{-1}), $\varepsilon_1(\lambda, P)$ is the pressure scaling factor that accounts for water vapour's inhomogeneity in the atmosphere, $\varepsilon_1(\lambda, p_{\mathrm{w}})$ is the correction factor that improves parameterization away from the band centre under fluctuating water vapour conditions, and p_{w} is the experimentally determined water vapour path-length (in atm-cm). The absorption coefficients and the temperature, pressure correction functions for all atmospheric constituents are used with minor modifications from SMARTS unless otherwise indicated [1, 2].

3.2 Simulation of a multi-channel filter radiometer

Based on the number of desired MCFR's channels and the filter characteristics, the corresponding Gaussian filter's transmission profiles can be generated and applied to the FSR's solar spectrum. This is the basic procedure of simulating the MFCR, which is exemplified in Figure 3.1 with six channels. The spectral current density of each channel is determined by applying the responsivity of the appropriate photodiode, which is typically made out of

Si or germanium (Ge), depending on the spectral location of the channel, as demonstrated in Figure 3.2. The integration of the spectral current density over all wavelengths gives the current density for each channel in units of A/m^2. The "measured" photodiode current, $I_{x,\text{measured}}$, for each channel x can be expressed as

$$I_{x,\text{measured}} = A \cdot \int_{\lambda_1}^{\lambda_2} S(\lambda) \cdot F_x(\lambda) \cdot R(\lambda) \cdot d\lambda, \tag{3.11}$$

where A is the active area of the photodiode, $S(\lambda)$ is the measured spectrum, $F_x(\lambda)$ is the filter transmission of channel x, $R(\lambda)$ is the responsivity of the photodiode, and λ_1, λ_2 is the wavelength range of the channel. Since the full widths at half maxima (FWHM) of the MCFR's filters are narrow, typically 1-10 nm, the integration is not performed for the entire spectral range [6]. It is assumed that the filters have no out-of-band transmission. Hence, the inputs into the model are x values representing the current "measured" from each channel.

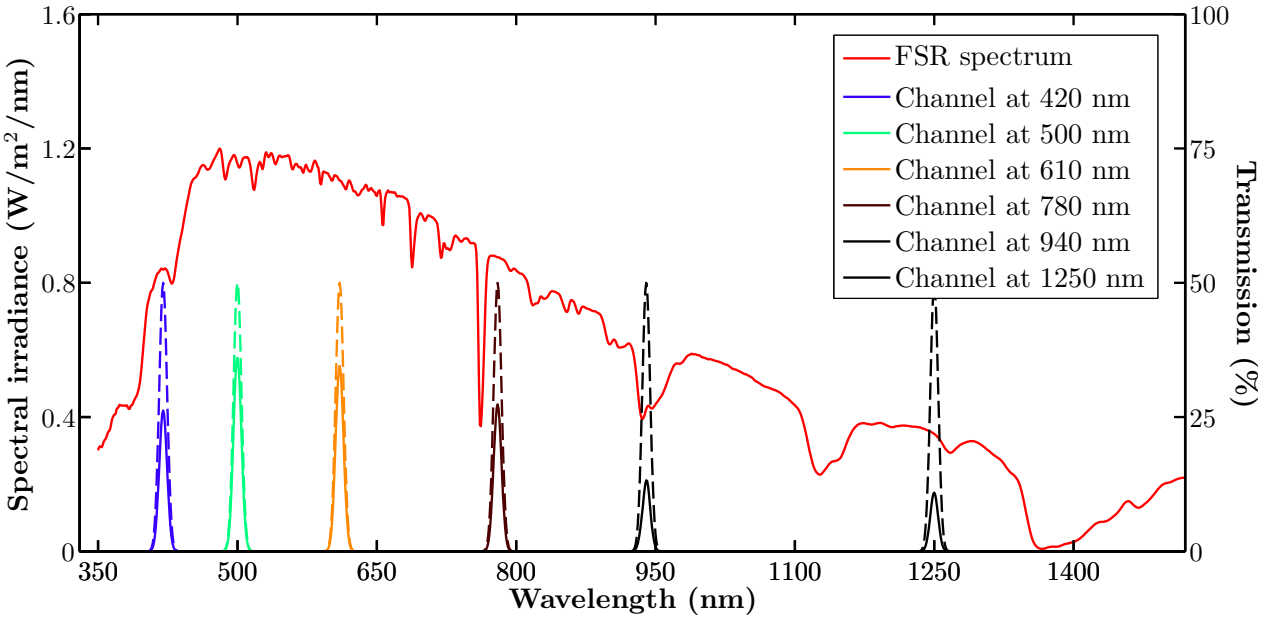

Figure 3.1: The simulation of the MCFR from the solar spectrum measured by the FSR. Dashed lines are Gaussian filter transmission profiles for each channel of the MCFR. The corresponding solid lines are the product of the filter transmission and the solar spectrum from the FSR (red line).

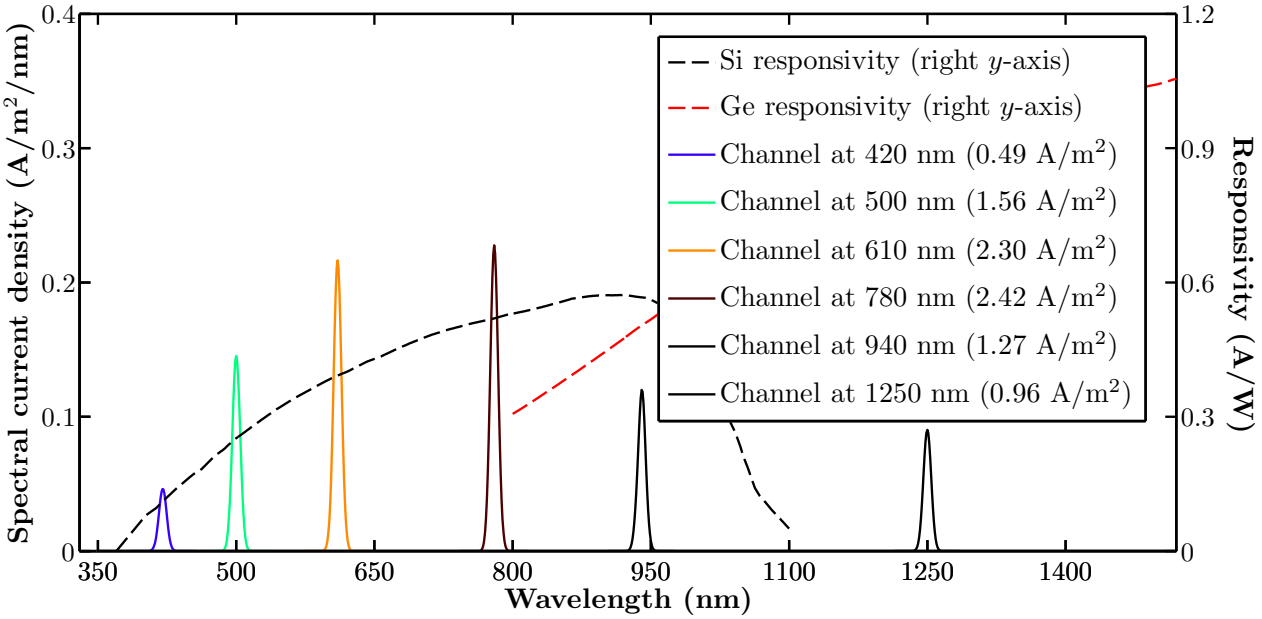

Figure 3.2: The application of the photodiode responsivity to each channel of the MCFR from Figure 3.1. In this case the channel at 420 nm has the lowest current density of 0.49 A/m^2, while the channel at 780 nm has the highest current density of 2.42 A/m^2.

3.3 Channel selection for spectrum parameterization

Aerosol extinction and Rayleigh scattering affect all photons of the solar spectrum in the 350–1830 nm range, but ozone and water vapour absorptions are only significant in discrete spectral regions. Figure 3.3 shows the transmission of the DNI beam without the effects of aerosol extinction and Rayleigh scattering. The total column densities of ozone and water vapour are varied from one extreme to the other with ozone path-lengths increasing from 0.1 to 0.6 cm and the water vapour path-length from 0.1 to 4.0 cm. This exercise reveals six areas for possible placement of aerosol channels in the 350–1830 nm range. In these regions there are practically no effects from varying concentrations of ozone and water vapour, as it is emphasized in Figure 3.4 where the difference in the DNI beam transmissions for extreme cases is demonstrated.

The summary of the preferred spectral regions for aerosol extinction detection is shown in Table 3.3. The centre wavelength of the channel can lie anywhere within the specified regions. Each area houses one aerosol channel, except the area ①, which uses two channels because the solar spectrum changes rapidly from 350 to 510 nm.

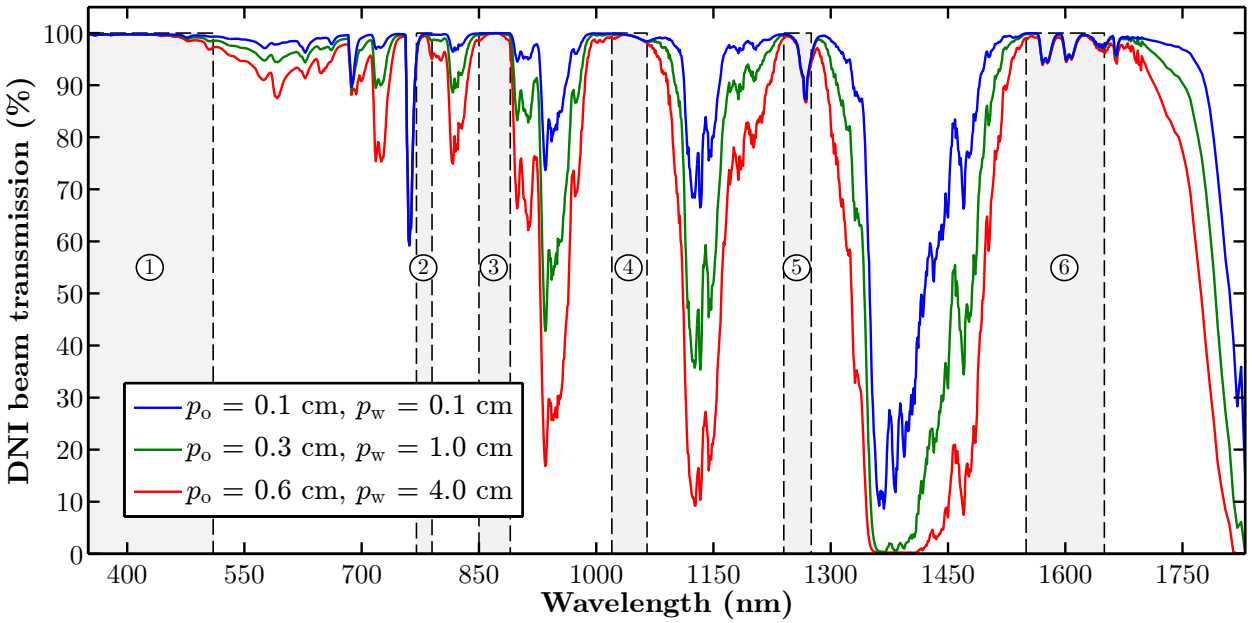

Figure 3.3: Beam transmission of the spectral DNI through the atmosphere without the aerosol extinction and Rayleigh scattering. The path-lengths of ozone and water vapour, p_o and p_w, respectively, are varied from one extreme to the other to reveal six suitable spectral areas for the aerosols detection.

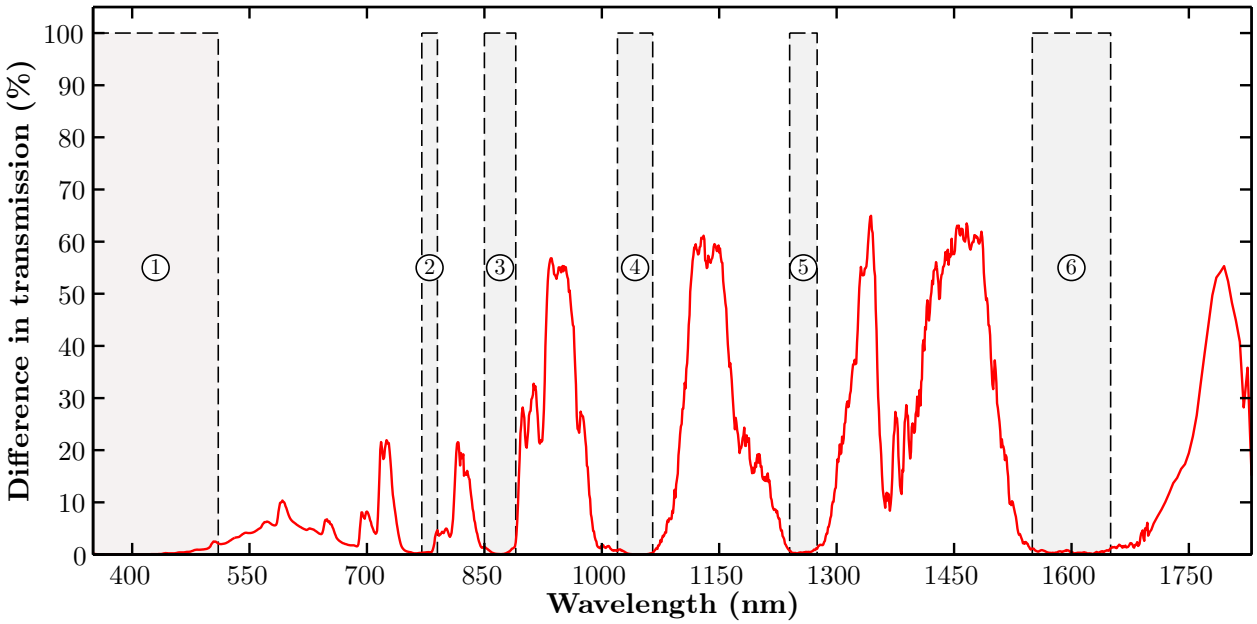

Figure 3.4: Difference in the beam transmissions of the spectral DNI between the extreme cases from Figure 3.3. A more vivid illustration of where the solar spectrum is not significantly affected by mixed gases, trace gases, water vapour, and ozone absorptions.

Ozone absorption of the solar spectrum is very weak across the 350–1830 nm range, even under the most extreme conditions, as shown in Figure 3.5. The region from 500–700 nm, also known as the Chappuis band, where the maximum ozone absorption occurs, is used to study the most suitable area for ozone channel placement. This point roughly corresponds to 602 nm. However, the inset plot in Figure 3.6 reveals moderate water vapour absorption in the 580–605 nm range. Therefore, the ozone channel is placed at 610 nm, which does not overlap with water vapour absorption but is still close to the peak ozone absorption.

The water vapour channel is also placed where its maximum absorption occurs. Suitable areas for the water vapour channel in the 350–1830 nm range are marked in Figure 3.6. Out of the three spectral bands, area ② is the most ideal, as it is more sensitive to water vapour absorption than area ①, yet it contains more incident power than area ③.

Finally, Table 3.4 summarizes the MCFR's channels and corresponding filter characteristics that are used in the simulation. All filters have FWHM of 10 nm and the maximum transmission at the centre wavelength of 50%.

Table 3.3: The MCFR's aerosol channels location.

Channel centre (nm)	Area	Spectral range (nm)
420, 500	①	350–510
780	②	770–790
870	③	850–890
1050	④	1020–1065
1250	⑤	1240–1275
1650	⑥	1550–1650

Table 3.4: The MCFR's channels and filter characteristics.

Channel centre (nm)	Parameter	FWHM (nm)
420, 500, 780, 870, 1050, 1250, 1650	Aerosols	10
610	Ozone	10
940	Water vapour	10

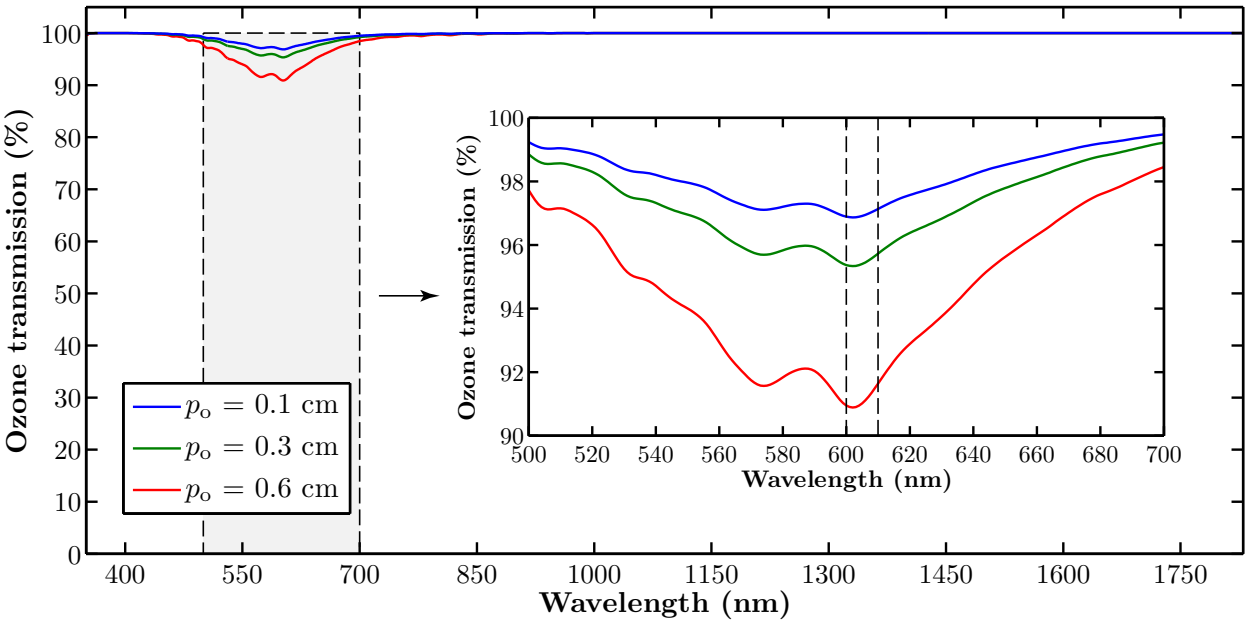

Figure 3.5: Ozone transmission with varying total column densities. The path-lengths of 0.1 cm and 0.6 cm are the extreme cases and rarely occur. The inset plot shows the peak ozone absorption in the visible range is at approximately 602 nm.

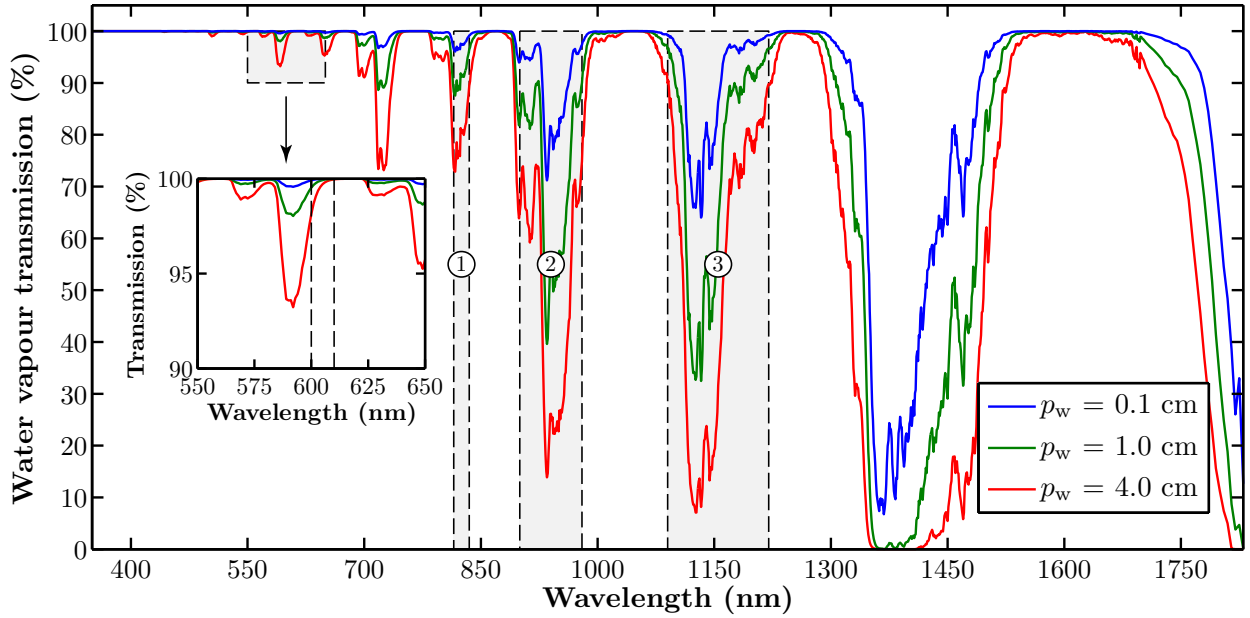

Figure 3.6: Water vapour transmission with varying total column densities. The inset plot shows the moderate absorption of water vapour in the vicinity of 600 nm, which corresponds to the peak ozone absorption in the visible range, hence the ozone channel at 610 nm is a better alternative. In addition, the area ② is the best choice for the water vapour channel.

3.4 Solar spectrum parameterization

The solar spectrum in Equation 3.1 is obtained by determining the unknowns $T_{\mathrm{a}}(\lambda)$, $T_{\mathrm{o}}(\lambda)$, and $T_{\mathrm{w}}(\lambda)$. To derive these quantities, the MCFR channels must be selected to isolate the effect of one atmospheric constituent at a time. This is accomplished by placing appropriate channels in the regions where only one unknown atmospheric parameter dominates. Figure 3.3 reveals the areas that are unaffected by the ozone and water vapour absorption. The channels in these regions are used to determine the aerosol extinction. For example, channels centred at 500 and 780 nm (areas ① and ②, respectively, in Figure 3.3) can be used to deduce aerosol extinction for every wavelength in that range. Since the FWHM of each filter is 10 nm, the filter transmission does not extend far from the centre wavelength. Hence, ozone and water vapour absorption are neglected within the aerosol channels given in Table 3.4. The expression for the spectral irradiance of the aerosol channel centred at λ_{c} resembles Equation 3.1 except that $T_{\mathrm{o}}(\lambda)$ and $T_{\mathrm{w}}(\lambda)$ are set to unity for $\lambda_1 \leq \lambda \leq \lambda_2$, where $\lambda_1 = \lambda_{\mathrm{c}} - 25$ nm and $\lambda_2 = \lambda_{\mathrm{c}} + 25$ nm. Transmission outside the given range is assumed to be negligible. Therefore, the simulated current of the photodiode for the aerosol channel x is expressed as

$$I_{x,\mathrm{simulated}} = A \cdot r^2 \cdot \int_{\lambda_1}^{\lambda_2} T_{\mathrm{a}}(\lambda) \cdot C_x(\lambda) \cdot d\lambda, \tag{3.12}$$

where $C_x(\lambda) = S_0(\lambda) \cdot T_{\mathrm{g}}(\lambda) \cdot T_{\mathrm{n}}(\lambda) \cdot T_{\mathrm{R}}(\lambda) \cdot F_x(\lambda) \cdot R(\lambda)$. The uniform trapezoidal rule is used to approximate the result of the integration in Equation 3.12. The only outstanding unknown is $T_{\mathrm{a}}(\lambda)$, which can be expressed through the combination of Beer's and Ångström's power laws as

$$T_{\mathrm{a}}(\lambda) = \exp\Big[- \beta_{\mathrm{y}} \cdot \lambda^{-\alpha_{\mathrm{y}}} \cdot m_{\mathrm{a}} \Big]. \tag{3.13}$$

For a given aerosol extinction region y, the values of α_{y} and β_{y} are optimized such that simulated current of the photodiode from Equation 3.12 agrees with measured current from Equation 3.11. In other words, the total residual difference between the simulated and the measured current values is minimized for two channels that define the aerosol region. A 1-D Golden section search algorithm is used to find the values of α_{y} that produces the smallest residual error for 40 pre-defined values of β_{y}. Finally, the optimal values of α_{y} and β_{y} are passed to a 2-D simplex algorithm to further refine these parameters. This optimization routine is performed for each aerosol region y in order to determine the aerosol transmission, $T_{\mathrm{a}}(\lambda)$. Calculation of the aerosol transmission is a crucial step in deriving the ozone and the water vapour total column densities.

The spectral irradiance for ozone and water vapour channels is very similar to Equation 3.1, but $T_{\mathrm{w}}(\lambda)$ and $T_{\mathrm{o}}(\lambda)$ are set to unity, respectively. The simulated current of the

photodiodes for these channels resembles Equation 3.12 with the addition of the appropriate $T_{\mathrm{o}}(\lambda)$ or $T_{\mathrm{w}}(\lambda)$ term. The unknown ozone and water vapour transmittances are expressed through Beer's law in a similar manner to Equation 3.13 with suitable formulations for the optical depth and AM. Both the ozone and water vapour total column abundances, p_{o} and p_{w}, are found with a 1-D Golden section search algorithm that minimizes the residual difference between the simulated and measured current values. Once the parameterization is complete, the simulated spectral irradiance $S(\lambda)$ from Equation 3.1 is computed and compared with the measured spectral irradiance from the FSR.

3.5 Model validation

An extensive analysis of 57,876 measured spectra from the University of Ottawa's CPV testing facility is performed to validate the developed algorithm for solar spectrum reconstruction with the simulated MCFR. All spectra contain at least 200 $\mathrm{W/m^2}$ of incident DNI in the FSR's measured 350–1830 nm range. A large number of spectra permits testing of the algorithm under a wide range of the atmospheric inputs to ensure it is applicable to other locations with different climatic conditions. For example, Figures 3.7 and 3.8 show a six channel MCFR's solar spectrum reconstruction that consists of four aerosol channels (420, 500, 780, and 1050 nm), the ozone channel (610 nm), and the water vapour channel (940 nm) under clear and hazy conditions in Ottawa. There is a high contrast in the aerosol and water vapour content between both cases, yet the spectral reconstruction in each instance is accurate. This observation is emphasized by the inset plots in both figures that show in detail the effective simulation of water vapour absorption. Furthermore, in both cases, the total incident power between the measured and simulated spectra are in excellent agreement. The total power difference is -6.1 $\mathrm{W/m^2}$ (or -1.24 %) and -4.3 $\mathrm{W/m^2}$ (or -0.5 %) for clear and hazy conditions, respectively. Smoothing by central moving average is performed on the simulated spectrum to match its resolution with the measured spectrum.

Since it is not practical to analyze every spectrum in such detail manually, yearly simulations are performed. The RMS error and mean difference of the analyzed data sets for 2012 and 2013 with respect to the original measured spectra are calculated, as shown in Figures 3.9 through 3.12. This technique allows comparing different channel configurations with ease. The lowest RMS error and mean difference typically occur in areas where the aerosol, ozone, or water vapour channels are located. The mean difference is calculated based on a weighted technique to avoid large differences between small irradiance values. The largest discrepancies occur at the very sharp and narrow oxygen absorption bands around 687 nm and 761 nm due to the FSR's limited spectral resolution of several nanometres.

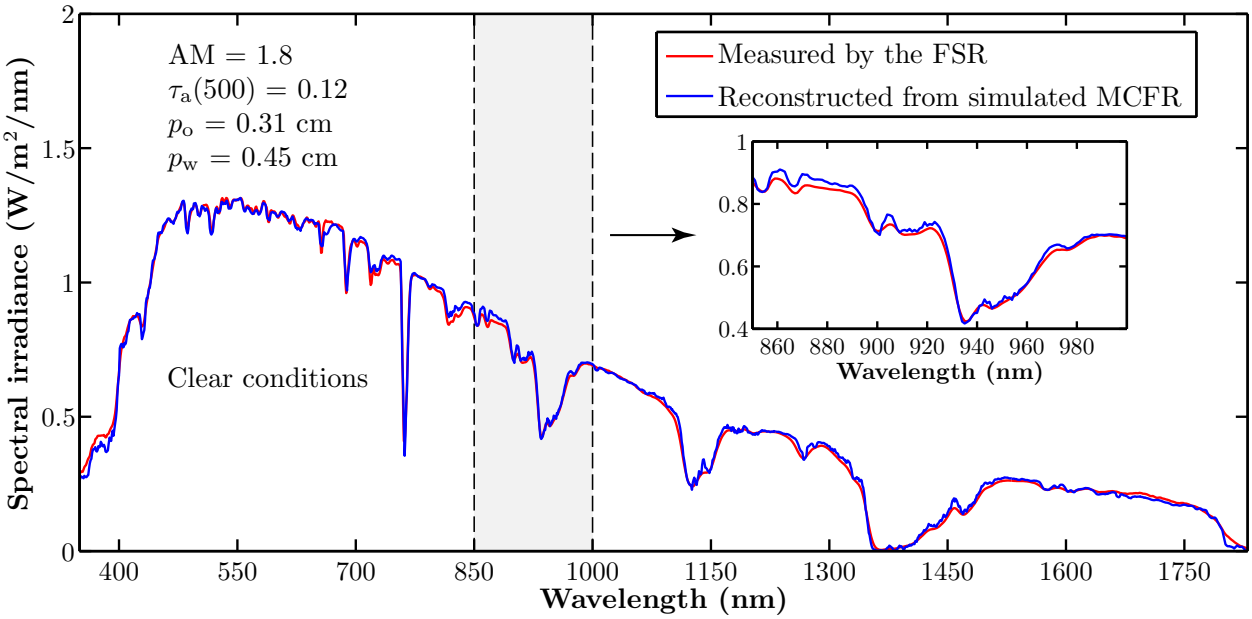

Figure 3.7: Comparison of the measured solar spectrum by the FSR and the simulated spectrum with a six channel MCFR under clear conditions in Ottawa. The MCFR consists of four aerosol channels (420, 500, 780, and 1050 nm), one ozone channel (610 nm) and one water vapour channel (940 nm).

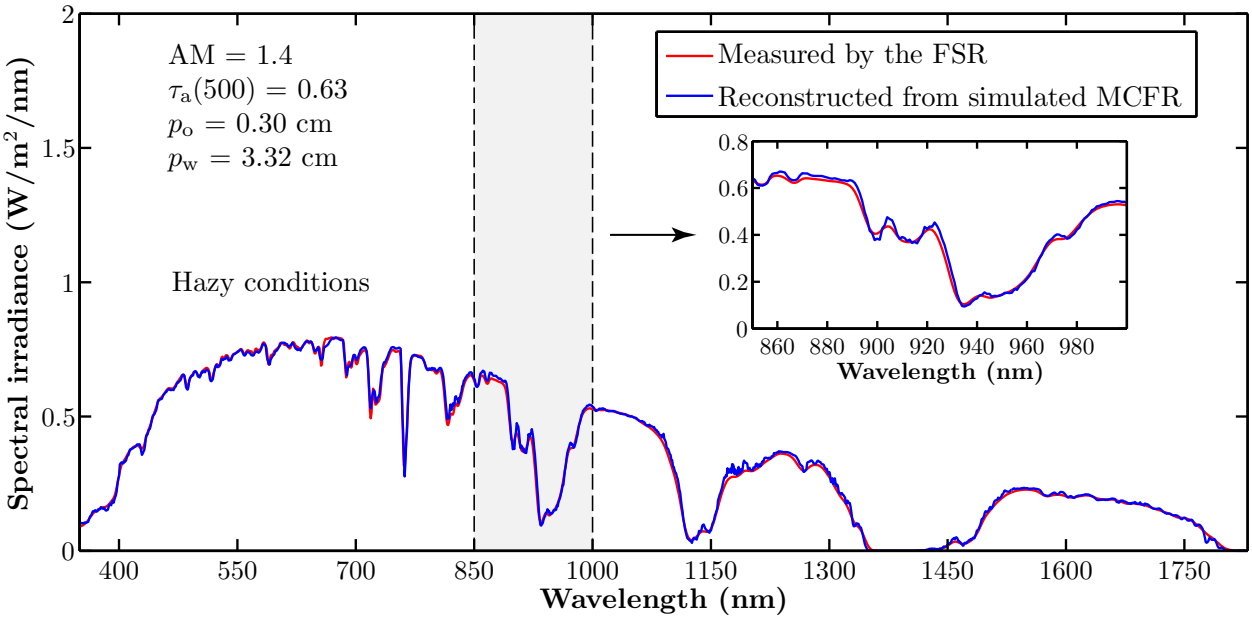

Figure 3.8: Comparison of the measured solar spectrum by the FSR and the simulated spectrum with a six channel MCFR under hazy conditions in Ottawa. The MCFR consists of four aerosol channels (420, 500, 780, and 1050 nm), one ozone channel (610 nm) and one water vapour channel (940 nm).

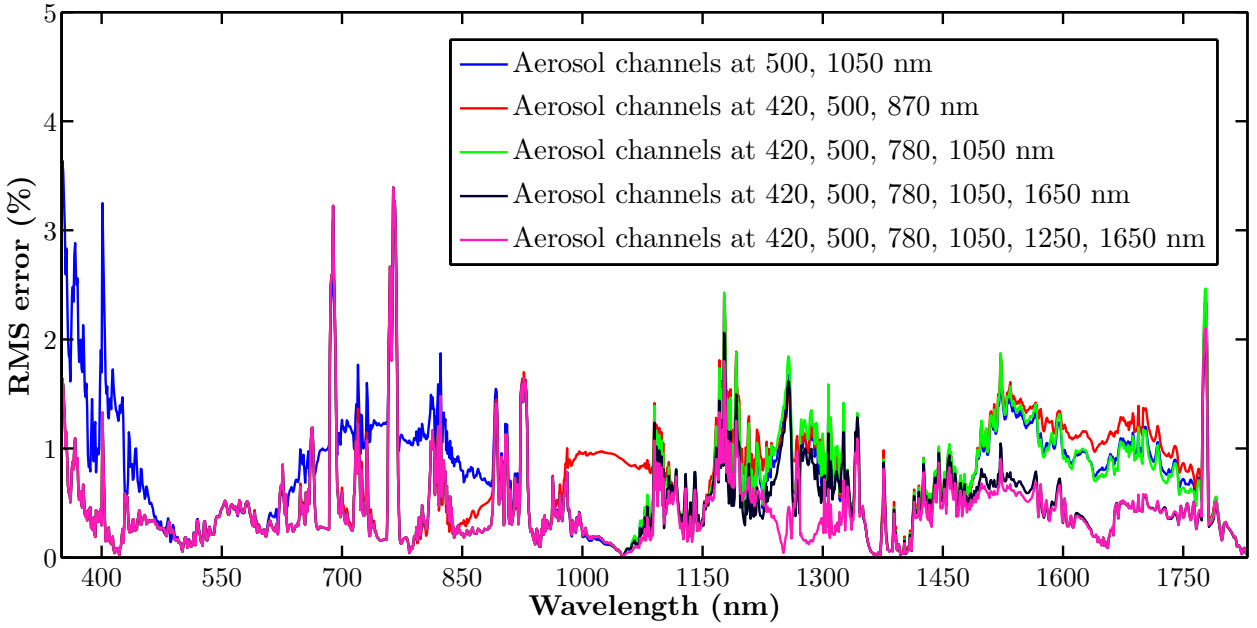

Figure 3.9: The RMS error between the measured spectra by the FSR and the simulated spectra with a two to six aerosol channel MCFR. The analysis is performed for 26,768 measured spectra in 2012. Every configuration contains the ozone channel at 610 nm and the water vapour channel at 940 nm.

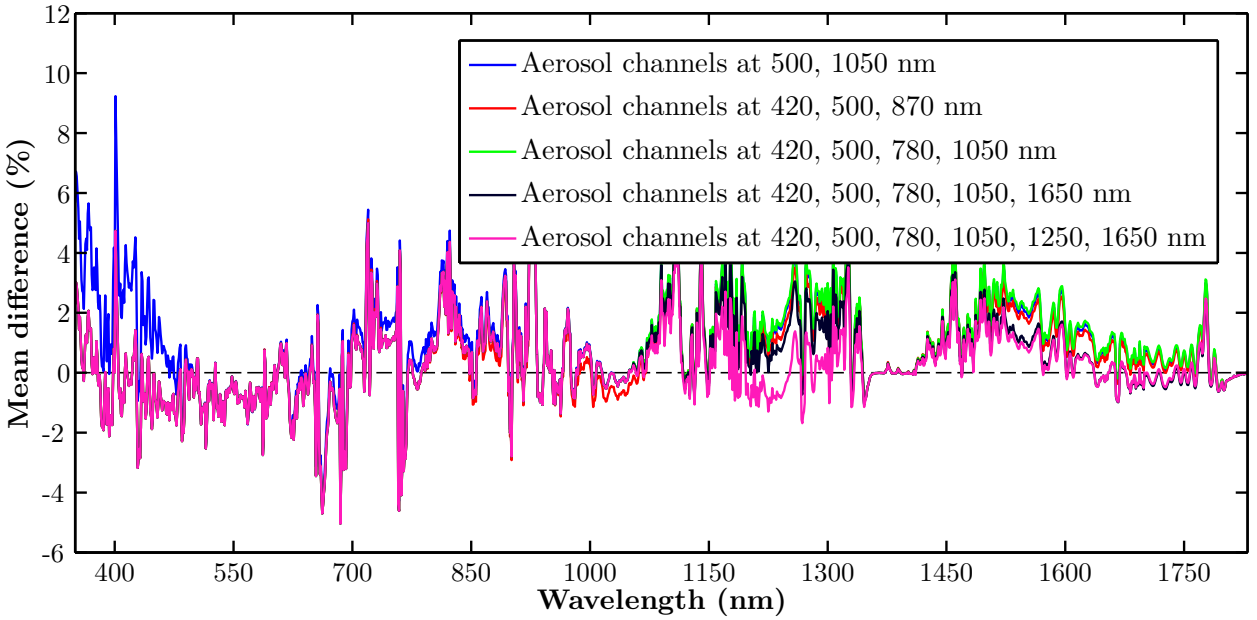

Figure 3.10: Mean difference between the measured spectra by the FSR and the simulated spectra with a two to six aerosol channel MCFR. The analysis is performed for 26,768 measured spectra in 2012. Every configuration contains the ozone channel at 610 nm and the water vapour channel at 940 nm.

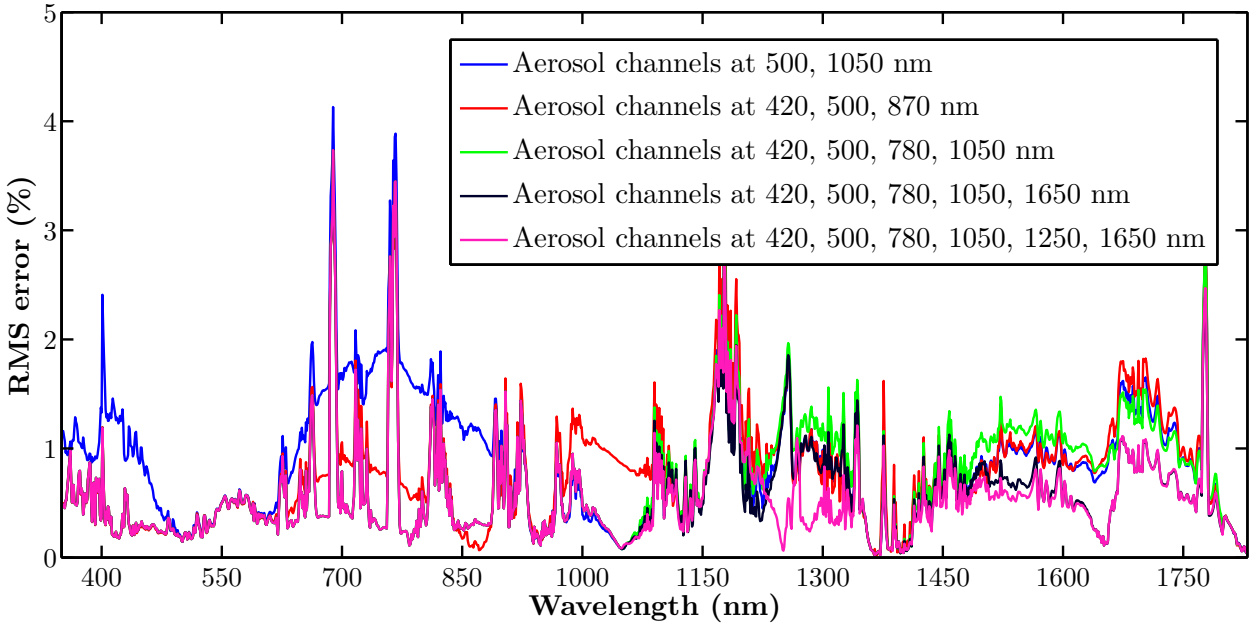

Figure 3.11: RMS error between the measured spectra by the FSR and the simulated spectra with a two to six aerosol channel MCFR. The analysis is performed for 31,108 measured spectra in 2013. Every configuration contains the ozone channel at 610 nm and the water vapour channel at 940 nm.

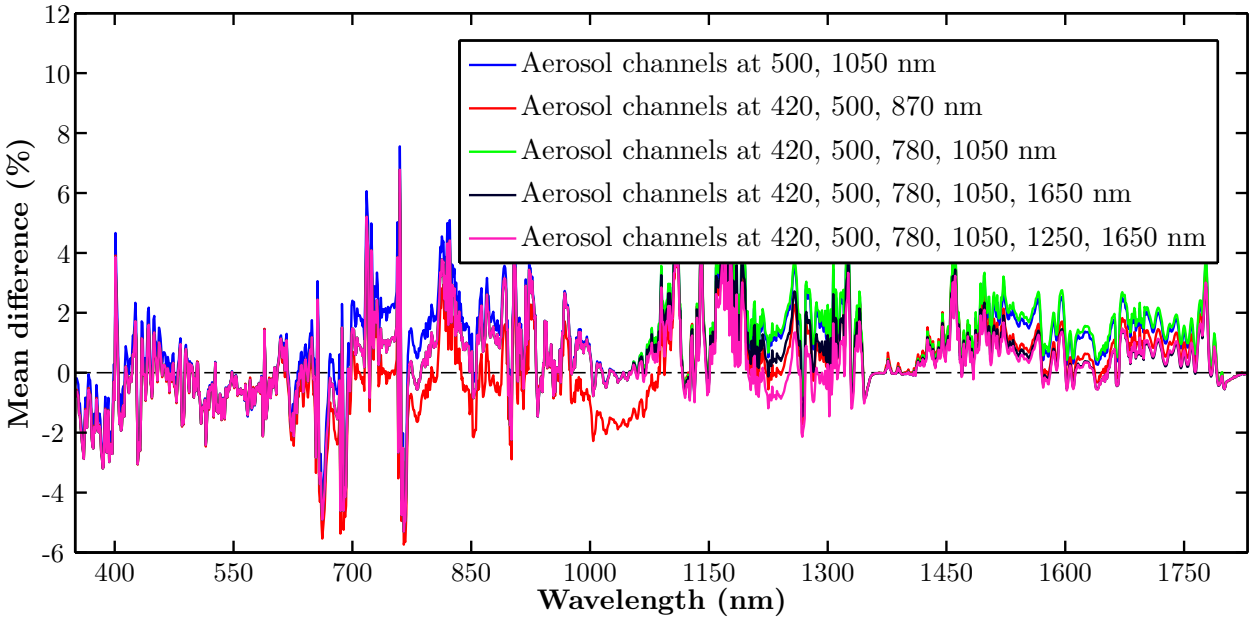

Figure 3.12: Mean difference between the measured spectra by the FSR and the simulated spectra with a two to six aerosol channel MCFR. The analysis is performed for 31,108 measured spectra in 2013. Every configuration contains the ozone channel at 610 nm and the water vapour channel at 940 nm.

Table 3.5 summarizes the results of Figures 3.9 through 3.12 by highlighting the best aerosol channel combinations. For all of these cases, the ozone and the water vapour channels at 610 nm and 940 nm, respectively, are included. To compare different aerosol channel combinations, the areas under the RMS error curves are normalized to the highest area or the worst performing configuration. The inverse of the resultant values is calculated to ensure that the worst performing channel combination has the lowest value. Table 3.5 reveals that the Ångström power law is not sufficient to estimate aerosol extinction across the entire measured spectral range. Application of the power law piece-wise, with different α_y and β_y parameters for each spectral range, gives more accurate fits to the measured data.

Although six aerosol channels give a very good spectral reconstruction accuracy, it is not generally desirable to have channels centred at 1250 and 1650 nm. These infrared channels need expensive Ge or InGaAs detectors, which have bandgaps low enough to capture photons at those wavelengths. On the other hand, Si-based detectors are relatively cheap and ubiquitous. Therefore, it is recommended to either use a three aerosol channel configuration of 420, 500, and 870 nm or a four channel configuration of 420, 500, 780, and 1050 nm. In both cases the standard deviation or the RMS error for the 2012 data set in Ottawa is under 1.5% over 96% of the 350–1830 nm range, while for the 2013 dataset it is under 1.5% for over 93% of the 350–1830 nm range. This discrepancy can be partially explained due to the first dataset containing 4,340 spectra less than the latter dataset, which may have introduced more spectral variability and as a result a lower reconstruction accuracy.

Table 3.5: The relative performance of the best aerosol channel combinations.

Aerosol channels	Best combination	Relative performance*	
		2012	2013
2	500, 1050 nm	1	1
3	420, 500, 870 nm	1.098	1.129
4	420, 500, 780, 1050 nm	1.271	1.242
5	420, 500, 780, 1050, 1650 nm	1.624	1.512
6	420, 500, 780, 1050, 1250, 1650 nm	1.796	1.629

Note: Relative performance is defined as the inverse of the normalized area of the RMS error curve.

References

[1] C. A. Gueymard. *SMARTS2: a simple model of the atmospheric radiative transfer of sunshine*. 1995.

[2] C. A. Gueymard. "Parameterized transmittance model for direct beam and circumsolar spectral irradiance". In: *Solar Energy* 71 (2001), pp. 325–346.

[3] B. Holben, T. Eck, I. Slutsker, et al. "AERONET - A federated instrument network and data archive for aerosol characterization". In: *Remote Sensing of Environment* 66.1 (1998), pp. 1–16.

[4] B. Holben, D. Tanre, A. Smirnov, et al. "An emerging ground-based aerosol climatology: Aerosol optical depth from AERONET". In: *Journal of Geophysical Research: Atmospheres* 106.D11 (2001), pp. 12067–12097.

[5] N. Chan, T. Young, H. Brindley, et al. "Validation of energy prediction method for a concentrator photovoltaic module in Toyohashi Japan". In: *Progress in Photovoltaics: Research and Applications* (2012).

[6] G. Seckmeyer, A. Bais, G. Bernhard, et al. *Instruments to measure solar ultraviolet radiation, Part 3: Multi-channel filter instruments*. Tech. rep. World Meteorological Organization Global Atmosphere Watch, 2010.

[7] C. A. Gueymard. "The sun's total and spectral irradiance for solar energy applications and solar radiation models". In: *Solar Energy* 76 (2004), pp. 423–453.

[8] I. Reda and A. Andreas. "Solar position algorithm for solar radiation applications". In: *Solar energy* 76.5 (2004), pp. 577–589.

[9] C. A. Gueymard. *SMARTS code, version 2.9.5, user's manual*. Tech. rep. Solar Consulting Services, 2006.

[10] A. Ångström. "On the atmospheric transmission of sun radiation and on dust in the air". In: *Geografiska Annaler* 11 (1929), pp. 156–166.

[11] M. Z. Jacobson. *Fundamentals of atmospheric modeling*. New York, USA: Cambridge University Press, 2005.

[12] A. Bucholtz. "Rayleigh-scattering calculations for the terrestrial atmosphere". In: *Applied Optics* 34.15 (1995), pp. 2765–2773.

[13] B. A. Bodhaine, N. B. Wood, E. G. Button, et al. "On Rayleigh optical depth calculations". In: *Journal of Atmospheric and Oceanic Technology* 16 (1999), pp. 1854–1861.

Chapter 4

The impact of spectrum on solar cells

Solar irradiance varies in intensity and spectrum throughout the day. PV cells are sensitive to such spectral fluctuations, as demonstrated by numerous experimental and theoretical studies [1–9]. However, different solar cell technologies exhibit varying degrees of sensitivity to spectral changes in illumination. MJSCs, which are at the heart of most CPV systems, are more sensitive to spectral DNI variation than their Si solar cell counterparts. This is due to the fact that MJSCs are series connected, which results in the worst performing subcell limiting the performance of the entire device. Furthermore, future MJSC designs are expected to incorporate up to six junctions, which makes them even more sensitive to incident solar spectrum variation [10]. As a result, MJSC subcells are designed to be current matched for a particular spectrum, such as for the AM1.5D reference ASTM G173 [11, 12]. Under realistic conditions spectral variations cause MJSC and consequently CPV system performance to deviate from the desired operating point.

This chapter discusses the theory behind a solar cell operation and presents the model for the MJSC, consisting of InGaP, InGaAs, and Ge subcells. This knowledge is applied at quantifying the impact of the aerosol extinction, the ozone and water vapour absorptions on the MJSC's performance.

4.1 A single-junction solar cell theory and operation

4.1.1 Semiconductors

Photovoltaic devices use semiconductor materials to convert the incident sunlight into the electrical energy. The most popular semiconductor for the applications in solar cells and the solid state electronics is Si, a group IV element in the periodic table with 14 orbiting electrons and 14 protons in its nucleus. A pure or intrinsic Si has a three-dimensional tetrahedral lattice structure where atoms are held in their position by covalent bonds, which are formed by a pair of valence electrons, one from each atom. Since a Si atom has four valence electrons, it forms four covalent bonds with neighbouring atoms. At absolute zero temperature (0 K), all of the covalent bonds of Si atoms are intact and there are no free electrons, in other words Si is a perfect insulator in this case. However, at room temperature, thermal energy frees some electrons from the valence band and promotes them to the top energy band, called the conduction band, as demonstrated in Figure 4.1. The void left by an electron creates a positively charged carrier - a hole, which has the charge equal in magnitude to the charge of an electron but with the opposite sign. The electrons in the conduction band and the holes in the valence band contribute to the current flow, but at room temperature Si is a very poor conductor with only one in 10^{10} electrons located in the conduction band [13]. The conductivity of Si is directly proportional to temperature. On the other hand, the conductivity of metals is indirectly proportional to temperature and their conduction band is partially full at all times. This is a primary difference between the metals and the semiconductors.

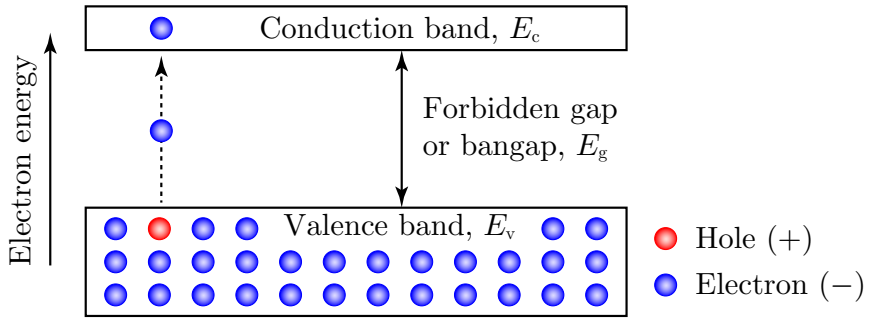

Figure 4.1: The illustration of the thermal generation in a semiconductor material. At the room temperature the thermal energy can promote electrons in a semiconductor to the conduction band, where the current flow is possible. In electron's place, the hole is created in the valence band with equal charge magnitude but opposite sign of the electron.

4.1.2 Bandgap impact on the solar cell efficiency

The bandgap of the semiconductor material fundamentally limits the efficiency of the solar cell as photons with energies lower than the bandgap cannot be absorbed. The photon energy, E_{ph}, is inversely proportional to its wavelength and can be expressed as

$$E_{\text{ph}} = h \cdot f = h \cdot \frac{c}{\lambda}, \tag{4.1}$$

where h is the Planck constant (eV $\cdot$ s), f is the frequency of the photon (Hz), c is the speed of light (m/s), and λ is the wavelength (m). For example, Si with a bandgap of 1.12 eV is optically transparent to photons with energies less than 1.12 eV or wavelengths greater than 1107 nm. This loss mechanism is termed the below-bandgap loss and for a Si solar cell it is equal to 20.0% under AM1.5D conditions, as shown in Figure 4.3.

Photons with energies greater than or equal to the bandgap of a semiconductor can be absorbed. However, excess photon energy above the bandgap is wasted as heat, which is known as the thermalization loss. For a Si solar cell under AM1.5D conditions, this loss is equal to 30.5%, as shown in Figure 4.3. As the photon energy approaches the bandgap, the thermalization loss decreases. For example, 79% of the pre-bandgap IR radiation is available for conversion versus only 33% for the UV radiation, as indicated in Figure 4.3.

After the aforementioned losses, 49.5% of sunlight is left for conversion in a Si solar cell. However, to date the best Si solar cell demonstrated the efficiency of 25% under the AM1.5G spectrum [14]. This discrepancy is due to other loss mechanisms in a solar cell that are not considered in the analysis of Figure 4.3, such as the electron-hole recombination. This fundamental loss is typically considered in the detail balance calculations, which determine the theoretical efficiency limit for single junction solar cells, as was first outlined by W. Shockley and H. J. Queisser in 1961 [15]. Figure 4.3 and its summary in Table 4.1 demonstrate calculated efficiency limits as a function of the bandgap. From these results, Si is one of the most suitable materials for a single junction solar cell.

Table 4.1: Schockley-Queisser efficiency limits for single junction solar cells [15].

Material	Symbol	Bandgap	Efficiency limit
Germanium	Ge	0.67 eV	20.6%
Silicon	Si	1.12 eV	29.5%
Indium phosphate	InP	1.35 eV	30.3%
Gallium arsenide	GaAs	1.43 eV	30.2%
Gallium phosphate	GaP	2.26 eV	20.2%

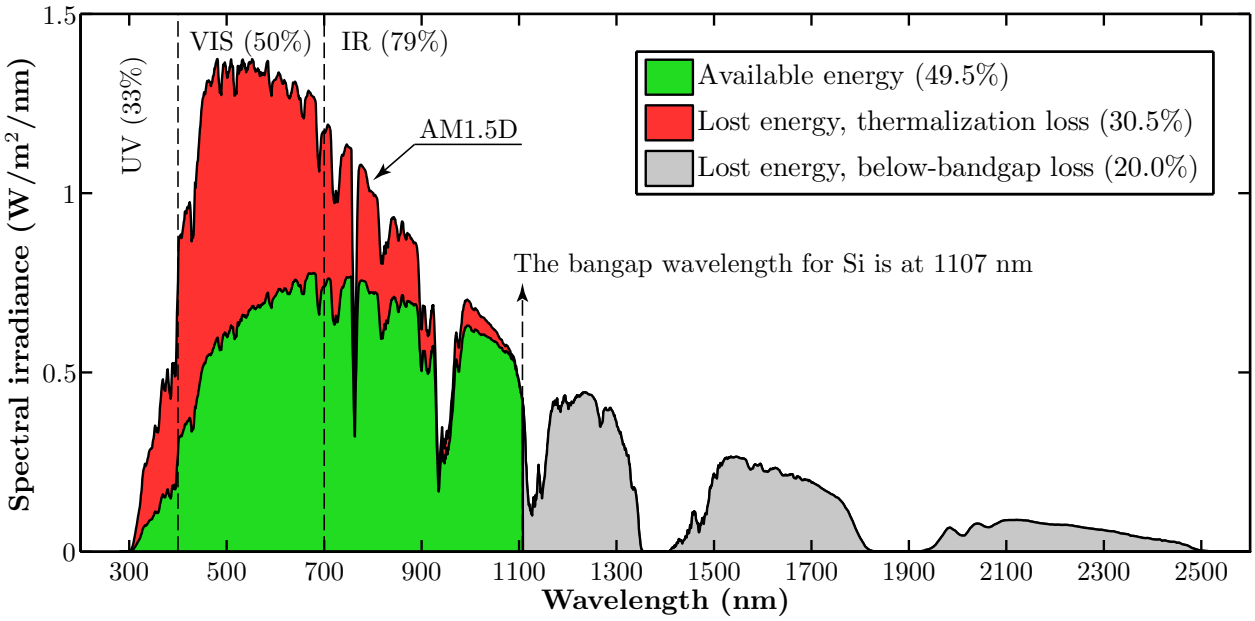

Figure 4.2: Fundamental Si solar cell losses under AM1.5D conditions. About 20.0% and 30.5% of the solar spectrum are lost due to the below-bandgap and the thermalization losses, respectively. The theoretical conversion efficiency for an ideal Si solar cell is 49.5% under the AM1.5D conditions including only the aforementioned losses.

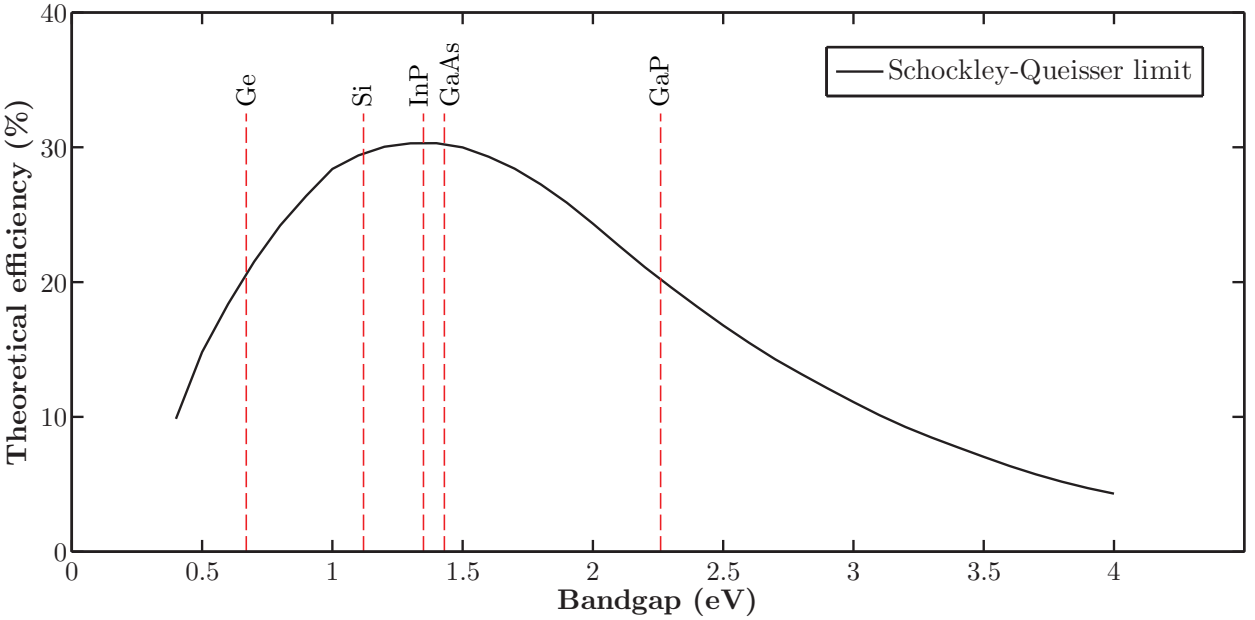

Figure 4.3: Schockley-Queisser efficiency limit for a single junction solar cell at 300 K and under 6000 K blackbody illumination [15]. Si with the bandgap of 1.12 eV at 300 K is one of the ideal choices for material selection in the single junction solar cell design.

4.1.3 The formation of a *p-n* junction

The *p-n* junction is a basic building block for most semiconductor devices, including solar cells. It is formed by joining *p*-type and *n*-type materials with the majority carriers in each area being positively (excess of holes) and negatively (excess of electrons) charged, respectively. A *p*-type semiconductor is created by introducing dopants or impurities to a semiconductor, typically from group III elements, such as boron atoms. Boron is a trivalent atom, which means it is short of one electron to fill its valence band. When boron atoms are introduced into a Si material through the diffusion doping process, each boron atom accepts an electron from a Si crystal, thus forming a covalent bond. Hence, holes become the majority carriers in a Si material, which makes it an *p*-type semiconductor. Analogously, the *n*-type semiconductor is formed by introducing dopants into a semiconductor, usually from group V elements, such as phosphorus atoms. Phosphorus is a pentavalent atom, hence it donates one electron when introduced to a Si material. Therefore, electrons become the majority carriers in a Si crystal, which makes it a *n*-type semiconductor.

Figure 4.4 shows the *p-n* junction when the *p* and *n* materials are first brought together. The holes on the *n* side diffuse to the *p* side, leaving behind the negative charges in the *n* region and give rise to the positive charges in the *p* region by recombining with the free electrons. The electrons from the *n* side behave in analogous manner. As the diffusion process continues, a depletion region develops in the vicinity of the *p* and *n* material interface, as demonstrated in Figure 4.5. The positive and negative charges in the depletion region give rise to the electric field and consequently to the drift current, which opposes the diffusion current. When the drift current is equal to the diffusion current, the unbiased *p-n* junction is at the equilibrium. This condition is maintained by the built-in voltage of the junction, generated from the electric field in the depletion region. The built-in voltage for Si at 300 K is in the range of 0.6 to 0.8 V.

A *p-n* junction can operate in reverse or forward voltage bias. Under reverse bias, electrons and holes are injected to the *p* and *n* sides, respectively. This process increases recombination of the injected electrons with the free holes in the *p* region. The analogous situation occurs with injected holes in the *n* region. Consequently, more negative and positive charges are uncovered by the injected carriers in the *p* and *n* regions, respectively, and the depletion region widens. The opposite situation occurs under forward bias where the injected electrons and holes neutralize some of the positive and negative charges in the depletion region, respectively. As a result, the depletion width and the built-in potential decrease, and more charge carriers diffuse across the junction. The diffusion current becomes significantly greater than the drift current as the forward bias increases.

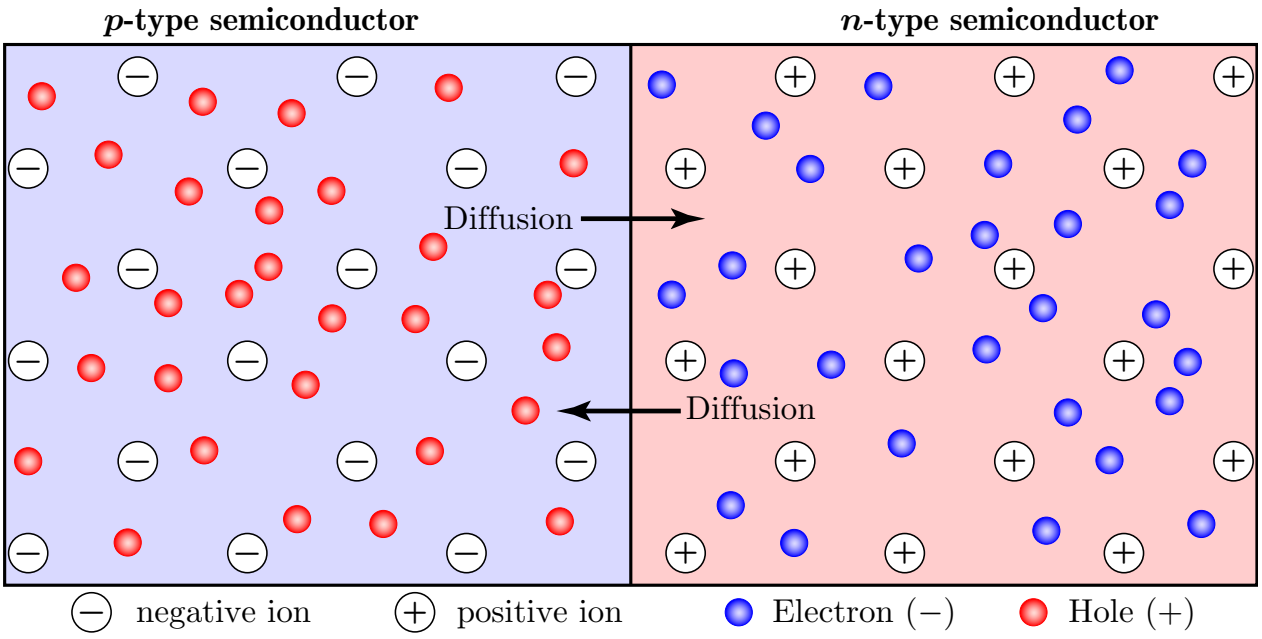

Figure 4.4: Unbiased p-n junction when the p and n materials are first joined. The holes and electrons diffuse to the n and p sides, respectively, thus giving rise to the diffusion current.

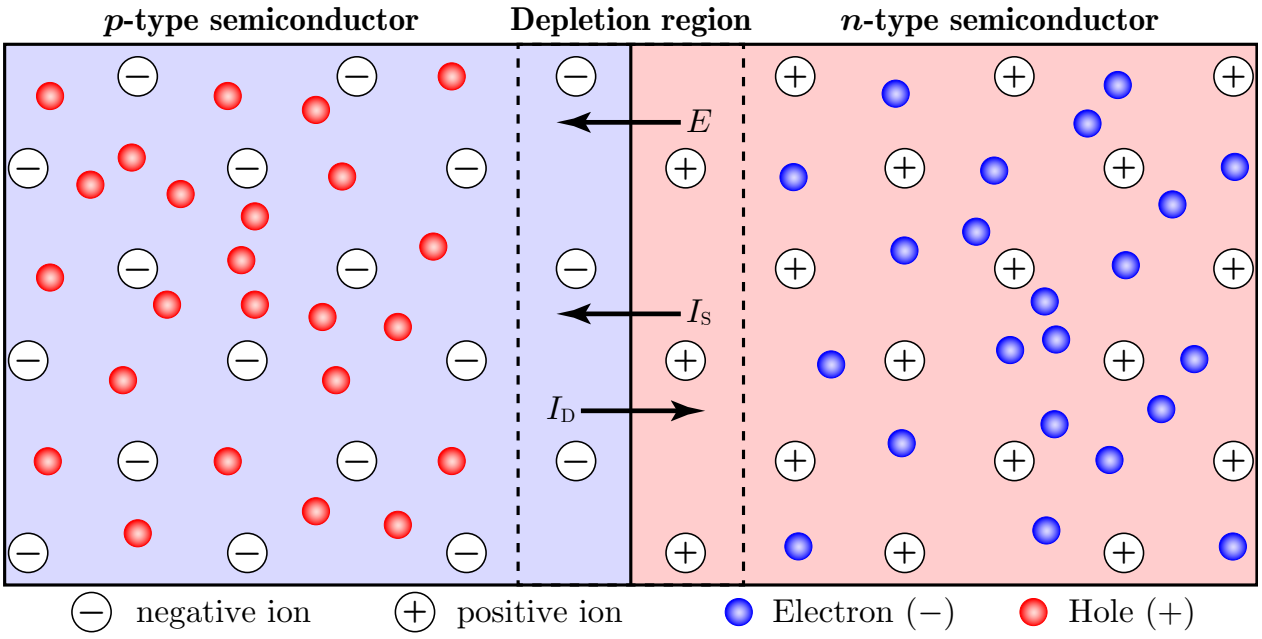

Figure 4.5: Unbiased p-n junction at the equilibrium. As the holes diffuse to the n side, they recombine with the majority electrons on the n side, thus leaving behind negative charges. In the similar manner, the electrons diffusing to the p side leave behind positive charges on the n side. The area depleted of free holes and electrons forms over the p and n regions, which is termed the depletion region. The electric field, E, develops in the depletion region, giving rise to the drift current, I_{S}, which neutralizes the diffusion current, I_{D}.

4.1.4 A *p*-*n* junction as a solar cell

Solar cells are illuminated p-n junctions in forward bias. Typically, a solar cell is arranged with a thin layer of n-type semiconductor on the top (emitter) and a thick layer of p-type semiconductor on the bottom (base), as demonstrated in Figure 4.6. When the p-n junction is exposed to sunlight, incident photons are absorbed by either the n-type or p-type semiconductor and electron-hole pairs can be created, provided the photons have an energy greater than the bandgap of the material. The electrons and holes are swept away by the electric field in the depletion region and are directed toward the top and bottom contacts, respectively. If a load from an external circuit is connected across the terminals, current flow is generated. However, the top and bottom contacts act as high recombination sites for holes and electrons, respectively. To limit the electron-hole recombination and consequently boost the conversion efficiency, the top and bottom contacts are isolated from the emitter and the base with highly doped n++ and p++ regions, respectively, as shown in Figure 4.6. These regions behave like p-n junctions with the electric field opposing the flow of the minority carriers.

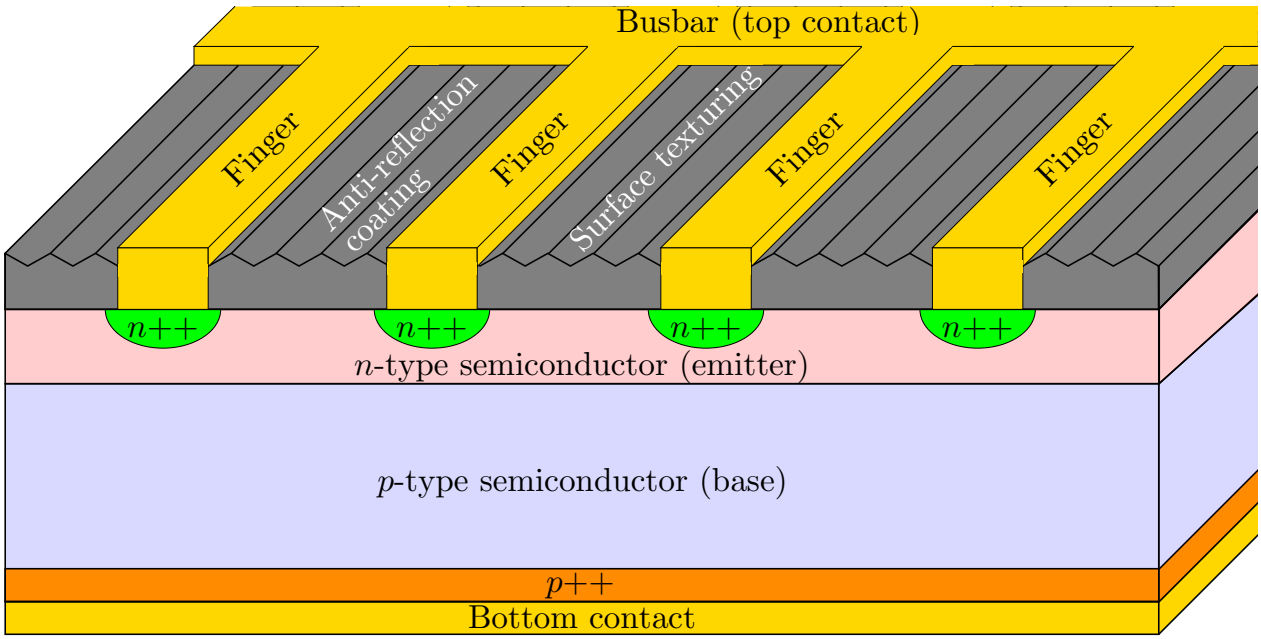

Figure 4.6: Simplified structure of a single junction solar cell. The p-n junction is formed by a thin n-type layer on the top of a thick p-type layer. The top and bottom contacts are used for collecting electrons and holes, respectively, to generate the current flow when the p-n junction is illuminated. To increase photon absorption, solar cells commonly utilize the anti-reflection coating and surface texturing.

A p-type semiconductor is more efficient at carrier collection than an n-type semiconductor of the same doping and thickness, because minority carriers (electrons) in p-type materials have higher mobilities and higher diffusion lengths than minority carriers (holes) in n-type material. For a Si material the primary cause of this phenomenon is acceptor-type impurities [16]. As a result, for Si solar cells the base is typically made from a thick, lightly doped layer of the p-type semiconductor in order to absorb as many photons as possible. On the other side, the emitter consists of a heavily doped, thin layer of the n-type semiconductor to allow more light to pass through to the base. The thickness of the emitter is optimized for low series resistance and high optical transmission. Ultimately, the carrier generation in the emitter can be neglected due to high recombination in this heavily doped layer. For Si solar cells the emitter thickness is in the 0.1 to 2 μm range, while the base thickness varies between 300 and 500 μm [16, 17].

4.1.5 Current-voltage characteristics of a solar cell

A solar cell in the dark or under no illumination acts as a conventional p-n junction diode and its current-voltage (I-V) characteristic is described by the Shockley ideal diode equation

$$I_{\mathrm{d}} = I_0 \cdot \left[\exp\left(qV/nkT\right) - 1\right], \tag{4.2}$$

where I_{d} is the dark current (A) flowing through the diode at the voltage, V, applied from the p-side to the n-side (V), I_0 is the reverse saturation current (A), q is the electron charge (C), k is Boltzmann constant (J/K), n is the ideality factor, which equals to unity for an ideal diode, and T is the junction temperature (K). When the solar cell is illuminated, Equation 4.2 becomes [16]

$$I = I_{\mathrm{sc}} - I_0 \cdot \left[\exp\left(qV/nkT\right) - 1\right], \tag{4.3}$$

where I_{sc} is the photogeneration current (A), commonly referred to as the short circuit current, because that is the current generated by a solar cell under illumination if the top and bottom contacts are shorted. For practical applications, Equation 4.3 must be altered to consider the parasitic effects of series and shunt resistances in a solar cell [16]

$$I = I_{\mathrm{sc}} - I_0 \cdot \left(\exp\left[\frac{q(V + I \cdot R_{\mathrm{s}})}{nkT}\right] - 1\right) - \left(\frac{V + I \cdot R_{\mathrm{s}}}{R_{\mathrm{p}}}\right), \tag{4.4}$$

where R_{s} and R_{p} are series and parallel (or shunt) resistances, respectively. Figure 4.7 shows the equivalent circuit for a single junction solar cell incorporating these aforementioned parasitic resistances.

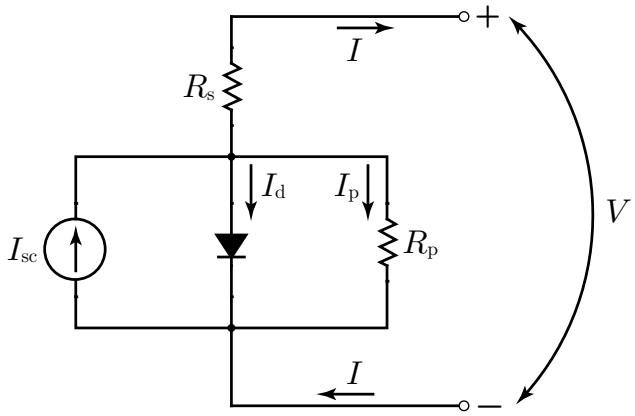

Figure 4.7: An equivalent circuit for a single junction solar cell. The parasitic series and parallel resistances, R_s and R_p, respectively, reduce the voltage and current generated by a solar cell.

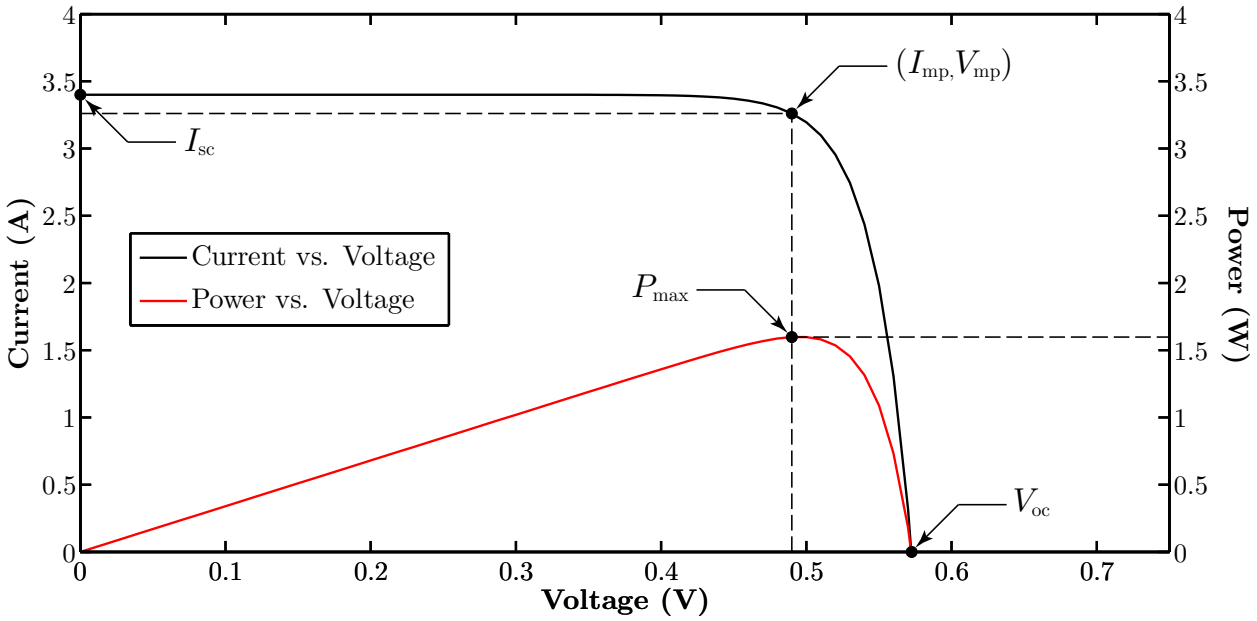

Figure 4.8: The I-V and P-V curves of a solar cell with no parasitic resistances. The I-V curve is defined by the short circuit current, I_{sc} (no load), the open circuit voltage, V_{oc} (infinite load), and the maximum power point, P_{max}.

Equation 4.3 can be used to generate the I-V curve for an ideal solar cell, as shown in Figure 4.8. The I-V curve is defined by the short circuit current, the open circuit voltage, and the maximum power point. The short circuit current and the open circuit voltage define the maximum available current and voltage from a solar cell. The product of these quantities yield the maximum theoretical power the given solar cell can produce. To evaluate how well a

solar cell is performing, the fill factor (FF) is commonly used, which describes the squareness of an I-V curve as

$$FF = \frac{V_{\mathrm{mp}} \cdot I_{\mathrm{mp}}}{V_{\mathrm{oc}} \cdot I_{\mathrm{sc}}} = \frac{P_{\max}}{V_{\mathrm{oc}} \cdot I_{\mathrm{sc}}}. \tag{4.5}$$

For example, the FF for the solar cell in Figure 4.8 is about 82%, which is considered to be very good. For comparison, the current record-holding Si solar cell has a FF of 82.8% and an efficiency of 25% under the AM1.5G solar spectrum [14]. The efficiency is the most important metric of a solar cell and it can be expressed as

$$\eta = \frac{V_{\mathrm{mp}} \cdot I_{\mathrm{mp}}}{P_{\mathrm{in}}} = \frac{P_{\max}}{P_{\mathrm{in}}}, \tag{4.6}$$

where P_{in} is the incident optical power on the surface of a solar cell.

4.1.6 The effect of temperature, irradiance, and parasitic resistances on the I-V characteristics of a solar cell

Equation 4.4 can be used for observing the effect of temperature, irradiance, and parasitic resistances on a solar cell performance. Prior to this investigation it is necessary to derive the reverse saturation current, which for a Si solar cell is given by [16]

$$I_0 = A \cdot q {n_{\mathrm{i}}}^2 \cdot \left(\frac{D_{\mathrm{n}}}{N_{\mathrm{a}} L_{\mathrm{n}}} + \frac{D_{\mathrm{p}}}{N_{\mathrm{d}} L_{\mathrm{p}}} \right), \tag{4.7}$$

where A is the junction area (cm^2), q is the electron charge (C), n_{i} is the intrinsic carrier concentration (cm^{-3}), D_{n} and D_{p} are the diffusion coefficients of electron and hole (cm^2/s), respectively, L_{n} and L_{p} are the diffusion lengths of electron and hole (cm), respectively, N_{a} and N_{d} are doping concentrations in a p-type and n-type semiconductors (cm^{-3}), respectively. Most of the aforementioned parameters are influenced by temperature, however, n_{i} has a particularly strong temperature dependence. Therefore, for simplicity it is assumed that all parameters in Equation 4.7 are constant with temperature, except n_{i}, which is formulated as [18]

$$n_{\mathrm{i}}(T) = 5.29 \times 10^{19} \cdot (T/300)^{2.54} \cdot \exp(-6726/T). \tag{4.8}$$

Table 4.2 shows the parameters, including the reverse saturation current, for practical Si solar cell. These parameters along with Equations 4.4, 4.7 and 4.8 can be used to generate the I-V curves for this specific Si solar cell at any temperature, light intensity, and parasitic resistances.

Table 4.2: Parameters for a practical Si solar cell [13].

Parameter	Symbol	Value
Short circuit current	I_{sc}	3.4 A*
Reverse saturation current	I_0	6×10^{-10} A*
Series resistance	R_{s}	0.005 Ω
Parallel resistance	R_{p}	6.6 Ω

*at DNI = 1000 W/m^2 and $T = 25$ °C

Figure 4.9 shows the behaviour of the I-V curve as the temperature is varied from 250 to 370 K for a Si solar cell with parameters in Table 4.2. The open circuit voltage linearly decreases with increase in temperature. A plot of the open circuit voltage versus temperature can be generated to extract the open circuit voltage temperature coefficient, which in this case is -2.405 mV/C°. On the other hand, the short circuit current slightly increases with temperature because the bandgap of the semiconductor decreases and more photons have enough energy to generate electron-hole pairs. However, this effect is very small, with the short circuit current temperature coefficient being around +0.06%/C° for a typical Si solar cell [19].

The effect of varying light intensity on the I-V curve is demonstrated in Figure 4.10, where the DNI decreases uniformly from 1000 W/m^2 to 100 W/m^2. Evidently, the short circuit current decreases linearly with decrease in irradiance. On the other hand, the open circuit voltage has a logarithmic dependence on the short circuit current and, by extension, on the incident irradiance, which is deduced from rearranging Equation 4.3 at V_{oc} conditions in an ideal solar cell as

$$V_{\text{oc}} = \frac{nkT}{q} \cdot \ln\left(\frac{I_{\text{sc}}}{I_0} + 1\right). \tag{4.9}$$

Ideally, it is desired to have a solar cell with no series and shunt resistances. However, in practise, contact resistances and impurities near the p-n junction result in series and shunt resistances, respectively. The shunt resistance reduces the current generated by a solar cell. From Figure 4.11 it can be seen that as the forward voltage increases, the current loss due to shunt resistance increases as well. On the other hand, as series resistance increases, the forward voltage across the p-n junction and current decreases, which results in a reduction of the maximum power the solar cell can produce, as shown in Figure 4.12. Moderate series resistance has little effect on the I-V curve at low forward voltages because the short circuit current term in Equation 4.4 dominates.

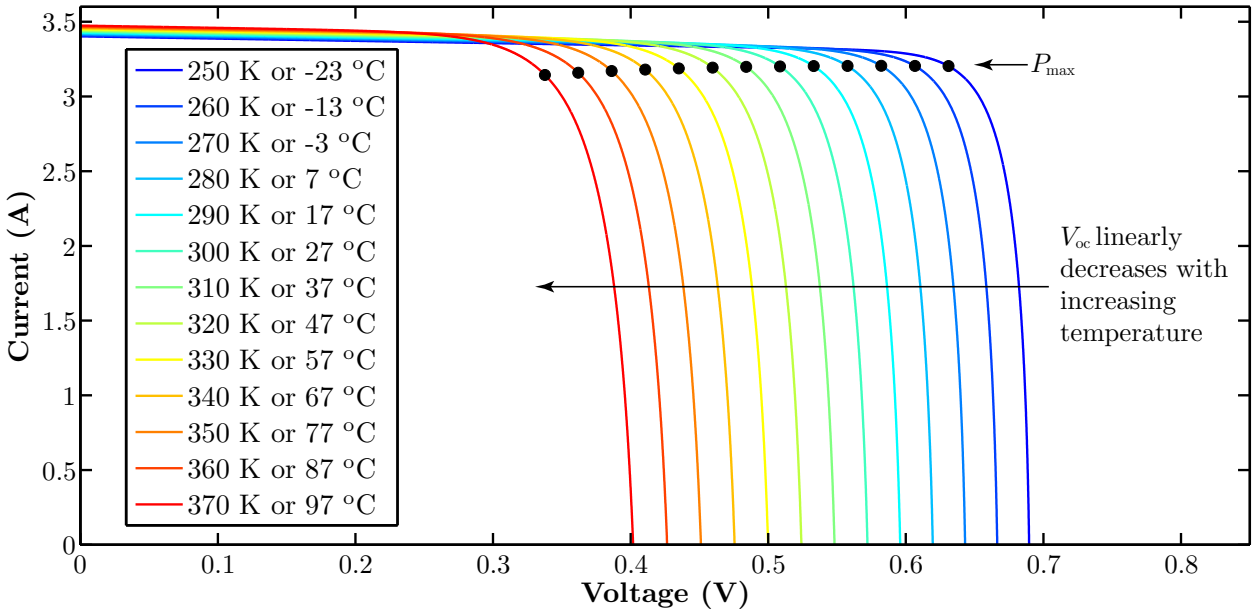

Figure 4.9: The effect of temperature on the I-V curve of Si solar cell. The open circuit voltage, V_{oc}, linearly decreases with increasing temperature, while the short circuit current, I_{sc}, rises slightly under these conditions. The maximum power decreases as the temperature increases, mainly due to the shift of the voltage at the maximum power point.

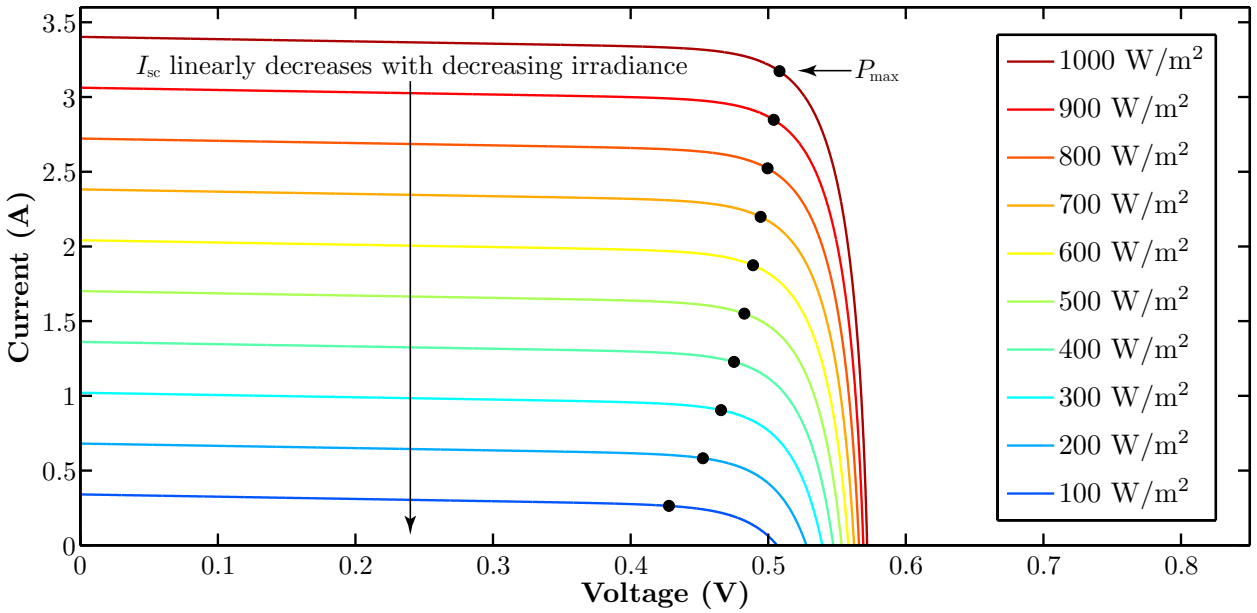

Figure 4.10: The effect of the irradiance on the I-V curve of Si solar cell. The short circuit current, I_{sc}, linearly decreases with decreasing irradiance, while the open circuit voltage, V_{oc}, decreases logarithmically under these conditions. The maximum power, P_{max}, decreases as the irradiance decreases, due to current reduction at the maximum power point.

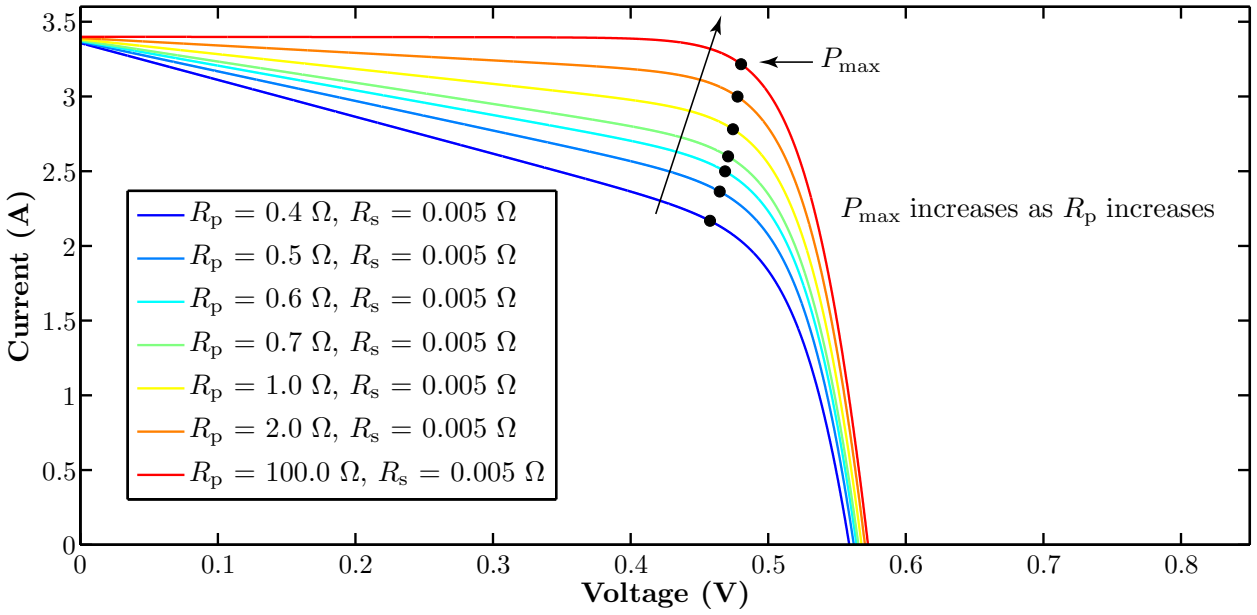

Figure 4.11: The effect of shunt resistance on the I-V curve of Si solar cell. As the shunt resistance increases, the maximum power and with it the FF of the solar cell increases.

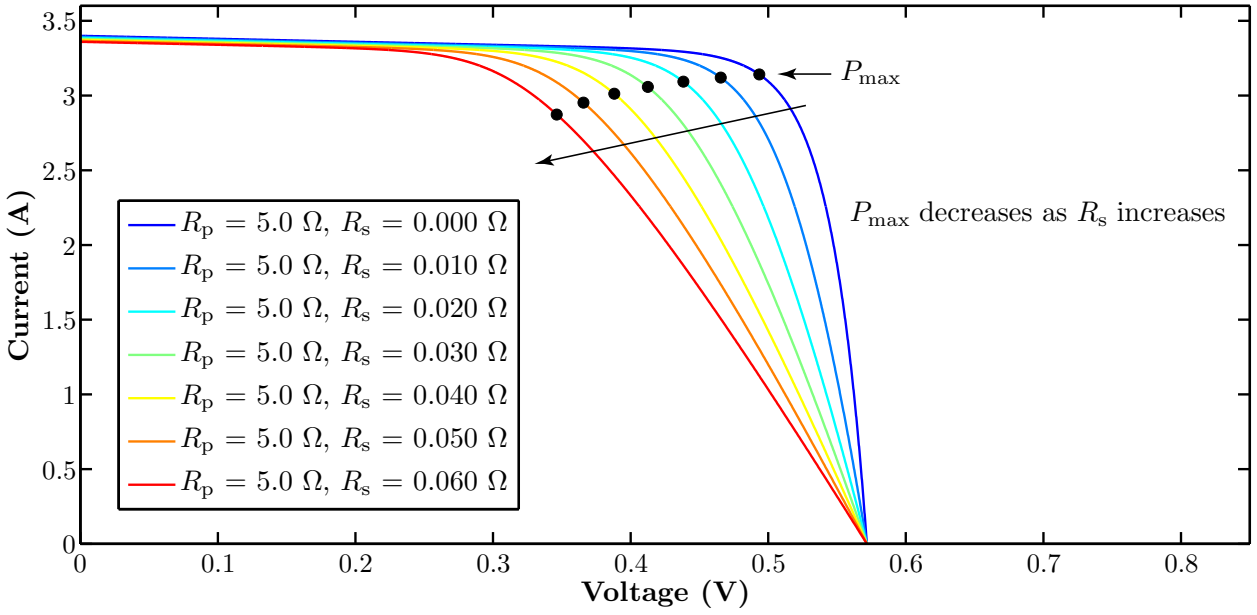

Figure 4.12: The effect of series resistance on the I-V curve of Si solar cell. As the series resistance increases, the maximum power and with it the FF of the solar cell decreases.

4.1.7 External quantum efficiency

The external quantum efficiency (EQE) is the probability of electron-hole generation when an energy-specific photon strikes a semiconductor material. It is dependent on the material absorption, the collection and charge separation efficiencies of the generated carriers by the *p-n* junction. Therefore, the EQE is an important parameter that gives insight into the solar cell operation under different spectral conditions. In particular, the short circuit current of a solar cell can be expressed through the EQE as

$$I_{sc} = A_s \cdot \int_0^{\lambda_g} S(\lambda) \cdot EQE(\lambda) \cdot \frac{q\lambda}{hc} \cdot d\lambda, \tag{4.10}$$

where A_s is the area of a solar cell (m^2), λ_g is the wavelength at the bandgap, $S(\lambda)$ is the spectral irradiance ($W/m^2/nm$), and $EQE(\lambda)$ is the EQE ranging from 0 to 100%. Equation 4.10 can be re-written as

$$I_{sc} = A_s \cdot \int_0^{\lambda_g} S(\lambda) \cdot R(\lambda) \cdot d\lambda, \tag{4.11}$$

where $R(\lambda)$ is the responsivity (A/W). Figure 4.13 demonstrates a typical EQE and the corresponding responsivity of a Si solar cell. The front and back surface recombinations primarily cause the reduction of the EQE in regions ① and ③, respectively, while the reflection and low diffusion lengths of carriers are responsible for non-ideal EQE in region ②.

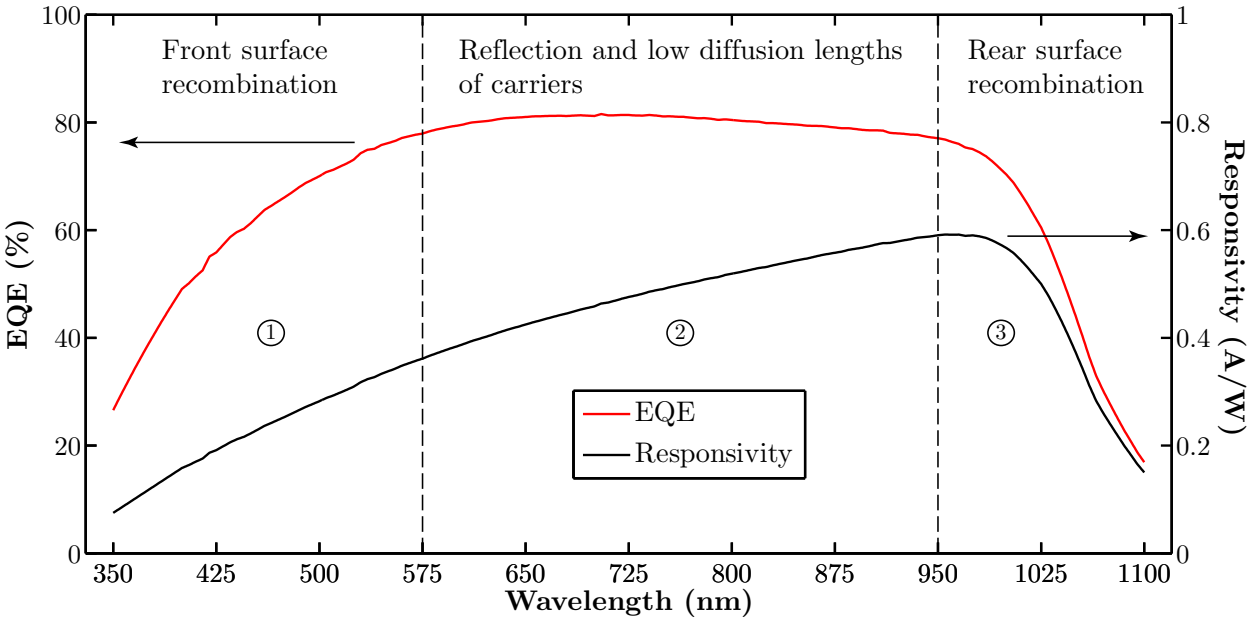

Figure 4.13: Typical EQE and responsivity of a Si solar cell. The front and back surface recombinations, reflection, and low diffusion lengths result in the non-ideal EQE (< 100%).

4.2 Multi-junction solar cells

The previous section described in detail the fundamental principles behind a single-junction solar cell and the factors limiting its performance. At present, a Si solar cell is the most popular PV device on the market, but it has a theoretical efficiency limit of only 29.5% [15]. In a continuous effort to improve the solar cell efficiency, MJSCs offer an enormous potential with record efficiency presently being at 44% at 942 suns concentration of the AM1.5D spectrum [14]. A MJSC consists of several stacked junctions of different bandgaps, where each junction absorbs a certain portion of the solar spectrum. This topology reduces below-bandgap and thermalization losses and leads to a higher efficiency as compared to a Si solar cell.

Figure 4.14a shows the simplified structure of a common triple junction solar cell (TJSC), consisting of InGaP, InGaAs, and Ge subcells from top to bottom, respectively. Only photons with energies greater than 0.65 eV can be absorbed by the TJSC. The junction-specific absorption of incident light at the bandgaps in Figure 4.14a is categorized as

- top subcell - up to 681 nm,
- middle subcell - between 682 and 886 nm, and
- bottom subcell - between 887 and 1907 nm.

Each pair of subcells is connected by a tunnel junction, which prevents a voltage drop between two directly connected p-n junctions, and creates an effective potential barrier for minority carriers in each respective junction [20].

The equivalent circuit for a TJSC is an extension of the single junction model from Figure 4.7. Therefore, three subcells connected in series can be modelled by the circuit in Figure 4.14b. The voltage of a TJSC is a sum of all subcell voltages. On the other hand, the current of a TJSC is limited by the lowest current-producing subcell. The latter represents a challenge for solar cell designers as the subcell current depends on the incident spectrum, which is strongly influenced by highly-varying atmospheric conditions. In the subsequent section, a model for the TJSC is introduced for the purpose of observing the spectral sensitivity of this device, as the effect of the individual atmospheric constituents is varied.

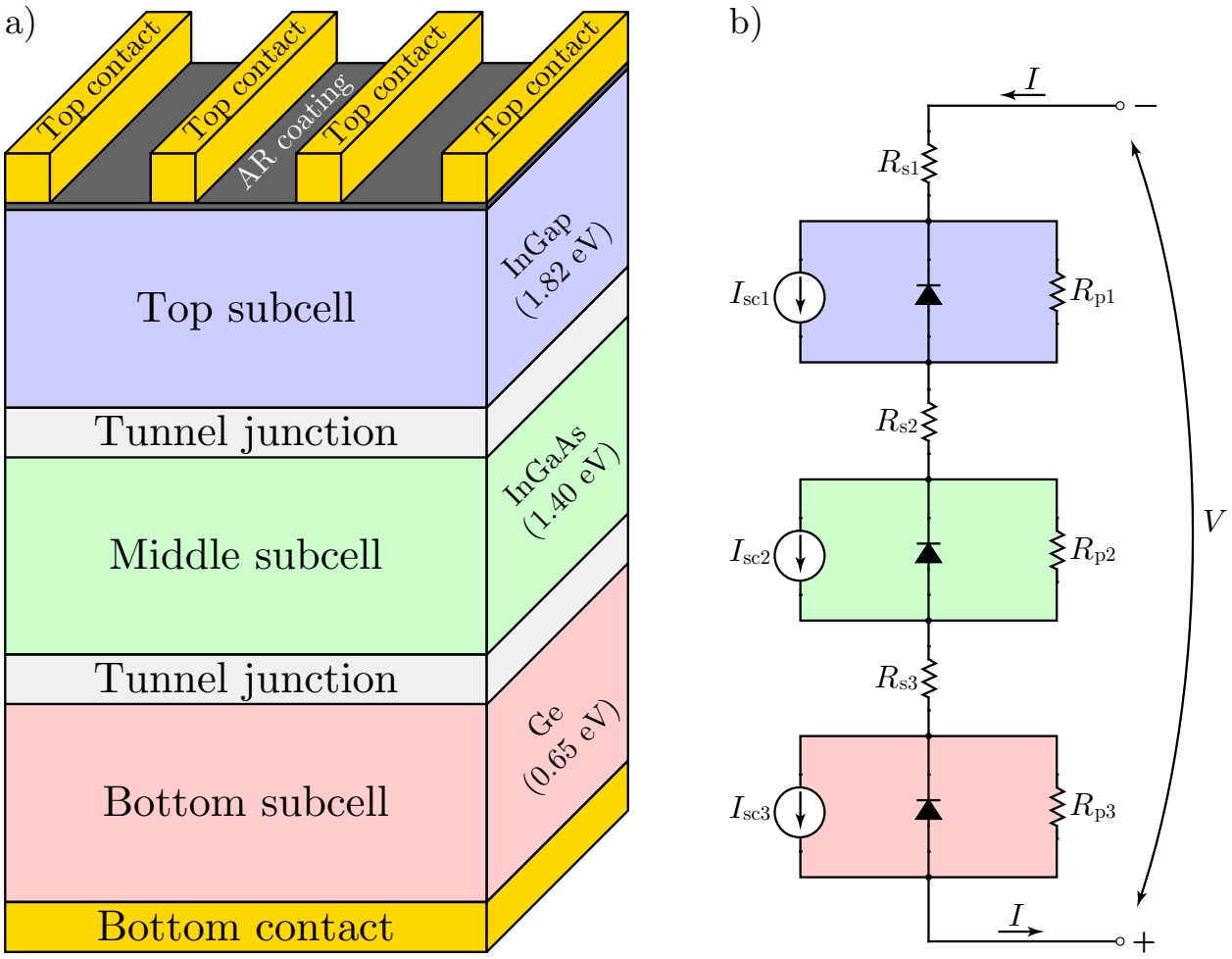

Figure 4.14: a) The simplified structure of a TJSC consisting of three subcells at different bandgaps. Each pair of subcells is connected via a tunnel junction, which acts as a low-Ohmic link between two p-n junctions. This topology results in increased efficiency as compared to a Si solar cell due to reduced below-bandgap and thermalization losses. b) The equivalent circuit for a TJSC, which is an extension of the single junction model from Figure 4.7. Since the subcells are series connected, the voltages of each subcell add up, while the current of the lowest-producing subcell prevails.

4.2.1 Model of a triple-junction solar cell

The dark current of a single junction solar cell can be expressed as [16]

$$I_{\mathrm{d}} = I_{\mathrm{diff}} \cdot \left[\exp\left(\frac{qV}{kT}\right) - 1\right] + I_{\mathrm{rad}} \cdot \left[\exp\left(\frac{qV}{kT}\right) - 1\right] + I_{\mathrm{scr}} \cdot \left[\exp\left(\frac{qV}{2kT}\right) - 1\right], \tag{4.12}$$

where I_{diff} is the diffusion current, I_{rad} is the radiative recombination current, and I_{scr} is the current due to recombination in the space charge (SCR) or depletion region. In indirect bandgap materials, such as Si, radiative and SCR recombination currents are not significant and can be ignored [16]. Therefore, for Si the reverse saturation current is primarily due to diffusion current and Equation 4.12 simplifies to Equation 4.2. Although a TJSC contains the materials with both direct and indirect bandgaps, such as InGaAs and Ge, respectively, all terms in Equation 4.12 for each junction are typically preserved. Since the diffusion and the radiative recombination currents have the same exponential terms, usually they are combined and named the reverse saturation current, I_0, and the dark current is written as [21]

$$I_{\mathrm{d}} = I_0 \cdot \left[\exp\left(\frac{qV}{kT}\right) - 1\right] + I_{\mathrm{scr}} \cdot \left[\exp\left(\frac{qV}{2kT}\right) - 1\right]. \tag{4.13}$$

The I-V relationship for each junction of a TJSC is an extension of Equation 4.4 and is written as

$$I = I_{\mathrm{sc}} - I_0 \cdot \left[\exp\left(\frac{qV_{\mathrm{s}}}{kT}\right) - 1\right] - I_{\mathrm{scr}} \cdot \left[\exp\left(\frac{qV_{\mathrm{s}}}{2kT}\right) - 1\right] - \frac{V_{\mathrm{s}}}{R_{\mathrm{p}}}, \tag{4.14}$$

where $V_{\mathrm{s}} = V + I \cdot R_{\mathrm{s}}$ is the voltage across the junction with added series resistance effect. The I-V curve fitting can be carried out to extract the diode parameters R_{s}, R_{p}, $I_0(T_{\mathrm{nom}})$, and $I_{\mathrm{scr}}(T_{\mathrm{nom}})$, where T_{nom} is the reference temperature. The temperature dependence of the reverse saturation and the SCR recombination currents is given by [21]

$$I_0(T) = I_0(T_{\mathrm{nom}}) \cdot \left(\frac{T}{T_{\mathrm{nom}}}\right)^{X_{\mathrm{t}}} \cdot \exp\left[-\frac{q}{k} \cdot \left(\frac{E_{\mathrm{g}}(T)}{T} - \frac{E_{\mathrm{g}}(T_{\mathrm{nom}})}{T_{\mathrm{nom}}}\right)\right], \tag{4.15}$$

$$I_{\mathrm{scr}}(T) = I_{\mathrm{scr}}(T_{\mathrm{nom}}) \cdot \left(\frac{T}{T_{\mathrm{nom}}}\right)^{X_{\mathrm{t}}/2} \cdot \exp\left[-\frac{q}{2k} \cdot \left(\frac{E_{\mathrm{g}}(T)}{T} - \frac{E_{\mathrm{g}}(T_{\mathrm{nom}})}{T_{\mathrm{nom}}}\right)\right], \tag{4.16}$$

where X_{t} is the temperature exponent. Since I_0 dominates at high biases due to unity ideality factor, at V_{oc} it can be expressed as [21]

$$I_0(T) = I_{\mathrm{sc}}(T) \cdot \left[\exp\left(\frac{qV_{\mathrm{oc}}(T)}{kT}\right) - 1\right]^{-1}. \tag{4.17}$$

Therefore, if the temperature characteristics of I_{sc} and V_{oc} are known, X_{t} can be obtained by using Equations 4.15 and 4.17.

Table 4.3 shows the extracted diode parameters and temperature exponent from measured *I-V* curves of the InGaP, InGaAs, and Ge isotypes at the University of Ottawa [22]. The series and parallel resistances were estimated from values found in the literature for a similar TJSC. The main sources of series resistance in a TJSC are tunnel junctions, lateral, and electrode resistances. For the top subcell the series resistance will arise from lateral and electrode resistance, while for the middle and bottom subcells - from the tunnel junctions.

The additional parameters in Table 4.3 show the Varshni's coefficients, which are used in Varshni's equation to determine the bandgap of a semiconductor at varying temperatures as [23]

$$E_g(T) = E_{\mathrm{g}}(0) - \frac{\alpha \cdot T^2}{T + \beta}, \tag{4.18}$$

where $E_{\mathrm{g}}(0)$ is the bandgap of the material at 0 K, α and β are empirically-determined temperature coefficients. The Varshni equation is used in simulations to adjust the EQE of each subcell as the temperature varies. Figure 4.15 shows the EQE of the InGaP\InGaAs\Ge TJSC at 25°C measured at the University of Ottawa [22]. Knowledge of the EQE is the last parameter required to perform spectral sensitivity simulations for this specific TJSC.

Table 4.3: Extracted diode parameters and temperature exponent from measured *I-V* curves of the InGaP, InGaAs, and Ge isotypes under varying temperature and intensity [22]. The series and parallel resistances were taken from literature [21, 24]. At the bottom, the Varshni coefficients for bandgap determination of isotypes at different temperatures [25].

		Subcell			
		Top	*Middle*	*Bottom*	
Parameter		**InGaP**	**InGaAs**	**Ge**	**Units**
Reference temperature	T_{nom}	26	44	44	C°
Reverse saturation current	$I_0{}^*$	1.577×10^{-21}	1.259×10^{-14}	7.914×10^{-3}	A/m^2
Recombination current	$I_{\mathrm{scr}}{}^*$	4.727×10^{-10}	6.116×10^{-6}	1.587	A/m^2
Series resistance	R_{s}	1.297×10^{-6}	6.594×10^{-8}	4.396×10^{-8}	Ω·m^2
Parallel resistance	R_{p}	1600	450	0.054	Ω·m^2
Temperature exponent	X_{t}	2.31	2.07	1.35	N/A
Bandgap at 0 K	$E_{\mathrm{g}}(0)$	1.879	1.519	0.75	eV
Varshni's coefficient	α	6.12×10^{-4}	5.41×10^{-4}	4.77×10^{-4}	eV/K
Varshni's coefficient	β	350	204	235	K

*at T_{nom}

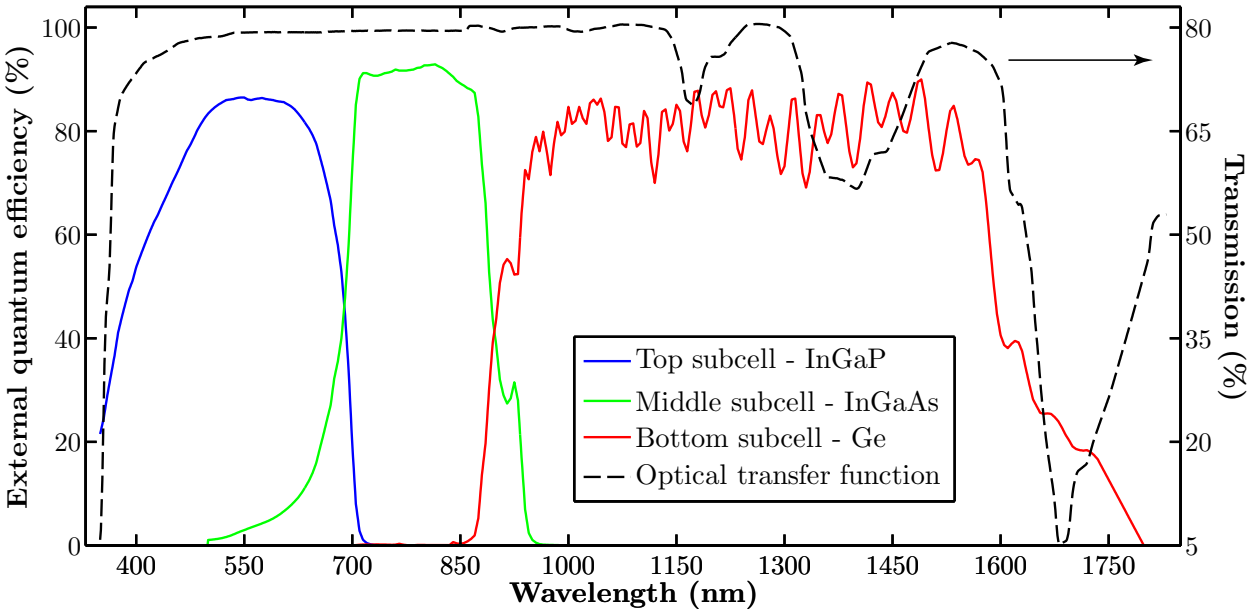

Figure 4.15: The EQE of the InGaP\InGaAs\Ge TJSC at 25°C measured at the University of Ottawa [22]. Also shown is the assumed optical transfer function for the CPV module in the simulations.

4.2.2 Spectral sensitivity of a triple-junction solar cell

In the previous section, a model for the InGaP\InGaAs\Ge TJSC was presented. This section utilizes the aforementioned model to assess the spectral impacts on the performance of the TJSC. Since the TJSCs are typically a part of a CPV system, a simulated CPV module's optical transfer function (OTF) as shown in Figure 4.15 is assumed. It consists of a 3 mm-thick Fresnel lens coupled with a 10 mm-thick glass secondary optic, all of which is assumed to give a concentration ratio of 500 times. Furthermore, the cell temperature is assumed to be constant throughout the day at 65°C to isolate only the spectral effects on the TJSC's performance. To simulate the effect of individual atmospheric constituents on the TJSC, four sets of the solar spectra for each constituent are generated from early morning until the solar noon with 10 min increments on June 21st, 2014 in Ottawa, Canada. Only one of, aerosol extinction, ozone, and water vapour absorptions, is varied from one set of solar spectra to the other, while the other constituents are kept the same across all sets. However, in all cases the spectral effect of the AM is present. The simulation on the day of the summer solstice is done to achieve the greatest AM changes possible.

Aerosols extinction effect

Figure 4.16 shows the simulated efficiency of the TJSC throughout the day as aerosol extinction is varied from one extreme to the other. (Note, the cell efficiency is defined as the ratio of the TJSC's output electrical power to the input optical power in the 350–1830 nm spectral range). The ozone and water vapour path-lengths are set constant as 0.345 cm and 1.42 cm, respectively, which is the case for the AM1.5D spectrum. Therefore, the data point where the AM is 1.5 and the AOD at 500 nm is 0.084 corresponds to the AM1.5D input spectrum. Figure 4.16 demonstrates that the highest peak efficiency occurs for the lowest aerosol extinction. It can be explained by observing the current density at the maximum power point, J_{mp}, of each subcell, as shown in Figure 4.17. For low aerosol optical depth, the J_{mp} of each subcell are better matched and as a result the efficiency is higher. In other words, the point where the spread between the J_{mp} of each subcell is the lowest corresponds to the peak efficiency. Furthermore, the TJSC's FF from Figure 4.18 leads to an interesting observation that the highest efficiency occurs at the lowest FF. For example, if the top subcell is severely current limited, the bottom subcell is forced to operate close to its V_{oc}. Thus, the bottom subcell contributes nearly vertical portion of its I-V curve to the resultant TJSC's I-V curve. In this case the FF is higher as compared to when the bottom subcell is operating at the J_{mp}. Ultimately, high aerosol extinction reduces the TJSC's efficiency and consequently the generated power, as shown in Figure 4.19.

Ozone absorption effect

Figure 4.20 shows the TJSC's efficiency throughout the day under different ozone absorption scenarios. The peak efficiency is the highest for the lowest ozone absorption. For the higher ozone path-length scenarios, the top subcell remains current-limiting for a longer period of time, as demonstrated in Figure 4.21. In other words, the crossing between the J_{mp} of the top and the middle subcells is later in the day. This point also corresponds to the lowest FF, which, as explained earlier, indicate the best current matching between the subcells. Ultimately, Figure 4.23 shows that the overall power from the TJSC is mostly unaffected by the ozone absorption for the AM lower than 1.93. However, for the higher AM the TJSC performs better at the lowest ozone absorption.

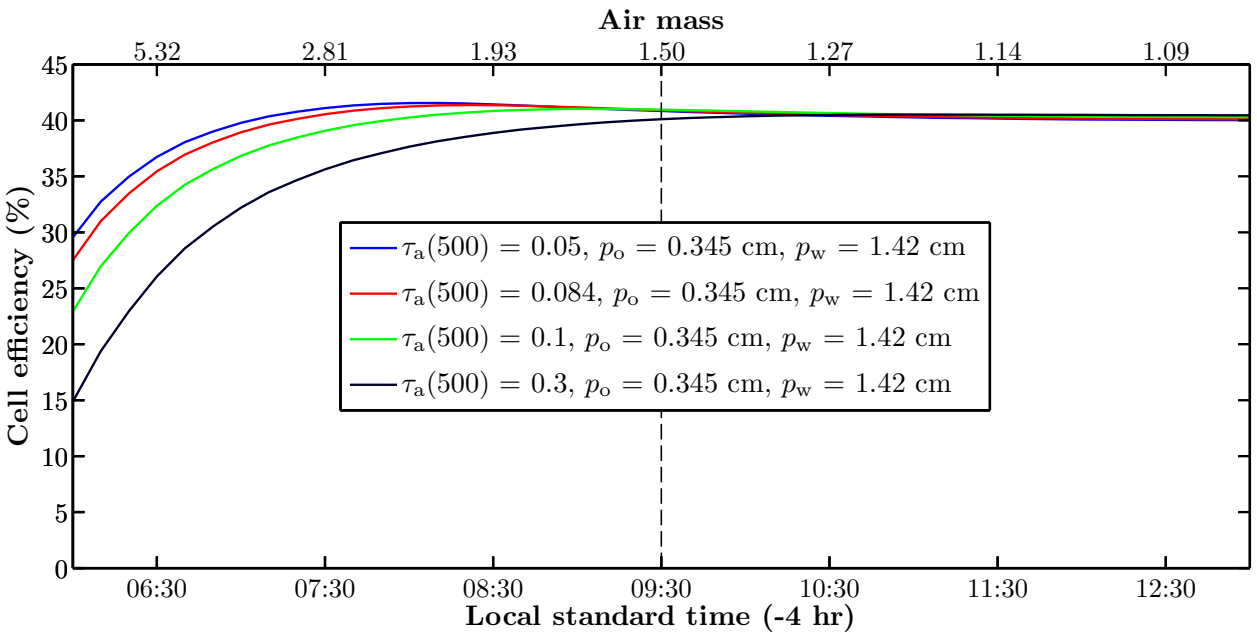

Figure 4.16: The effect of the aerosol extinction on the TJSC's efficiency. High aerosols content leads to a lower cell efficiency for AM greater than 1.5, but for lower AM it has little effect on the efficiency.

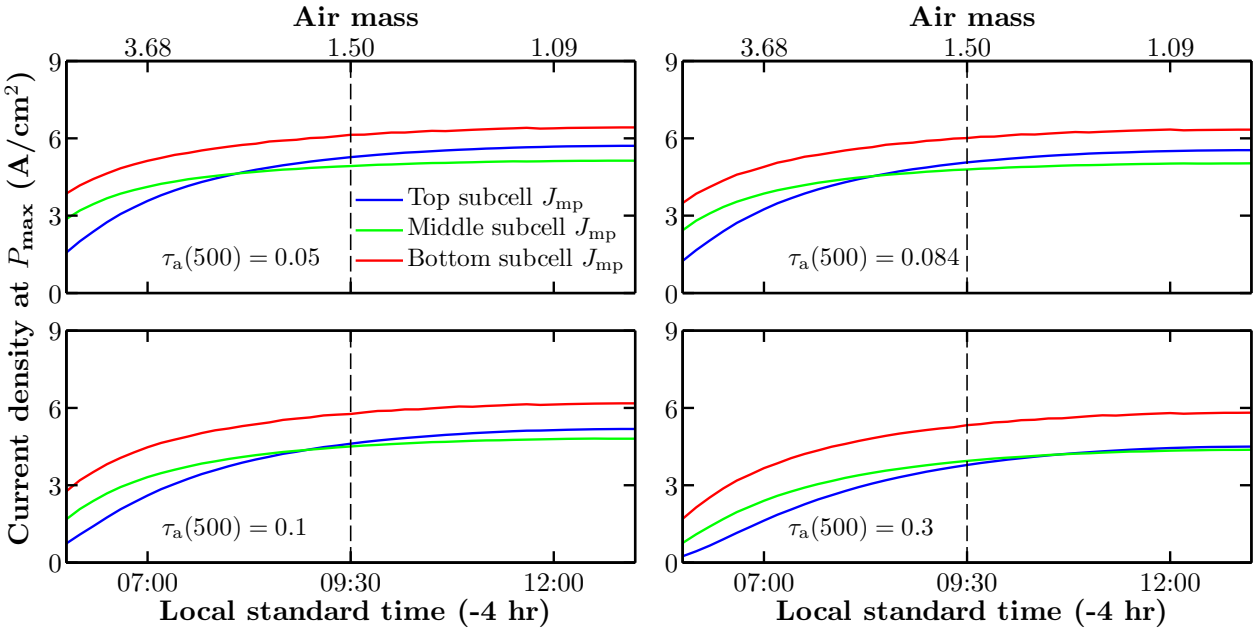

Figure 4.17: Subcell currents at the maximum power point for different aerosol extinction scenarios. High aerosols content leads to a greater mismatch between the subcell currents.

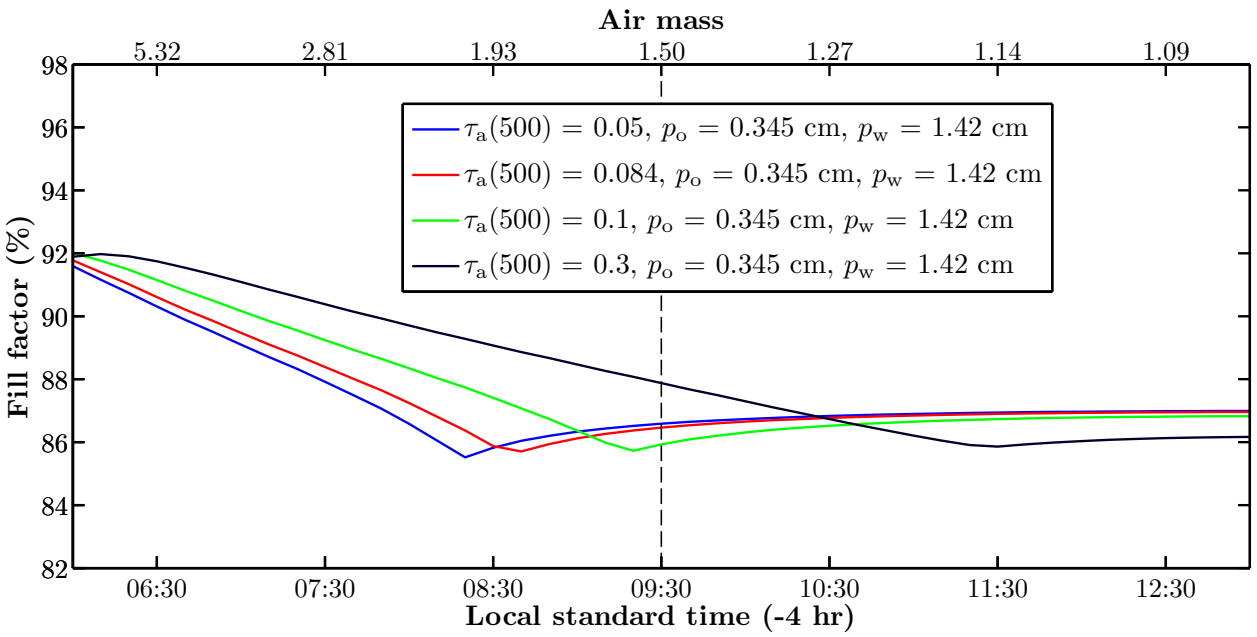

Figure 4.18: The FF of the TJSC under varying levels of aerosols. The lowest FF corresponds to the highest efficiency throughout the day, as it represents the point where the best subcell current matching occurs. For higher aerosol extinction this point occurs later in the day.

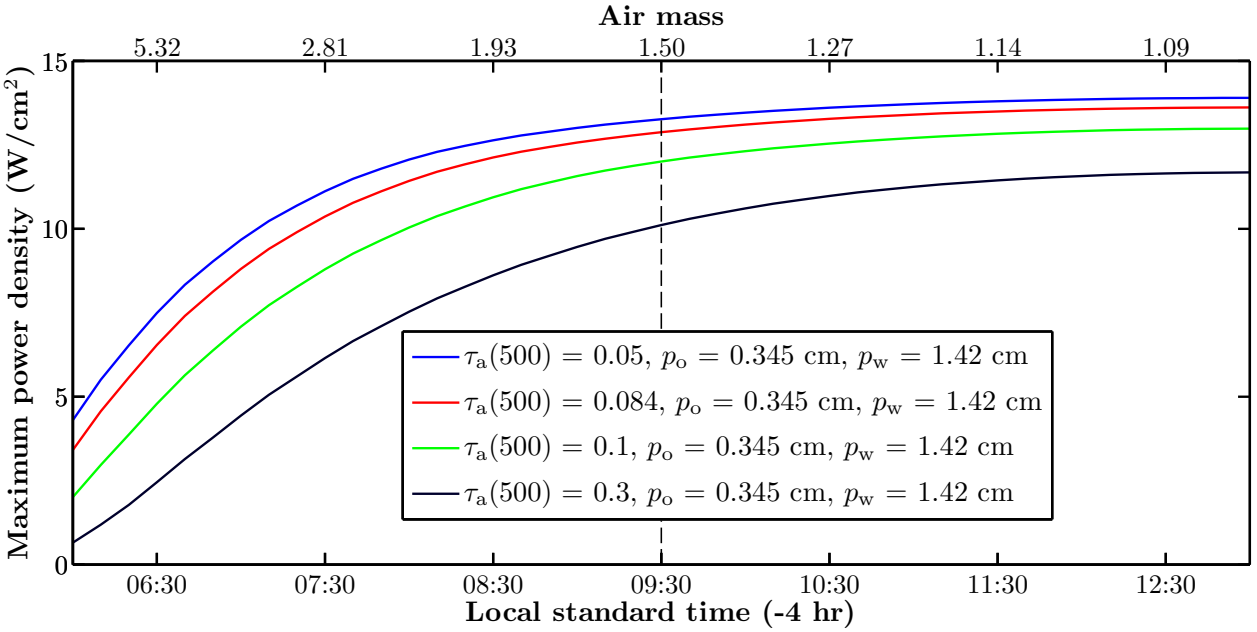

Figure 4.19: The output power of the TJSC under varying aerosols content. High aerosol extinction decreases cell's output power.

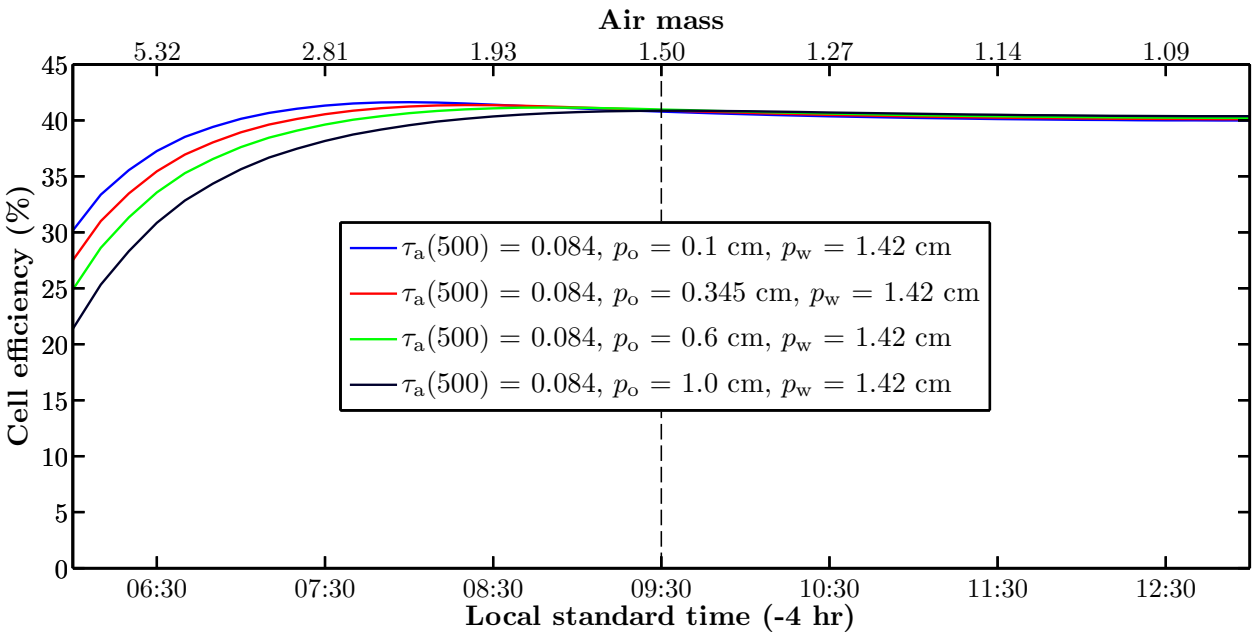

Figure 4.20: The effect of the ozone absorption on the TJSC's efficiency. High ozone content leads to a lower cell efficiency for AM greater than 1.5, but for lower AM it has little effect on the efficiency.

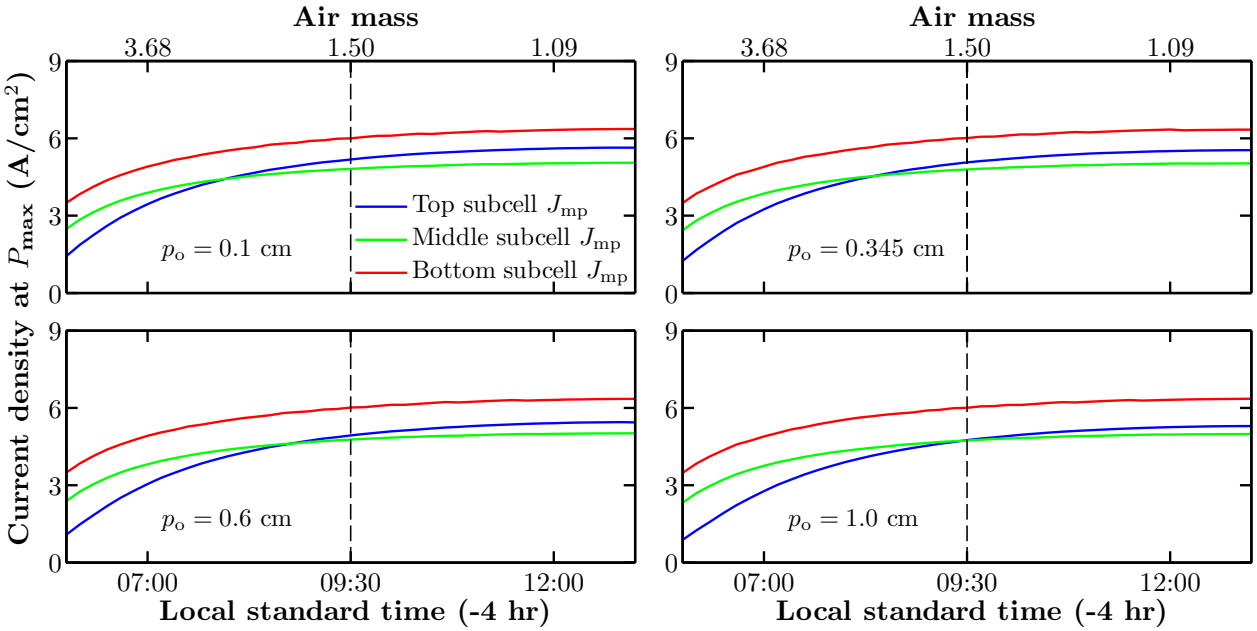

Figure 4.21: Subcell currents at the maximum power point for different ozone absorption cases. High ozone content reduces the short circuit current of the top subcell, and worsens subcell current matching.

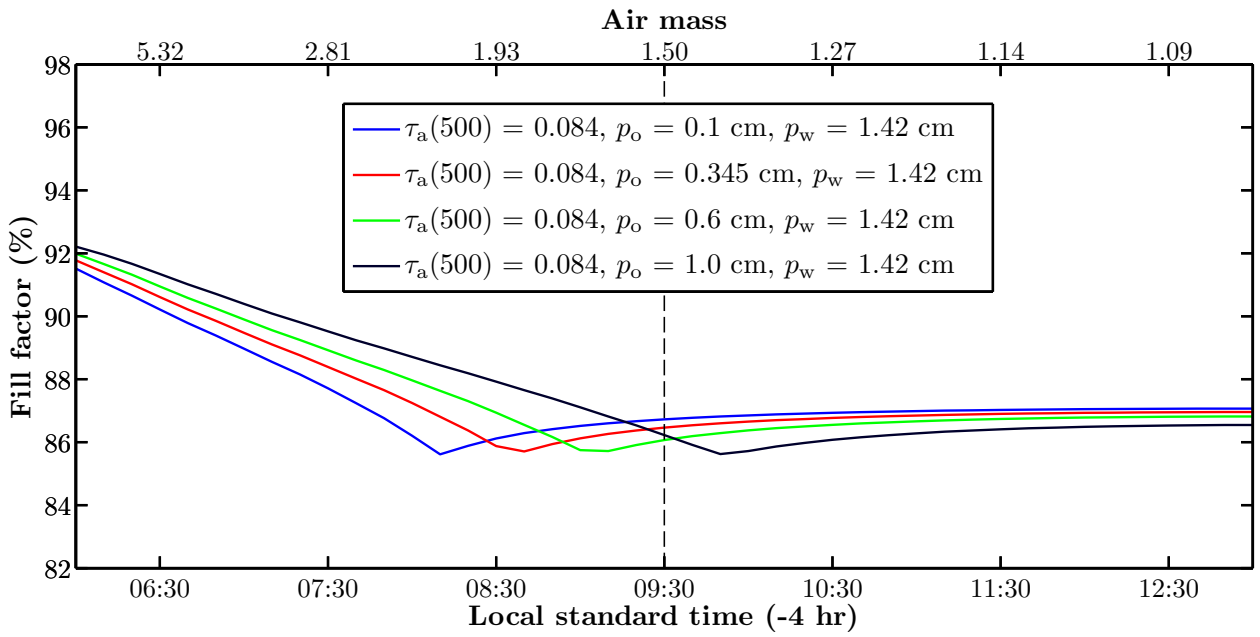

Figure 4.22: The FF of the TJSC under different ozone absorptions. The lowest FF corresponds to the highest efficiency throughout the day, as it represents the point where the best subcell current matching occurs. For higher ozone absorption this point occurs later in the day.

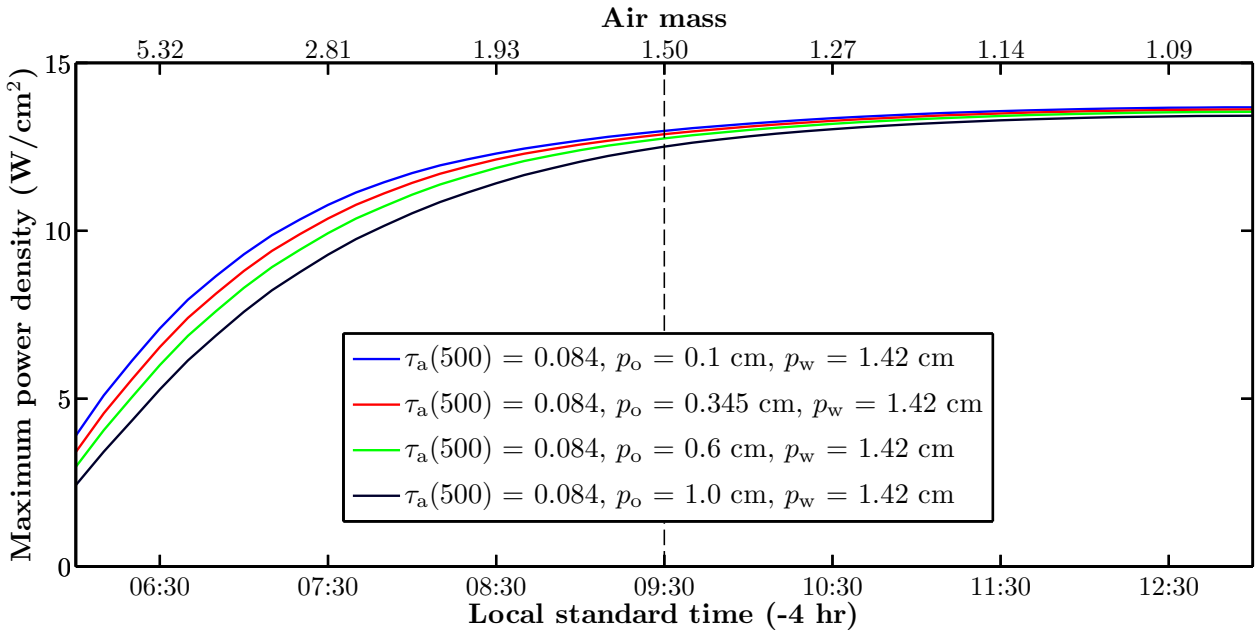

Figure 4.23: The output power of the TJSC under varying ozone content. High ozone absorption decreases cell's output power.

Water vapour absorption effect

Figure 4.24 shows the TJSC's efficiency throughout the day for different water absorption cases. In contrast to aerosol extinction and ozone absorption scenarios, the peak efficiency occurs under high water vapour conditions. Figure 4.25 reveals that the J_{mp} for all subcells are best matched at the water vapour path-length of 4.0 cm. This is primarily due to the reduction of the J_{mp} for the overproducing bottom subcell, which improves its FF and efficiency. The water vapour absorption primarily affects the J_{sc} of the bottom subcell, but it also has a slight influence on the J_{sc} of the middle subcell. On the other hand, the top subcell is largely unaffected, as demonstrated in Figure 4.25. Therefore, as the water vapour content increases, the J_{mp} of the middle and bottom subcells approaches the J_{mp} of the top subcell. As in previous cases, the best current match occurs when the FF is the lowest, which, based on Figure 4.26, occurs earlier in the day for high water vapour absorption. Nonetheless, the low water vapour content is still desirable, because it yields the most power from the TJSC, as demonstrated in Figure 4.27. However, for the AM higher than 2.81 the TJSC's output power is largely unaffected by the water vapour content in the atmosphere, due to the increased efficiency of the TJSC under these conditions.

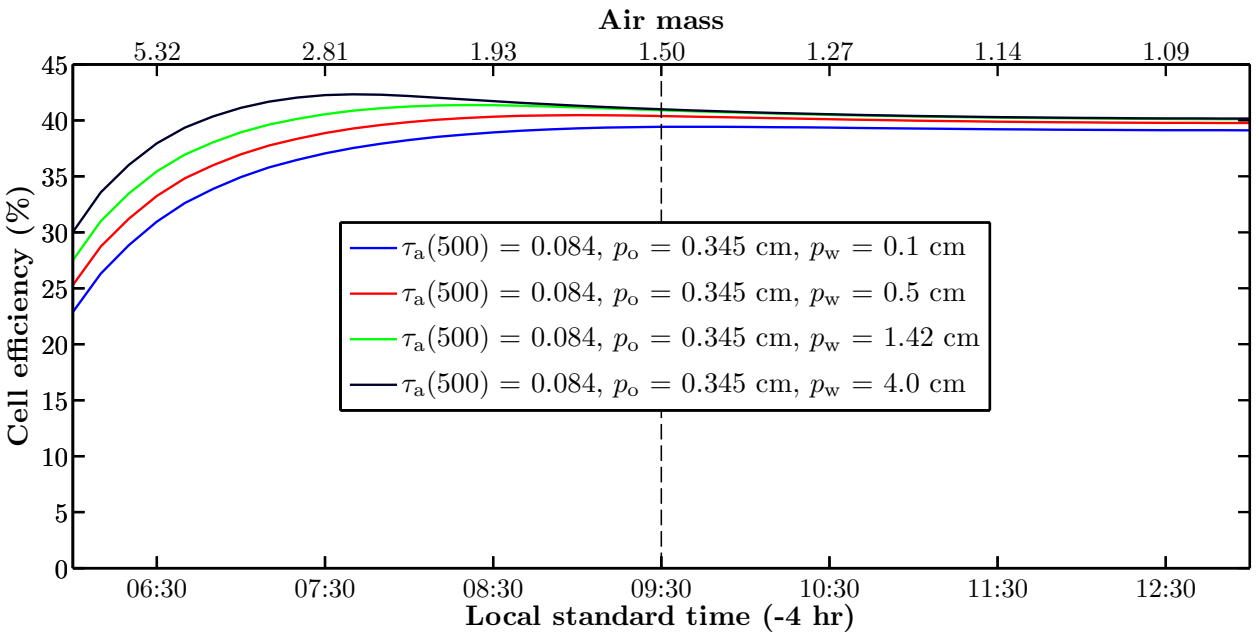

Figure 4.24: The effect of water vapour absorption on the TJSC's efficiency. High water vapour content increases cell efficiency for all AMs.

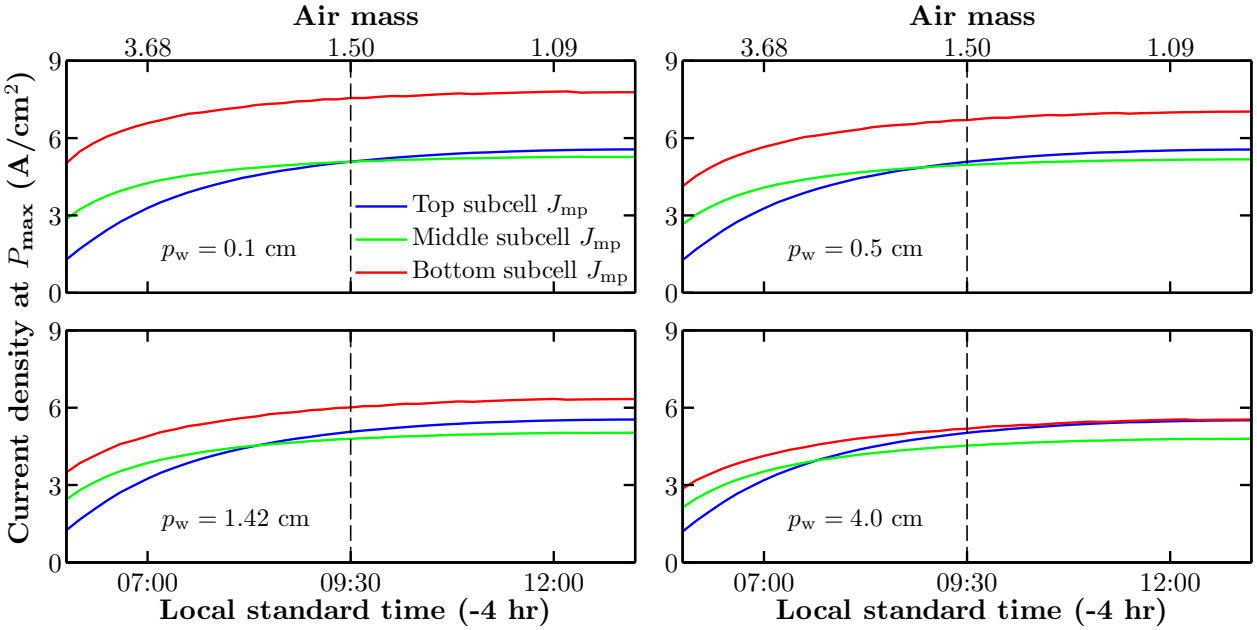

Figure 4.25: Subcell currents at the maximum power point for different water absorption cases. High water vapour content reduces the current of the middle and bottom subcells, thus leading to a better current matching.

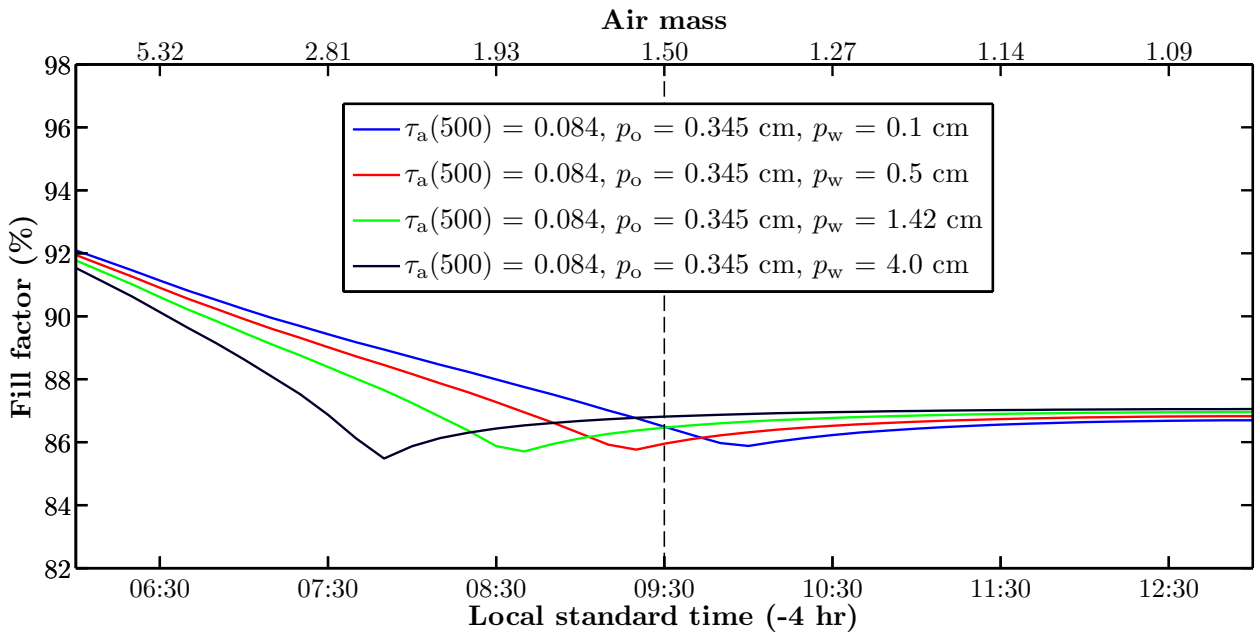

Figure 4.26: The FF of the TJSC under different water vapour absorptions. The lowest FF corresponds to the highest efficiency throughout the day, as it represents the point where the best subcell current matching occurs. For higher water vapour absorption this point occurs earlier in the day.

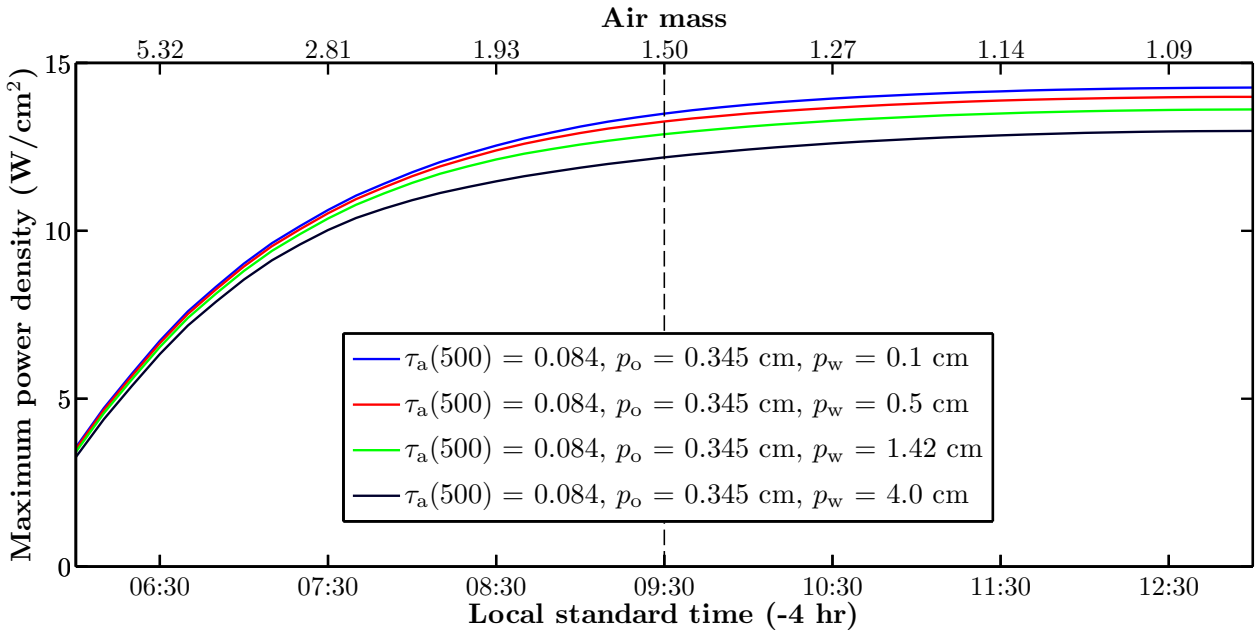

Figure 4.27: The output power of the TJSC under varying water vapour content. High water vapour absorption decreases cell's output power, but for the AM higher than 2.81 this effect is very small.

References

[1] N. Chan, H. E. Brindley, and N. J. Ekins-Daukes. "Quantifying the impact of individual atmospheric parameters on CPV system power and energy yield". In: *Photovoltaic Specialists Conference (PVSC), 2012 38th IEEE*. IEEE. 2012, pp. 000922–000927.

[2] N. Chan, T. Young, H. Brindley, et al. "Validation of energy prediction method for a concentrator photovoltaic module in Toyohashi Japan". In: *Progress in Photovoltaics: Research and Applications* (2012).

[3] J. Jaus and C. A. Gueymard. "Generalized spectral performance evaluation of multi-junction solar cells using a multicore, parallelized version of SMARTS". In: *AIP Conference Proceedings*. Vol. 1477. 2012, p. 122.

[4] N. Chan, T. Young, H. Brindley, et al. "Variation in spectral irradiance and the consequences for multi-junction concentrator photovoltaic systems". In: *Photovoltaic Specialists Conference (PVSC), 2010 35th IEEE*. IEEE. 2010, pp. 003008–003012.

[5] M. Muller, B. Marion, S. Kurtz, et al. "An investigation into spectral parameters as they impact CPV module performance". In: *AIP Conference Proceedings*. Vol. 1277. 2010, p. 307.

[6] C. A. Gueymard. "Daily spectral effects on concentrating PV solar cells as affected by realistic aerosol optical depth and other atmospheric conditions". In: *SPIE Solar Energy and Technology*. International Society for Optics and Photonics. 2009, pp. 741007–741007.

[7] T. Minemoto, S. Nagae, and H. Takakura. "Impact of spectral irradiance distribution and temperature on the outdoor performance of amorphous Si photovoltaic modules". In: *Solar energy materials and solar cells* 91.10 (2007), pp. 919–923.

[8] R. Gottschalg, D. Infield, and M. Kearney. "Experimental study of variations of the solar spectrum of relevance to thin film solar cells". In: *Solar energynergy materials and solar cells* 79.4 (2003), pp. 527–537.

[9] M. Gonzalez and J. Carrol. "Solar cells efficiency variations with varying atmospheric conditions". In: *Solar Energy* 53.5 (1994), pp. 395–402.

[10] R. King, D. Bhusari, D. Larrabee, et al. "Solar cell generations over 40% efficiency". In: *Progress in Photovoltaics: Research and Applications* 20 (2012), pp. 801–815.

[11] W. McMathon, S. Kurtz, K. Emery, et al. *Criteria for the design of GalnP/GaAs/Ge triple junction cells to optimize their performance outdoors*. Tech. rep. National Renewable Energy Laboratory, 2002.

[12] O. Al Taher, R. Cravens, P. Pien, et al. "Qualification testing of 40% metamorphic CPV solar cells". In: *Photovoltaic Specialists Conference (PVSC), 2010 35th IEEE*. IEEE. 2010, pp. 1995–1998.

[13] M. Gilbert. *Renewable and efficient electric power systems*. John Wiley & Sons, 2004.

[14] M. A. Green, K. Emery, Y. Hishikawa, et al. "Solar cell efficiency tables (version 41)". In: *Progress in photovoltaics: research and applications* 21.1 (2013), pp. 1–11.

[15] W. Shockley and H. J. Queisser. "Detailed balance limit of efficiency of p-n junction solar cells". In: *Journal of applied physics* 32.3 (1961), pp. 510–519.

[16] J. Nelson. *The physics of solar cells*. Vol. 57. World Scientific, 2003.

[17] L. M. Fraas and L. D. Partain. *Solar cells and their applications*. Vol. 236. John Wiley & Sons, 2010.

[18] K. Misiakos and D. Tsamakis. "Accurate measurements of the silicon intrinsic carrier density from 78 to 340 K". In: *Journal of applied physics* 74.5 (1993), pp. 3293–3297.

[19] S. R. Wenham and M. A. Green. *Applied photovoltaics*. Routledge, 2011.

[20] G. Cherucheril, S. March, and A. Verma. *Multijunction solar cells*. Tech. rep. Iowa State University, 2011.

[21] Y. Sakurada, Y. Ota, and K. Nishioka. "Simulation of temperature characteristics of InGaP/InGaAs/Ge triple-junction solar cell under concentrated light". In: *Japanese Journal of Applied Physics* 50.4 (2011), 04DP13.

[22] M. Yandt. "Characterization and performance analysis of high efficiency solar cells and concentrating photovoltaic systems". MA thesis. University of Ottawa, 2012.

[23] Y. Varshni. "Temperature dependence of the energy gap in semiconductors". In: *Physica* 34.1 (1967), pp. 149–154.

[24] K. Nishioka, T. Takamoto, T. Agui, et al. "Evaluation of InGaP/InGaAs/Ge triple-junction solar cell and optimization of solar cell's structure focusing on series resistance for high-efficiency concentrator photovoltaic systems". In: *Solar energy materials and solar cells* 90.9 (2006), pp. 1308–1321.

[25] J. Ermer, R. Jones, P. Hebert, et al. "Status of C3MJ+ and C4MJ production concentrator solar cells at spectrolab". In: *Photovoltaics, IEEE Journal of* 2.2 (2012), pp. 209–213.

Chapter 5

Solar spectral irradiance meter

The integral part of most CPV systems is a MJSC. A MJSC consists of series-connected subcells, so the lowest current-generating one limits the performance of the full device. For optimal operation MJSC subcells are designed to be current matched for a particular spectrum, such as for the AM1.5D from the reference ASTM G173 [1, 2]. However, the solar irradiance at ground level is a dynamic energy resource that fluctuates in intensity and spectrum due to varying geographical and meteorological conditions. Therefore, under field conditions spectral variations cause MJSCs and CPV system performances to deviate from a perfect current match [3, 4]. Hence, knowledge of the solar spectral irradiance at a particular installation site is a valuable asset that gives a better predictive insight into the functioning of the CPV system.

The most accurate way to obtain the solar spectra in a desired location is to perform direct outdoor measurements with a FSR. However, these measurements are rarely available due to the prohibitive cost of the instrument. Therefore, the SSIM prototype was designed at the University of Ottawa as a cost-effective alternative to a FSR. The SSIM measures the solar spectral irradiance in several narrow wavelength bands with a combination of inexpensive Si photodiodes and integrated bandpass interference filters. Furthermore, the ambient temperature and pressure is recorded by the SSIM. This device performs in field spectral measurements with a cost two orders of magnitude less than a FSR, however additional software post-processing is required to deduce the solar spectrum for the entire 280–4000 nm range. The model developed in Chapter 3 along with the inputs from the SSIM is used to approximate the solar spectrum, while resolving major atmospheric processes, such as air mass, Rayleigh scattering, aerosol extinction, ozone and water vapour absorptions.

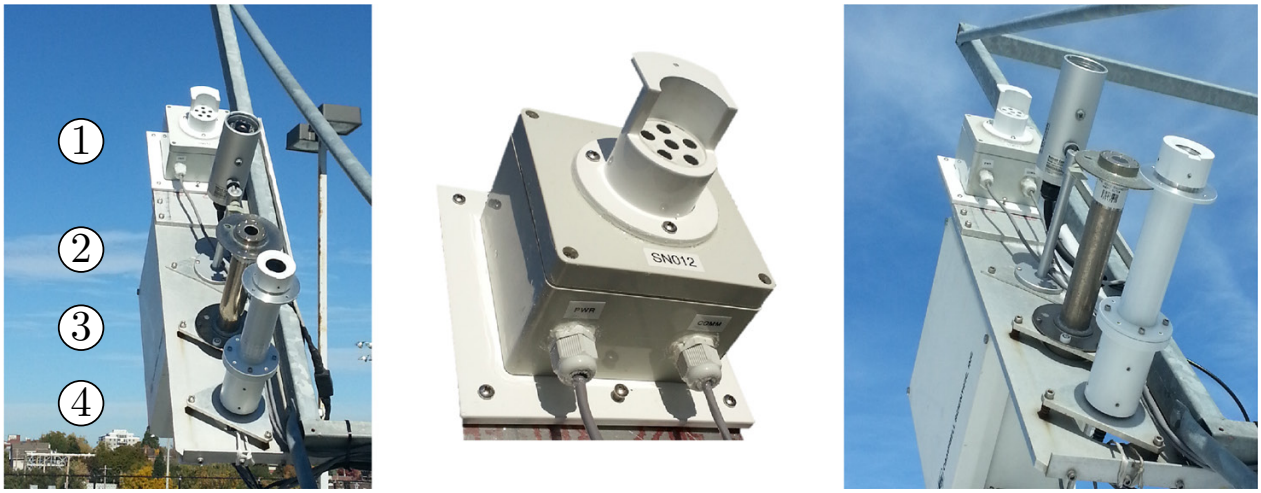

Figure 5.1: The instrumentation on the Golden Sun dual-axis tracker at the University of Ottawa's CPV testing facility, consisting of the SSIM ①, the sky camera ②, the Eppley pyrheliometer ③ and the ASD spectroradiometer ④.

5.1 Solar test site overview

The University of Ottawa's CPV solar testing facility was set up in early 2011, containing key instrumentation for the long term evaluation of the solar resource, such as the spectroradiometer, the pyrheliometer, and the dual-axis solar trackers, as shown in Figure 5.1. The specifications of the aforementioned and other instruments at the test site are summarized in Table 5.1. All measurements are acquired at two min intervals and are stored in a relational

Table 5.1: The instrumentation at the University of Ottawa's CPV testing facility.

Instrument	Manufacturer	Specifications
Spectroradiometer	*ASD Inc.*	350–1830 nm, 3 nm resolution, 2.9° field of view
Pyrheliometer	*Eppley Lab. Inc.*	285–2800 nm, ISO secondary standard, 2.9° field of view
Pyranometer	*Eppley Lab. Inc.*	285–2800 nm, ISO secondary standard
Weather station	*Lufft*	Measures ambient pressure, temperature, humidity, wind speed, wind direction, and global horizontal irradiance (300–1100 nm)
Solar tracker	*Golden Sun*	dual axis, 0.2° tracking accuracy

database for subsequent data analysis. The spectral data from the spectroradiometer is the most important piece of information when analyzing the performance of the SSIM, as the spectral output of both devices can be compared directly. The pyrheliometer measurements are used to validate the absolute power from both the SSIM and the ASD spectroradiometer. The measurements from the Lufft weather station are utilized for ambient pressure and temperature comparison with the SSIM.

5.2 Baseline instrumentation performance

To ensure an accurate assessment of the SSIM's performance, two baseline instruments at the test site, the spectroradiometer and the pyrheliometer, were tested against each other to ensure the similarity in reported DNI. The first step was to validate that both instruments have a comparable field of view. The original collimation tube design of the ASD spectroradiometer had a 0.7° field of view, as demonstrated in Figure 5.2a. This is well below the field of views of 2.5° and 2.9° for the DNI instrumentation as recommended by the World Meteorological Organization and the Eppley pyrheliometer, respectively [5]. Therefore, the collimation tube for the ASD spectroradiometer was redesigned to match the field of view of the pyrheliometer, as shown in Figure 5.2b.

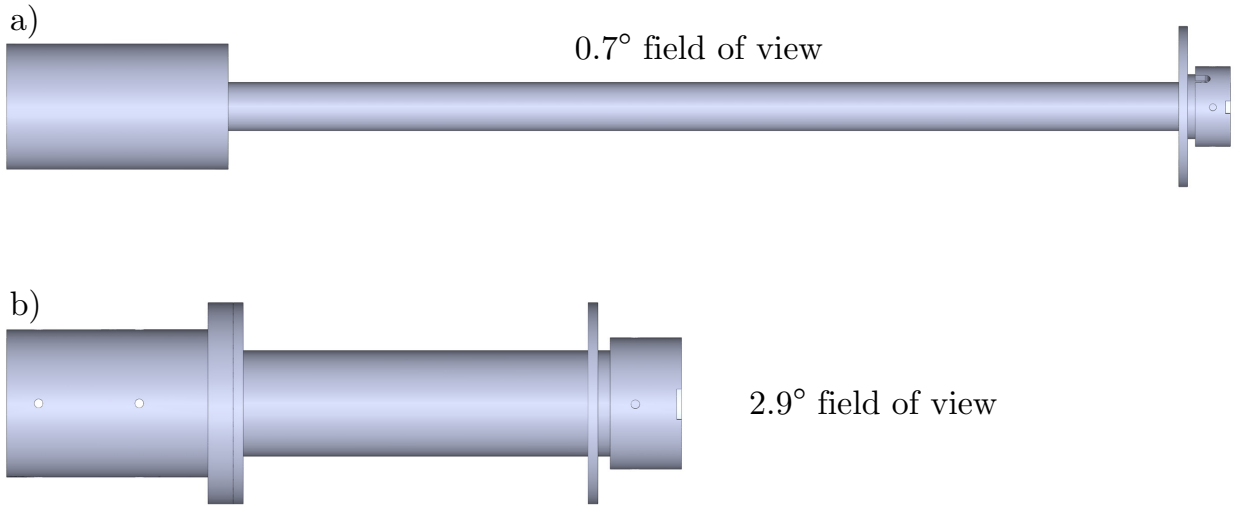

Figure 5.2: The comparison of the original a) and the redesigned b) collimation tubes for the ASD spectroradiometer. The new design decreased the overall length and increased the front aperture radius to match the 2.9° field of view the Eppley pyrheliometer.

The redesigned version of the spectroradiometer's collimation tube was installed on June 19th, 2013. From this date and on the DNI from the ASD spectroradiometer and the Eppley pyrheliometer can be directly compared as both instruments have an identical field of view. However, the solar spectrum from the spectroradiometer must be extended in order to match the spectral range of the pyrheliometer. The reconstruction technique from Chapter 3 is used to approximate the measured solar spectrum from the spectroradiometer in the 350–1830 nm range. The modelled spectrum is then extended to the pyrheliometer's 285–2800 nm range. Figure 5.3 shows a four-month DNI comparison from the spectroradiometer and the pyrheliometer in the 285–2800 nm range. The data was filtered to eliminate the DNI below 500 W/m^2 and the intermittent cloudy periods for clearer visualization. Figure 5.3 demonstrates that both instruments were in good agreement up to July 10th, 2013, from when the ASD spectroradiometer began underreporting the DNI. The gradual decline in spectroradiometer's performance stabilized at the end of September, when the difference in

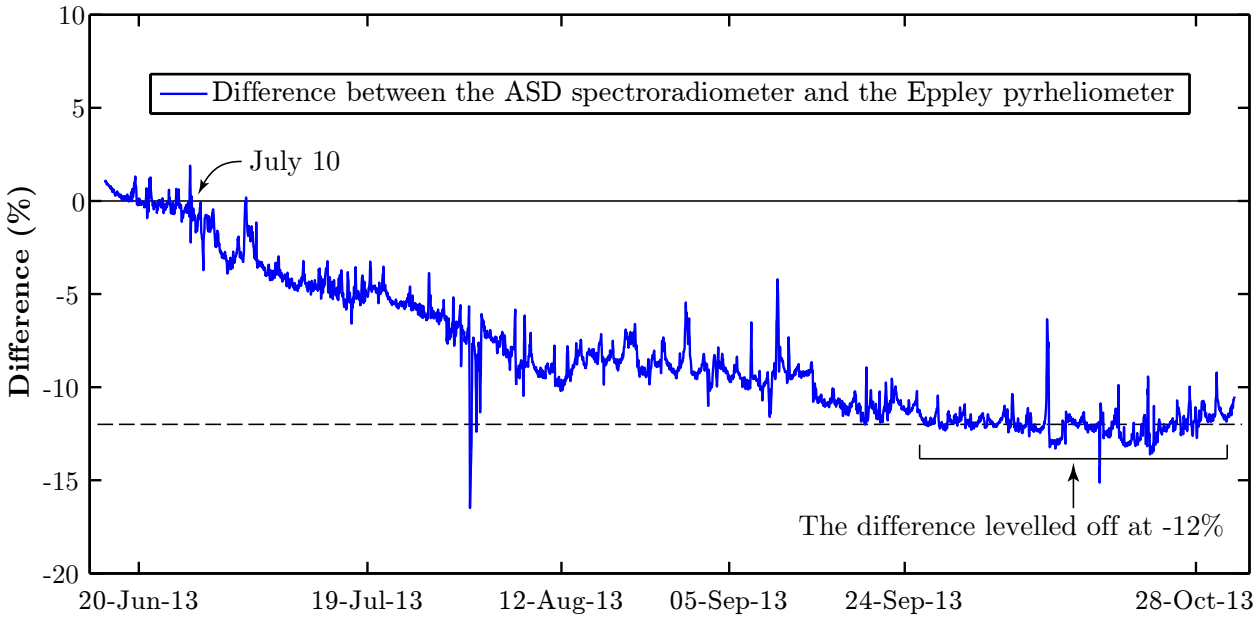

Figure 5.3: The comparison of the DNI as reported by the ASD spectroradiometer with a redesigned collimation tube from Figure 5.2b and the Eppley pyrheliometer. The ASD spectroradiometer's measured solar spectrum was extended from 350–1830 nm to 285–2800 nm using the modelling method described in Chapter 3 to match the spectral range of the Eppley pyrheliometer for an evenhanded analysis. Evidently, the performance of the ASD spectroradiometer has gradually deteriorated from July 10th, 2013, but the difference between two instruments stabilized at around -12% at the end of October, 2013.

the DNI between the ASD spectroradiometer and the Eppley pyrheliometer remained at -12% from there on. At the end of November the ASD spectroradiometer was brought indoors for an assessment.

To evaluate the spectral accuracy of the outdoor ASD spectroradiometer, the instrument was compared against the reference ASD spectroradiometer, which will be referred to from now on as the indoor ASD spectroradiometer. The spectral comparison between the outdoor and the indoor ASD spectroradiometers was performed under a quartz tungsten halogen light source. The experiment consisted of measuring the responses of bare optical fibre and the remote cosine receptor (RCR) for each spectroradiometer. The RCR is an aluminum cylinder with a top-mounted polyoxymethylene puck, which couples the light into the optical fibre. Figure 5.4 demonstrates the difference in the bare fibre and the RCR responses between both spectroradiometers. Evidently, the RCR response of the outdoor ASD spectroradiometer deviates significantly from the indoor one, while the bare fibre responses agree reasonably well in the 350–1100 nm range. The RCR's transmission of the outdoor

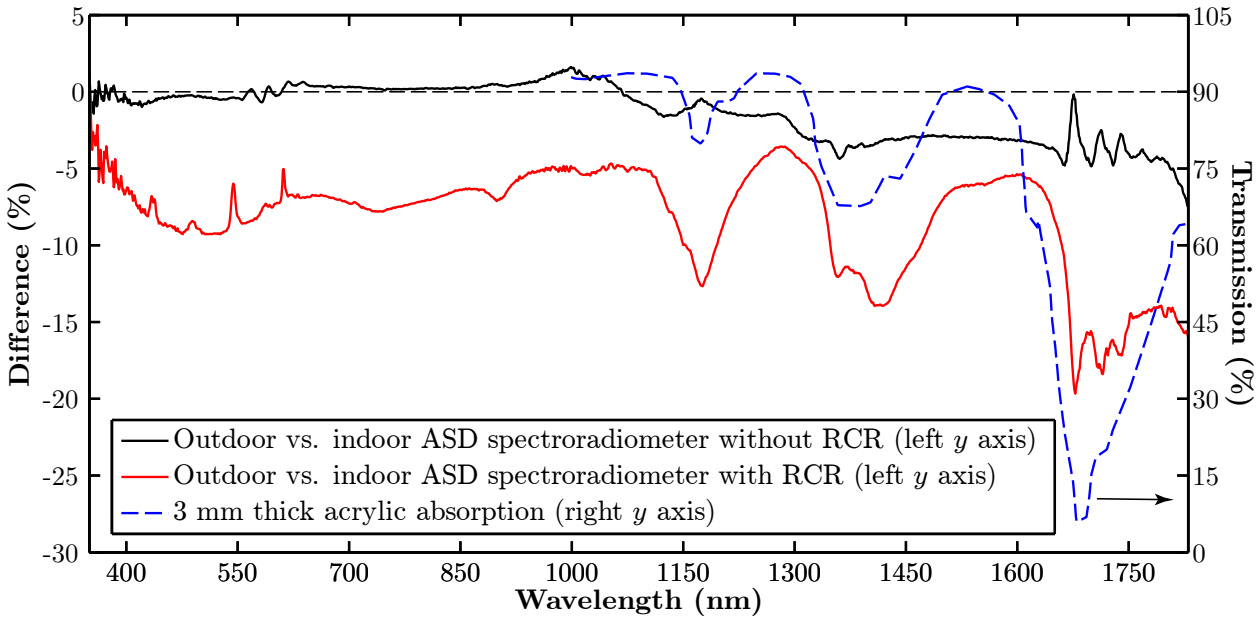

Figure 5.4: The difference in responses of the bare fibre (without RCR) and the RCR for the outdoor and the indoor ASD spectroradiometers. The bare fibre responses agree reasonably well between both instruments, albeit there is a slight IR discrepancy for the indoor spectroradiometer. However, the RCR responses show a significant degradation of the outdoor RCR, which explains the reduced DNI reported by the outdoor ASD spectroradiometer. This degradation is similar to the acrylic's IR transmission profile.

ASD spectroradiometer has degraded as apparent by significant IR absorption, which resembles the acrylic's transmission profile, as shown in Figure 5.4. These results validate the underreporting of the DNI by the indoor ASD spectroradiometer as compared to the Eppley pyrheliometer in Figure 5.3. The data in Figure 5.4 is used to quantify the spectral calibration factor needed to scale the outdoor ASD spectroradiometer's measured solar spectrum for accurate representation when analyzing the SSIM's performance.

5.3 SSIM overview

The exploded view of the SSIM prototype is presented Figure 5.5. The SSIM's components can be divided into two categories: opto-mechanical and electrical. The quartz window, the collimation tube, the integrated photodiode-filter combinations, the enclosure, and the alignment plate are all part of the opto-mechanical design. On the other hand, the main and the daughter printed circuit boards (PCBs) are part of the electrical design.

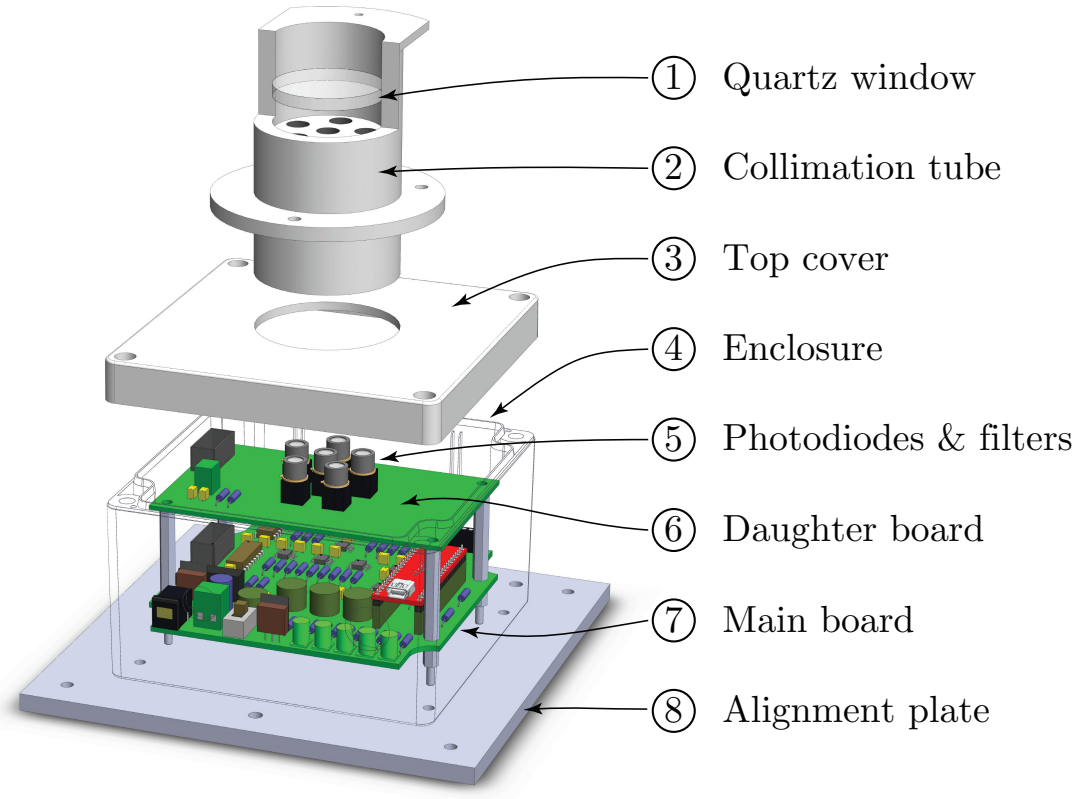

Figure 5.5: The exploded of view of the SSIM prototype. The SSIM design primarily falls under the opto-mechanical and the electrical categories.

Table 5.2 lists the components from Figure 5.5 with their respective manufacturers and basic functions. The first component in the optical train of the SSIM is a 4 mm thick quartz window, which acts as a protective barrier against the moisture and dust ingress. It has an average transmission of ∼95% in the 350–1830 nm range. The quartz window rests on the top of the collimation tube and is sealed using a standard silicone. The collimation tube and the quartz window assembly is fastened to the top cover of the enclosure with three screws and it rests on the daughter board. This setup allows to optically isolate each photodiode-filter combination (channel) by exposing it to a field of view as defined by the geometry of the collimation tube. The final component of the optical train is the photodiode-filter channels, which generate electrical current proportional to incident spectral irradiance as limited by the bandpass filter's narrow pass band. The photodiode-filter combinations are mounted on the daughter board and are electrically connected to the signal conditioning circuitry of the main board. The latter passes the data from each channel to the external host for analysis on the personal computer. Both the opto-mechanical and the electric designs are described in more detail in the subsequent sections.

Table 5.2: List of main components in the SSIM and their basic functions.

Component	**Manufacturer**	**Function**
Quartz window	*Thorlabs Inc.*	Protection against moisture and debris ingress
Collimation tube*	*Axzeon Inc.*	Geometric field of view limitation for each photodiode-filter combination
Enclosure	*Hammond MFG*	Encloses the electrical and the mechanical components of the SSIM
Photodiode-filter	*Intor Inc.*	Senses the solar spectral irradiance in a narrow wavelength band
Daughter PCB*	*Sunstone Circuits*	Hosts the photodiode-filter combinations
Main PCB*	*Sunstone Circuits*	Acquires the signals from the photodiode-filter combinations and relays the data to the host
Alignment plate*	*Axzeon Inc.*	Allows to optimally align the SSIM to the sun

*custom-designed

5.4 Opto-mechanical design of the SSIM

5.4.1 Collimation tube

The geometry of the collimation tube limits the DNI for each channel to a 2.9° field of view to be consistent with the ASD spectroradiometer and the Eppley pyrheliometer. The collimation tube is fastened to the top cover of the enclosure via three mounting holes, as shown in Figure 5.6a. Its bottom surface rests on the daughter board, thus optically isolating each photodiode-filter combination from each other. The latter are situated in the centre of each of the six hollow cylinders that define the field of view, as demonstrated from a sectioned view in Figure 5.6b. The positioning of the SSIM with respect to the sun is optimized by the alignment pinhole. Furthermore, to minimize the exposure to a stray light, the collimation tube was black anodized and the exterior surfaces were painted with white UV resistant paint. Finally, each channel is sealed via the quartz window to prevent moisture and debris ingress.

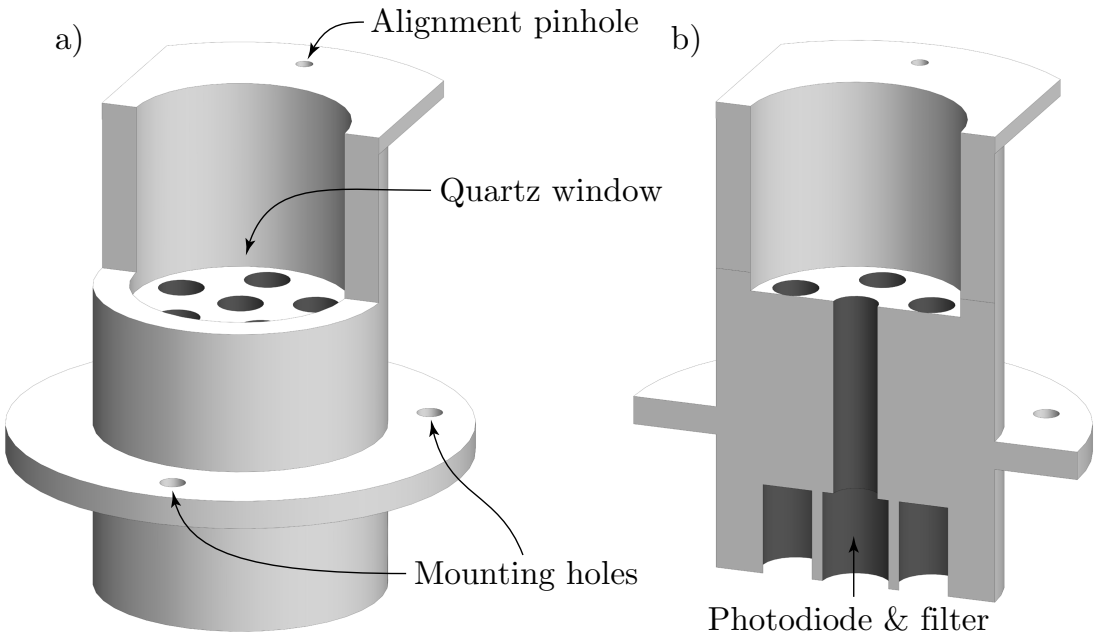

Figure 5.6: The normal a) and the sectioned b) views of the collimation tube of the SSIM. The primary function of this component is to expose each channel to the DNI within a 2.9° field of view. Its other functionalities include the sun alignment optimization, and the protection from moisture and debris ingress with the quartz window.

5.4.2 Photodiode-filter combinations

Each channel of the SSIM consists of the photodiode with an integrated bandpass filter. There are in total six channels centred at 420, 500, 610, 780, 940, and 1030 nm. The responsivity of each channel was measured at the University of Ottawa using the Oriel IQE-200 system. This system is equipped with a temperature controlled stage, which allows evaluating the performance of each photodiode-filter combination at various temperatures. The custom aluminum photodiode holder was designed to facilitate the mounting and to allow a more accurate temperature control of the device under test, as shown in Figure 5.7. The temperature of the photodiode inside the photodiode holder differs from the setpoint of the temperature stage due to inherent heat transfer losses between the stage and the holder. Therefore, the external thermocouple is inserted into the mounting body via a thermocouple slot, such that the contact with the photodiode is made, as demonstrated in Figure 5.7. This setup along with a multimeter allows to accurately set and monitor the temperature of the photodiode at which the responsivity needs to be measured. Finally, the connection slot is used to connect the anode and the cathode of the photodiode under test to the input terminals of the EQE machine via the hook probes.

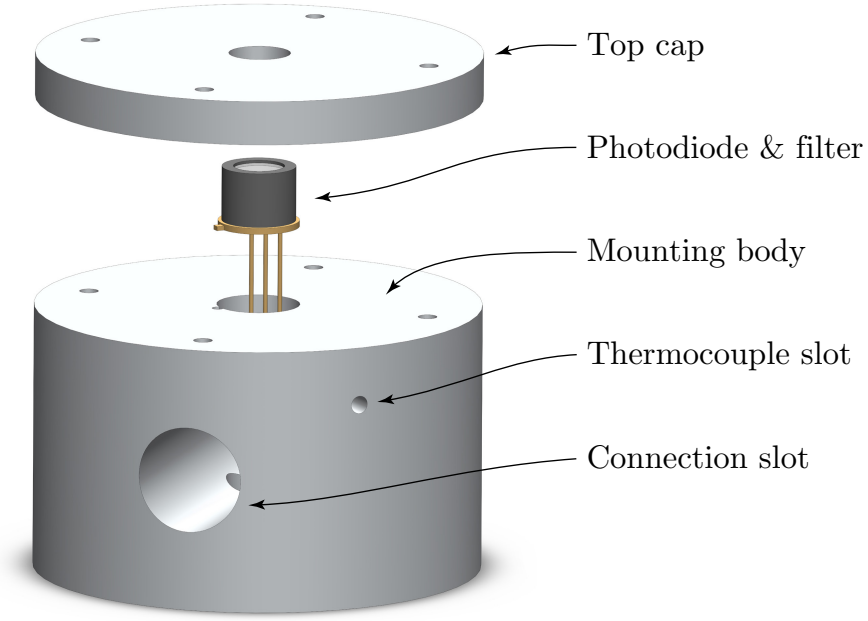

Figure 5.7: The photodiode holder for the responsivity measurement of the photodiode-filter combination. This custom-made test jig provides a reliable way for mounting, securing the electrical connection, and setting the temperature of the photodiode under test.

The measurement of the responsivities for all channels at 25°C is shown in Figure 5.8. These measurements are repeated at 45 and 65°C to deduce the temperature coefficient for each channel. The channels closest to the bandgap wavelength of the Si photodiode experience the greatest dependence on temperature. For example, the maximum responsivity of the 1030 nm channel increases by 13% from 25 to 65°C, while for 420 nm channel it decreases by only 0.6% under the same temperature conditions. The angle of light incidence is another factor besides temperature influencing the responsivity of each channel.

An inclinometer in conjunction with a tilt platform and the photodiode holder was used to perform the angle of incidence sensitivity analysis on a sample 870 nm photodiode-filter combination. The manufacturer of the filters recommends the operation under near collimated light source; therefore, it was of interest to determine if the responsivity of the channels would be affected by a field of view as defined by the collimation tube. Figure 5.9 shows the changes of the responsivity for varying angle of incidence about one axis from 0 to 11°. The centre wavelength blue-shifts, while the maximum responsivity slightly decreases with increasing angle of incidence. These results validate that a 2.9° field of view of the collimation tube does not significantly affect the channel performance.

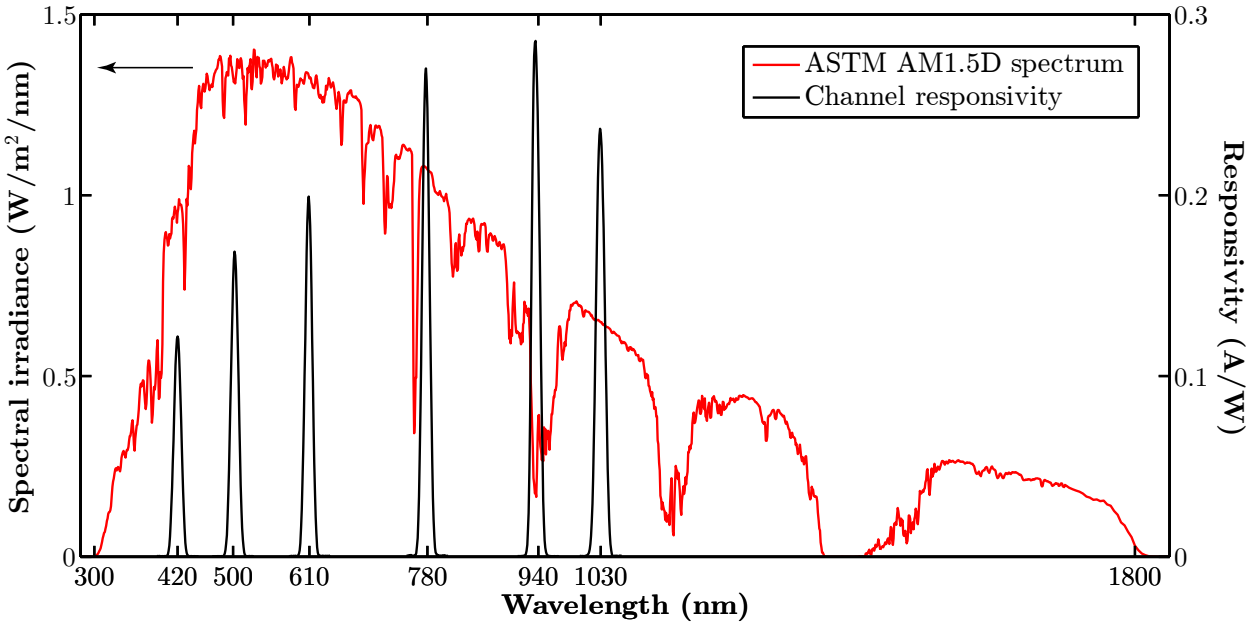

Figure 5.8: The responsivity of the SSIM's channels measured at 25°C using the Oriel IQE-200 system. The AM1.5D spectrum gives a good visualization of the strategic spectral placement of the channels.

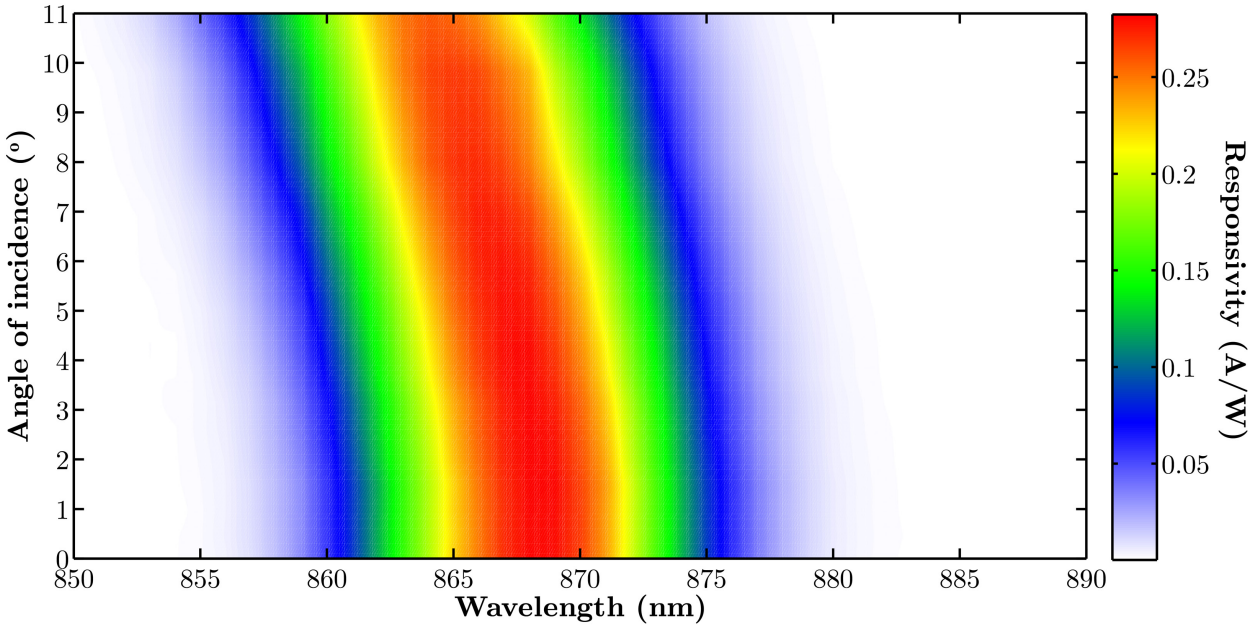

Figure 5.9: The change in the responsivity of a sample 870 nm photodiode-filter combination under varying angle of incidence about one axis from 0 to 11°. The centre wavelength and the corresponding responsivity decrease with the increasing angle of incidence. However, these changes are very subtle for the SSIM's field of view of 2.9°.

5.5 Electrical design of the SSIM

The SSIM's electrical design consists of two custom-made PCBs: the main board and the daughter board. Their primary function is to accurately measure the current from each spectral channel and to relay that information to the external host for analysis. The high-level electrical block diagram to accomplish this task is presented in Figure 5.10. Six spectral sensors and one calibration channel are fed to a 8-to-1 multiplexer, where a single channel is selectively passed on to a dynamic amplifier stage for signal conditioning. The resultant output voltage is processed by a 22-bit analog to digital converter (ADC), which transmits this data to a microcontroller (MCU) via a serial peripheral interface. Furthermore, the ambient pressure and temperature sensor outputs are fed to the MCU. Finally, the MCU communicates with a host through a RS-485 protocol.

5.5.1 Calibration stage

The calibration stage was implemented to validate the long term operation of the electronics. It consists of an inverting operational amplifier with a biased inverting input at 1 V as

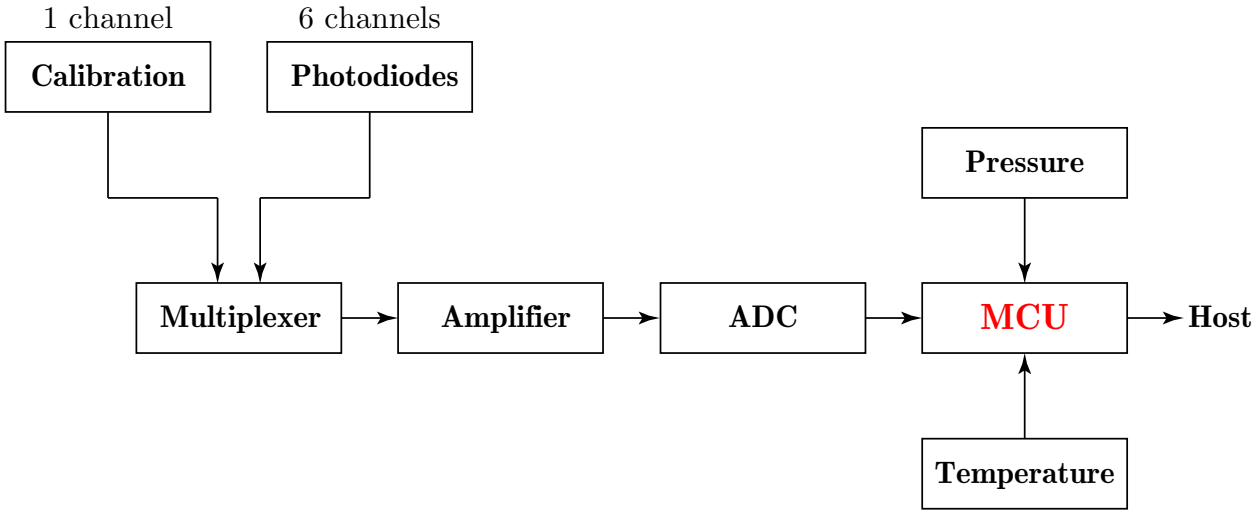

Figure 5.10: A high-level electrical block diagram of the SSIM.

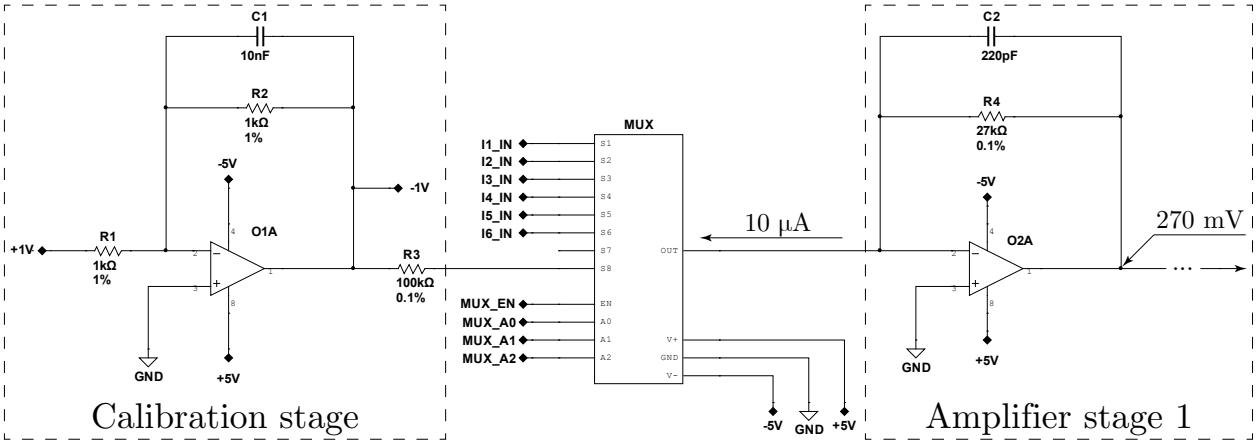

Figure 5.11: A snapshot of the calibration stage circuit. It generates a 10 µA current to test the electronics for consistency.

demonstrated in Figure 5.11. When the calibration channel is activated by the multiplexer, a 1 V potential develops across the resistor R3, which results in 10 µA current drawn from the first amplifier stage. This setup simulates the generated current from a photodiode. If the circuitry is functioning correctly, the host should always read 10 µA from the calibration channel.

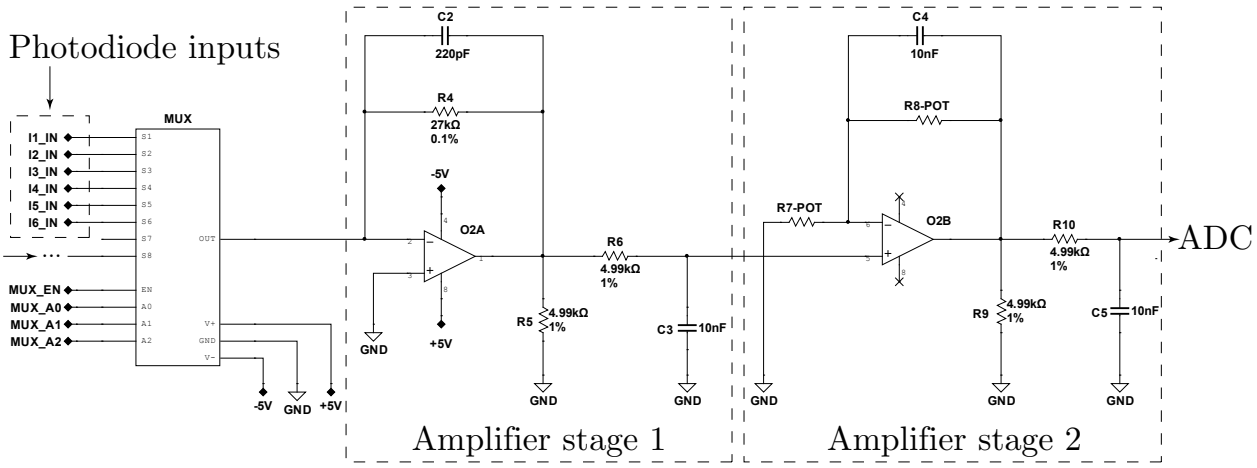

Figure 5.12: The signal conditioning circuit of the SSIM. It consists of the transimpedance stage (amplifier stage 1) and dynamic amplifier stage (amplifier stage 2). This circuit allows to measure the photodiode current of up to 90.7 μA.

5.5.2 Photodiode current measurement

The accurate measurement of the photodiodes' currents is the critical task for the electronics of the SSIM. Figure 5.12 shows the circuit that converts the current from each photodiode to a voltage and then passes it on to the ADC. The conversion is accomplished in two stages. The first stage is a transimpedance amplifier with a gain of 27,000 as dictated by resistor R4. The second stage is a non-inverting amplifier with a variable gain as controlled by a digital potentiometer. The MCU monitors the output voltage from the ADC and adjusts the resistors R7-POT and R8-POT to maximize the signal, thus increasing the signal-to-noise ratio. The digital potentiometer allows to control the gain of the second amplifier stage from 2 to 10. This configuration permits a wider current range input from the photodiodes. The maximum current that the circuit in Figure 5.12 can sense is 90.7 μA assuming the maximum voltage output of 4.9 V from the second amplifier stage as limited by ±5 V power supply of the operational amplifiers.

5.5.3 Sources of the measurement errors

Inherent errors

To determine the accuracy of the photodiode's current measurement by the electric circuit of the SSIM, it is important to quantify the sources of measurement errors. The current flowing through any resistor gives rise to shot and Johnson noises. Johnson or thermal noise current,

I_{n1}, arises from the thermal generation of the carriers and can be expressed as [6]

$$I_{n1} = \sqrt{\frac{4k \cdot T \cdot \Delta f}{R}}, \tag{5.1}$$

where k is Boltzmann constant (J/K), T is the temperature of the resistor (K), Δf is the noise bandwidth (Hz), and R is the sample resistance (Ω). The photodiode's shunt resistance primarily contributes to Johnson current noise. The SSIM's photodiodes typically have 3500 MΩ shunt resistance, which assuming 1 MHz noise bandwidth and the ambient temperature of 85°C results in Johnson noise of 2.37 pA as per Equation 5.1 or equivalently a voltage noise of $\pm$63.99 nV at the output of the amplifier stage 1 in Figure 5.12. Johnson noise from the feedback resistor, R4, of the amplifier stage 1 has the highest impact on the measurement uncertainty with the voltage noise of $\pm$23.11 μV or $\pm$0.0086% variation for the photodiode current of 10 μA. As the output voltage of the amplifier stage 1 decreases, the measurement uncertainty increases due to Johnson noise from the feedback resistor, R4.

Shot noise is another source of the measurement error in the SSIM's electric circuit. It occurs due to the finiteness of the electrical charges, which do not flow in a smooth but rather discrete manner. The expression for shot noise, I_{n2}, is given by [6]

$$I_{n2} = \sqrt{2q \cdot I_{dc} \cdot \Delta f}, \tag{5.2}$$

where q is the electron charge (C), I_{dc} is the direct current (A), and Δf is the noise bandwidth (Hz). For the base case of 10 μA photodiode current with 1 MHz noise bandwidth, shot noise across resistor R4 of $\pm$48.33 μV or $\pm$0.018% variation develops at the output of the amplifier stage 1.

Instrumentation errors

Instrumentation errors arise from various parasitic effects of the integrated circuit chips in the SSIM's electronics, including the operational amplifiers, the digital potentiometer and the multiplexer. For the SSIM application, two design constraints of the operational amplifiers must be considered: the bias current and the input offset voltage. A bias current is a leakage current into the input terminals of an operational amplifier, ranging from fA to μA. In the case of the SSIM the maximum bias current is 40 pA, which corresponds to a voltage offset of 1.08 μV or 0.0004% at the output of the amplifier stage 1 for 10 μA photodiode current. Evidently, this bias current is very low and hence its impact on the circuit accuracy is negligible. Input offset voltage is another characteristic of the operational amplifiers affecting the measurement uncertainty. It refers to the voltage difference between the inverting and the non-inverting inputs, which ideally should be zero. For the SSIM the input offset voltage has

Table 5.3: The summary of the measurement uncertainty in the SSIM's electronics. The impact of some error sources, such as the digital potentiometer mismatch, is reduced through active correction with the SSIM's calibration stage.

Error source	**Uncertainty***	**Correction**
Bias current of O2A	0.0004%	No
Offset voltage of O2B	0.0085%	No
Johnson noise of R4	±0.0086%	No
ADC	±0.0012%	No
Shot noise of R4	±0.018%	No
Multiplexer leakage current	0.03%	No
ADC voltage reference	0.118%	Yes
Digital potentiometer mismatch	±1.35%	Yes
Total uncorrected uncertainty	1.53%	

*for 10 μA photodiode current, 85 °C temperature, and 1 MHz noise bandwidth

a maximum value of 23 μV. This parameter does not play a significant role for the amplifier stage 1 as it is a transimpedance amplifier. However, amplifier stage 2 has a maximum gain of 10, hence, the input offset voltage results in 230 μV or 0.0085% error at its output assuming a 10 μA photodiode current. Evidently, a sufficiently high-quality operational amplifier was selected for the SSIM application.

The digital potentiometer consists of two resistors, which allow one to programmatically adjust the gain of the amplifier stage 2 from 2 to 10 to boost the signal-to-noise ratio. The main error arising from this chip is the nominal resistance match. The maximum resistor mismatch is 1.5% over the entire temperature range of -40 to 85°C, which implies the gain uncertainty at the output of the amplifier stage 2 of ±1.35%. In the SSIM design this uncertainty is reduced by performing routine calibration of the digital potentiometer via the calibration stage.

The primary source of error in the multiplexer is a leakage current. The maximum value of this parameter in the SSIM is 3 nA, which translates to the uncertainty of ±81 μV or 0.03% at the output of the amplifier stage 1 for photodiode current of 10 μA. Finally, the ADC also causes the measurement uncertainty. The non-linearity, offset, full-scale, and the associated drift errors affect the accuracy of the ADC. The RMS error of the SSIM's ADC at 85 °C is 12 ppm or 0.0012%. The voltage reference of the ADC has an initial accuracy of ±0.1% plus the drift error of 180 ppm or 0.018% at 85 °C. Table 5.3 shows the summary

of the main causes of the measurement uncertainty in the SSIM. The digital potentiometer is by far the biggest contributor to the measurement error. However, this error can be significantly reduced through the active use of the calibration stage. Hence, even though the total measurement uncertainty is 1.53% for the -40 to 85 °C operating temperature range, the actual figure is much lower after the calibration.

5.6 SSIM's performance

The performance of the SSIM is evaluated against corresponding instruments in Table 5.1 from September, 2013 up to March, 2014. ASD spectroradiometer data are available up to November, 2013, while the pyrheliometer data is available for the entire period. Figure 5.13 shows comparison of the DNI as reported by the SSIM and the Eppley pyrheliometer for clear, cloudless periods over the past six months with DNI of at least 400 W/m^2. The SSIM's DNI is in excellent agreement with the pyrheliometer's DNI for October, 2013, where it is within ±1.5% limits for most data points. Furthermore, the SSIM's solar spectra match the ASD spectroradiometer's spectra very well, as indicated in Figure 5.14. In this figure the extracted aerosol optical depth at 500 nm, $\tau_{\mathrm{a}}(500)$, the ozone path-length, p_{o}, and the water vapour path-length, p_{w}, from the SSIM's measurements are given for two different timestamps on October 3$^{\mathrm{rd}}$, 2013. The difference in spectral resolution between the SSIM and the ASD spectroradiometer explains the variability in "smoothness" of the spectra between two instruments.

However, in mid November, 2013 a large difference in the DNI between the SSIM and the Eppley pyrheliometer was detected as shown by the time event ① in Figure 5.13. The hypothesis was made that the interference filters for some channels had suddenly degraded due to moisture ingress after a heavy storm. The responsivities of each photodiode-filter combination were remeasured and filter degradations of 15.5 and 40.2% on 420 and 500 nm channels, respectively, were observed, as demonstrated in Figure 5.15. The manufacturer of the photodiode-filter combinations reluctantly confirmed that these two channels are more susceptible to degradation than 610, 780, 940, and 1030 nm channels under high humidity conditions and rapid temperature fluctuations. The 420 and 500 nm channels were replaced in early December, 2013, as denoted by the time event ② in Figure 5.13, where on December 11$^{\mathrm{th}}$ a good agreement between the SSIM and the Eppley pyrheliometer is observed. Nevertheless, from the time event ③ the difference between two instruments has largely fluctuated from day to day. It is difficult to determine the exact date when the SSIM began deviating from the Eppley pyrheliometer after the 420 and 500 nm channels replacement, because of a limited number of sunshine hours at this time of year. Nevertheless, the SSIM's performance was

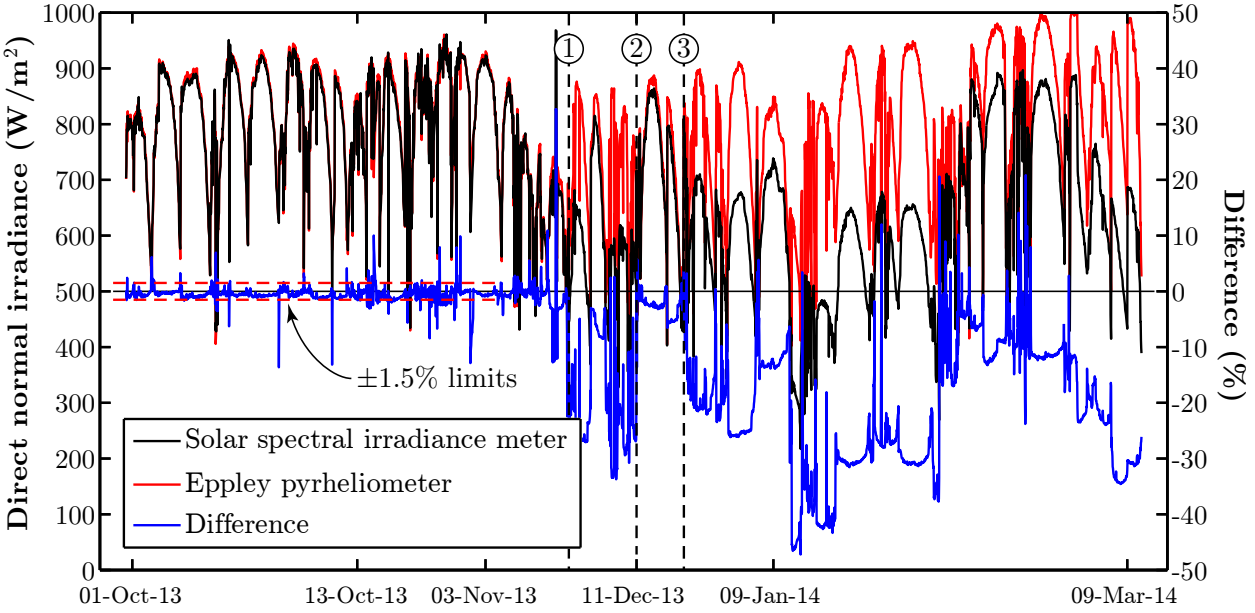

Figure 5.13: The comparison of the DNI as reported by the SSIM and the Eppley pyrheliometer for cloudless conditions at the University of Ottawa's CPV testing facility. The SSIM was in excellent agreement with the pyrheliometer for the month of October, 2013.

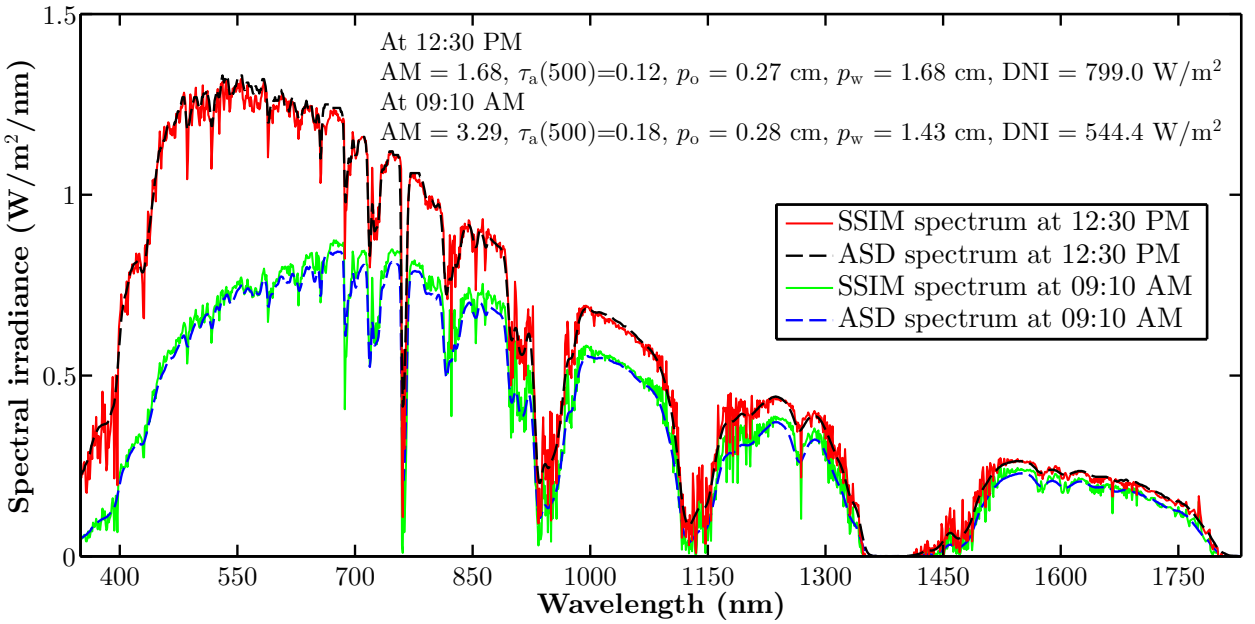

Figure 5.14: The comparison of the spectra as reported by the SSIM and the ASD spectroradiometer on October 3rd, 2013 at the University of Ottawa's CPV testing facility.

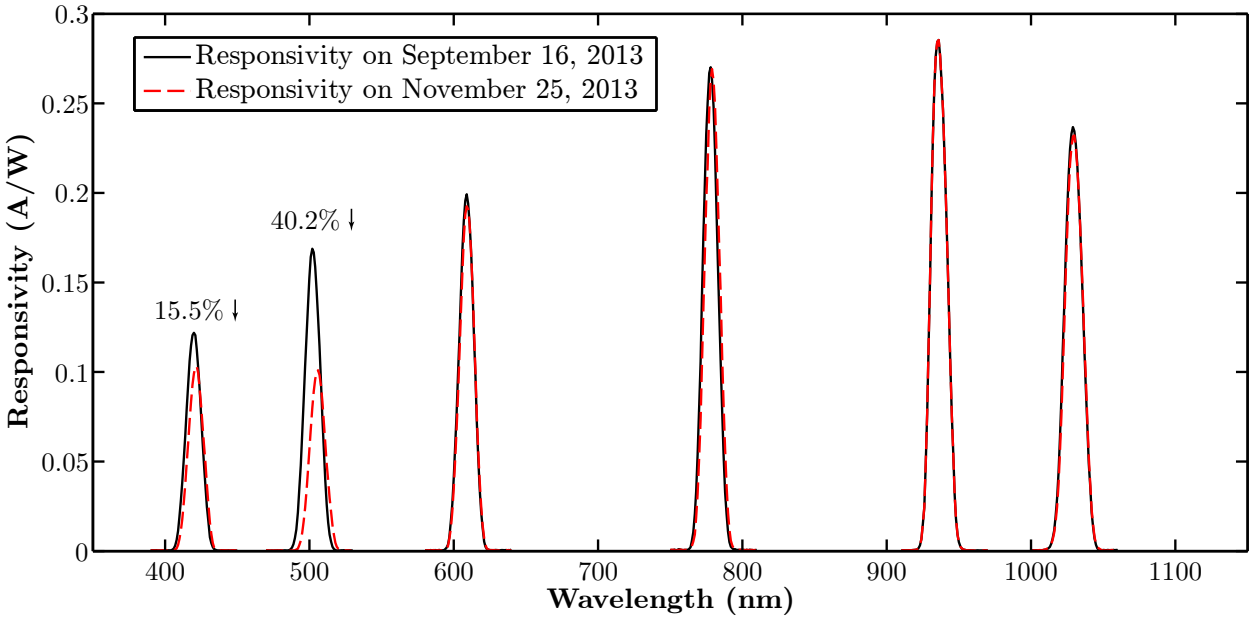

Figure 5.15: The filter degradation of the 420 and 500 nm channels after two month of operation. Evidently, the responsivity of other channels did not change.

limited by the interference filter degradation, and the condensation on the quartz window of the collimation tube, as demonstrated in Figure 5.16. The latter is primarily responsible for inconsistent day-to-day differences between the SSIM and the Eppley pyrheliometer. Several attempts were made to clear the condensation, but ultimately a vent allowing the pressure and temperature equalizations between the SSIM's enclosure and the ambient air is needed.

Even though the spectral DNI reproduction was limited by filter degradation and condensation, the SSIM's electronics functioned very well. Figure 5.17 shows the calibration current of the SSIM versus ambient and enclosure temperatures over a six month period starting in late September of 2013. The design value for the calibration current is 10 μA, but in practice due to resistor tolerances it is 9.96 μA at about 25 °C. Very subtle fluctuation of the calibration current with the enclosure temperature can be noticed from Figure 5.17. The maximum variation of 0.2% for the calibration current was observed for the enclosure temperature ranging from -15 to 30 °C. This result demonstrates the stability of the SSIM's electronics over a wide temperature range.

The SSIM measurements of the daytime ambient temperature and pressure were in good agreement with the corresponding values from the Lufft weather station. Figure 5.18 demonstrates the six month comparison for these parameters between the SSIM and the Lufft weather station. The ambient pressure profile was in excellent agreement between both

Figure 5.16: The condensation on the quartz window of the collimation tube as outlined by the dashed circle. It is one of the main factors limiting the SSIM's performance.

instruments. However, the SSIM's ambient temperature measurement was systematically higher than the value reported by the Lufft weather station, primarily due to the SSIM's temperature sensor placement. It is glued via a silicone paste to the back of the SSIM's alignment plate, which transfers the heat to the temperature sensor when exposed to the sun. This process biases the temperature sensor to overestimate ambient temperature, as indicated in Figure 5.18.

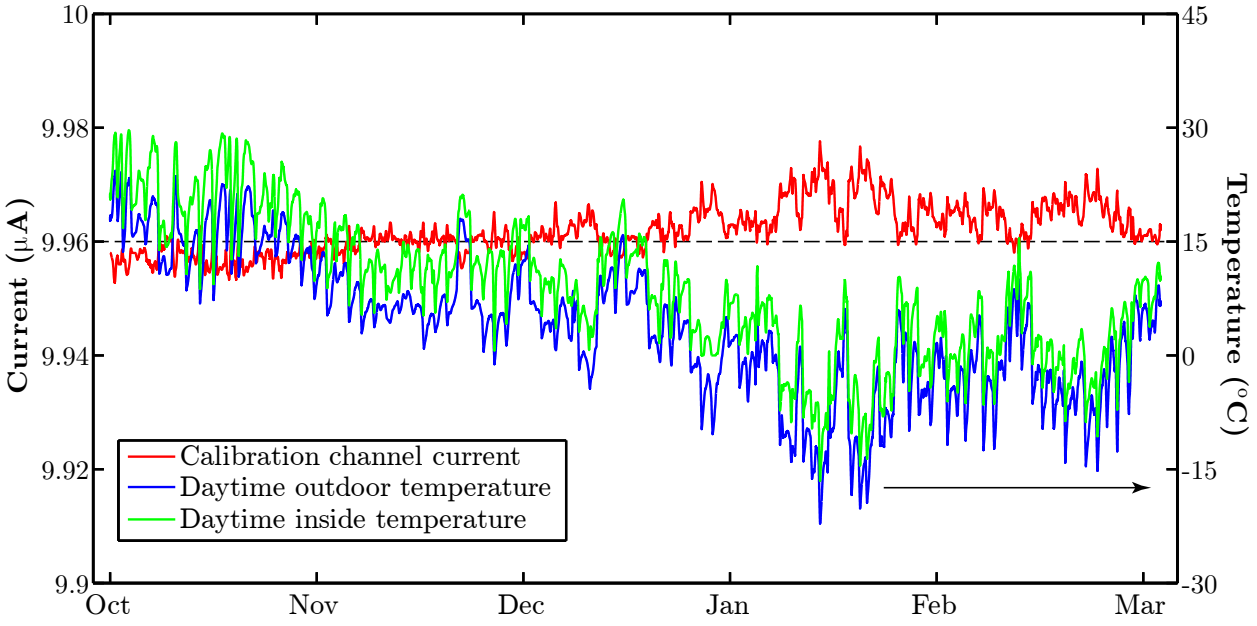

Figure 5.17: The calibration current of the SSIM versus the outdoor and the enclosure temperatures over time. There is a slight fluctuation of the calibration current with the temperature, but it remained within 0.2% over the six months. This result indicates temporal and thermal stability of the SSIM's electronics.

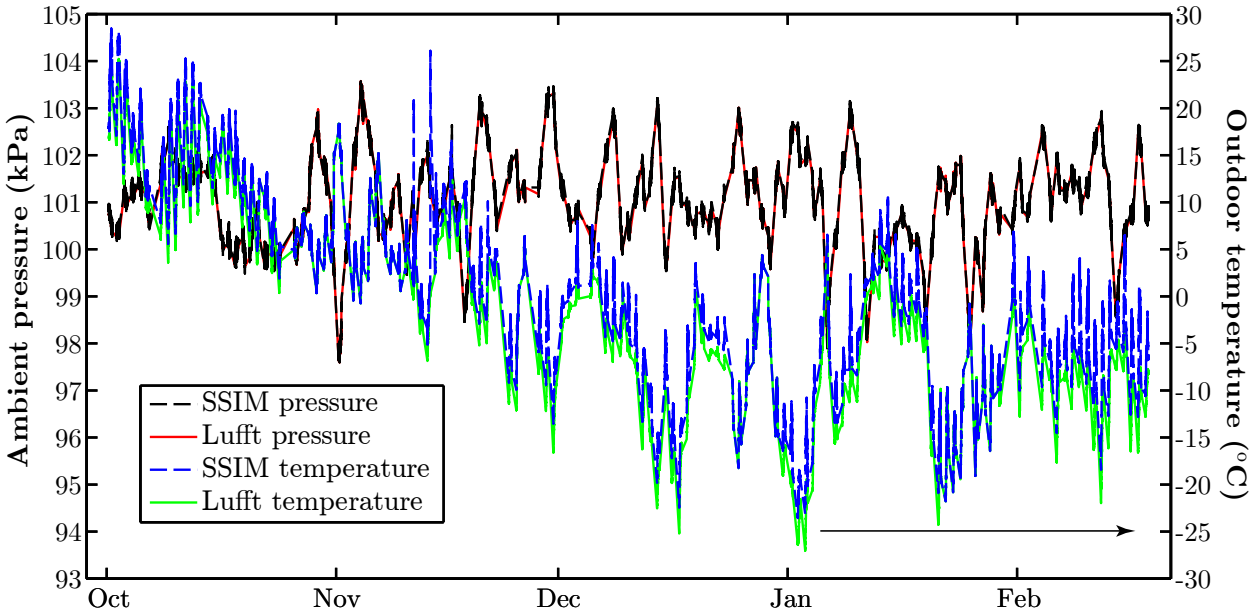

Figure 5.18: Comparison of the daytime ambient temperature and pressure profiles between the SSIM and the Lufft weather station. The SSIM's pressure profile is in excellent agreement with the Lufft weather station, while its temperature is slightly overestimated.

References

[1] W. McMathon, S. Kurtz, K. Emery, et al. *Criteria for the design of GalnP/GaAs/Ge triple junction cells to optimize their performance outdoors*. Tech. rep. National Renewable Energy Laboratory, 2002.

[2] O. Al Taher, R. Cravens, P. Pien, et al. "Qualification testing of 40% metamorphic CPV solar cells". In: *Photovoltaic Specialists Conference (PVSC), 2010 35th IEEE*. IEEE. 2010, pp. 1995–1998.

[3] N. Chan, H. Brindley, and N. Ekins-Daukes. "Impact of individual atmospheric parameters on CPV system power, energy yield and cost of energy". In: *Progress in Photovoltaics: Research and Applications* (2013).

[4] M. Muller, B. Marion, S. Kurtz, et al. "An investigation into spectral parameters as they impact CPV module performance". In: *AIP Conference Proceedings*. Vol. 1277. 2010, p. 307.

[5] *Guide to meterological instruments and methods of observation*. Tech. rep. Secretariat of the World Meteorological Organization, 2008.

[6] H. Winfield. *The art of electronics*. Cambridge University Press, 1995.

Chapter 6

Conclusion

CPV systems have the right features to be a significant source of energy generation in the near future. In order for this technology to become mainstream, more effort must be directed toward characterizing existing and developing new CPV technologies. This process requires affordable tools for the CPV community that enable solar spectral resource forecasting with great accuracy anywhere in the world. This thesis addressed this issue through the creation of the SSIM.

In chapter 2 the solar resource theory was described in detail as affected by astronomical, geographical, and atmospheric factors. In particular, the effects of the atmosphere on the solar spectrum were observed. It was established that highly variable atmospheric constituents, such as aerosols and water vapour, significantly affect the distribution of the solar spectral radiation at the earth's surface.

In chapter 3 a method of limited spectral sampling was presented by simulating the MCFR to reconstruct the solar spectrum. This model resolved major atmospheric processes, such as AM changes, Rayleigh scattering, aerosol extinction, ozone and water vapour absorptions. The verification of the model was accomplished by using FSR measurements at the University of Ottawa's CPV testing facility to mimic the outputs from the MCFR. This study was an essential step for determining the number and the type of channels required for the SSIM to adequately reproduce the solar spectrum.

Chapter 4 introduced a theory behind the operation of a single-junction solar cell, which was then extended to the model of the MJSC, consisting of InGaP, InGaAs, and Ge subcells. The model was used to quantify the effects of aerosols, ozone, and water vapour on the MJSC's performance throughout the day. The greatest spectral sensitivity was due to aerosol extinction and water vapour absorption variations. In summary, the knowledge of the solar spectrum is necessary for an accurate characterization of CPV systems.

In Chapter 5 the opto-mechanical and electrical designs of the SSIM were discussed. Furthermore, its performance was evaluated at the University of Ottawa's CPV testing facility over six months. Comparative analysis of the SSIM with the ASD spectroradiometer and the Eppley pyrheliometer was carried out between October, 2013 and March, 2014. The SSIM accurately reproduced the solar spectrum and consequently the DNI. The mean difference between the SSIM and the Eppley pyrheliometer was within $\pm 1.5\%$ for cloudless periods in October, 2013. However, the interference filter degradation for the 420 and 500 nm channels, and the condensation on the quartz window of the collimation tube negatively affected the performance of the SSIM. Outdoor-rated interference filters or equivalent are needed to ensure the device's long term reliability. Furthermore, a vent equalizing the pressure and the temperature between the SSIM's enclosure and the ambient air is required to avoid the condensation. Nonetheless, it was demonstrated that a cost-effective instrument can be built to replace an expensive spectroradiometer. The aforementioned design improvements will enhance the reliability of the next generation SSIMs.